

Graz University of Technology  
Faculty for Civil Engineering  
Institute of Applied Geosciences



Stefan Hausegger

# Deformation mechanisms and fluid-rock interactions in carbonate fault rocks

**DOCTORAL THESIS**

For obtaining the academic degree of

Doktor der Naturwissenschaften (Dr. rer. nat.)

Graz University of Technology  
Institute of Applied Geosciences

1<sup>st</sup> Assessor: Walter KURZ, Univ.-Prof. Mag. Dr.  
2<sup>nd</sup> Assessor: Scott KIEFFER, Univ.-Prof., Ph.D. P.E. C.E.G.  
Submitted by: Stefan HAUSEGGER, Mag.rer.nat.  
Submission: March 2013



## Acknowledgement

I would like to express my gratitude to my supervisor Univ.-Prof. Mag. Dr. Walter Kurz (Institute for Earth Sciences, University of Graz) for his support, patience and help during the work on this thesis and to Univ.-Prof. PhD Scott Kieffer (Institute of Applied Geosciences, Graz University of Technology).

Special thanks to Florian Mittermayr for his commitment and work on microprobe analysis at the University of Leoben, the memorable years at the Institute of Applied Geosciences (Graz University of Technology), all the helpful discussions and our great trips to China and St. Petersburg.

A sincere “thank you” to

- my colleagues at the Institute of Applied Geosciences (Graz University of Technology), especially to my former office roommates Robert Rabitsch, Thomas Rinder and Gerald Pischinger, Anna Pendl who had always an answer or a solution for any kind of (bureaucratic) question or problem and Daniel Höllen for his patient work on ICP-analysis.
- all supporters from the University of Graz (Institute for Earth Sciences), especially Franz Zmugg<sup>†</sup> for the perfect preparation of thin sections, Anton Pock for polishing them and Wolfgang Unzog for the rock saw (my favorite field tool!).
- Robert Scholger (Department for Applied Geosciences and Geophysics, University of Leoben) for providing the core drilling gear.
- Albrecht Leis (Joanneum Research, Graz) for providing stable isotope measurements and corresponding support.
- NAWI Graz – Doctorate Program “GASS - Graz Advanced School of Sciences” focusing on “Dynamics of Carbonate Systems” for the financial support.
- Dieter Mader (Department of Lithospheric Research, University of Vienna) for his support on the cathodoluminescence-microscope.
- Bundesamt für Eich- und Vermessungswesen (BEV) for providing digital elevation data of investigated sites.

Further thanks to my ice hockey team-mates for their contribution on keeping me strong, healthy and in shape. Special thanks to Hannes Stramitzer, Mathias Pflieger, Andreas Palan and Willi Hartstein for all the motivation, all non-scientific discussions and simply for

a great time. Also thanks to Markus Feldgrill for his help in the field and his great exertion when we collected samples and lug them down the steep slopes of site Brandwald.

Last but not least I want to express my deepest gratitude to my family and particularly to my parents. Thank you for your support, patience and understanding during all the years!

## Eidstattliche Erklärung

Ich erkläre an Eides statt, dass ich die vorliegende Arbeit selbstständig verfasst, andere als die angegebenen Quellen/Hilfsmittel nicht benutzt, und die den benutzten Quellen wörtlich und inhaltlich entnommenen Stellen als solche kenntlich gemacht habe. Diese Arbeit ist bislang keiner anderen Prüfungsbehörde vorgelegt worden.

---

Ort, Datum

---

Unterschrift

## Statutory declaration

I declare that I have authored this thesis independently, that I have not used other than the declared sources / resources, and that I have explicitly marked all material which has been quoted either literally or by content from the used sources.

---

place, date

---

signature

## Abstract

This thesis comprises investigations on the structural evolution of brittle fault zones in carbonate rocks with emphasis on fault zone structure, hydraulic properties, fluid flow and fluid chemistry along the Salzach-Ennstal-Mariazell-Puchberg (SEMP) fault system. The main results were published in three publications: Hausegger et al. (2010), Hausegger and Kurz (submitted to Tectonophysics) and Hausegger and Kurz (submitted to Journal of Structural Geology).

Chapter 1 (Hausegger et al., 2010) is mainly focused on fracture evolution, fault rock formation, grain size reduction and fluid flow in carbonate fault zones in locations along the Talhof fault segment (eastern part of the SEMP fault system). Analysis of samples from several structural domains (damage zone, transition zone and fault core) led to the reconstruction of a polyphase development. Layer-parallel shear caused the formation of joint-bounded slices oriented at high angles to the shear zone boundary (65 – 85°). Subsequent deformation and comminution processes marked the transition to cataclasite formation and fault core evolution. Continuous shear deformed cemented cataclasites by refracturing (“fault rock recycling”).

Stable isotope compositions ( $\delta^{13}\text{C}$ ,  $\delta^{18}\text{O}$ ) of fault rock cements indicate continuous equilibration between protolith-derived fragments and cements and point to limited fluid amounts, only temporally replenished by supposed meteoric water. A hydraulic gradient directed fluid flow from the damage zone towards the fault core in a cyclic change between an open and a closed system during fault evolution (Hausegger et al., 2010).

In chapter 2 (Hausegger and Kurz, submitted to Tectonophysics) three sites in Triassic carbonates (Ladinian Wetterstein limestone/ -dolomite) along the SEMP fault system were investigated with respect to brittle fault zone evolution and fault re-activation. Analysis of fault-slip data, structural inventory and particle size distribution app up to a classification of three different fault types (Fault type I, II and III). Progressive development from fault type III (thin solitary cataclasite layers) to fault type II (segmented cataclasite fault cores with thicknesses up to 1m) and fault type I (complex internal fault core structure and thicknesses up to several 10's of meters) is consistent with increasing displacement and increasing fault core width.

Type I faults are mainly parallel to the main fault direction in each site and exclusively evolve in a strike direction of maximum shear stress ( $\tau_{\text{max}}$ ). Type II and type III faults develop sub-parallel to the main fault direction and in orientations according to R, R' or X shear fractures with variable ( $\sigma_n / \tau$ ) ratio. Fault type classification and related paleostress analysis provides evidence from field observation compared to theoretical and analogue

models of Mohr-Coulomb fracture evolution (Hausegger and Kurz, submitted to Tectonophysics).

Chapter 3 (Hausegger and Kurz, submitted to Journal of Structural Geology) contributes to the understanding of comminution processes and changing fluid chemistry in cataclastic fault rocks. The analytical combination of cathodoluminescence microscopy (CL), microprobe analysis and stable isotope composition allowed the reconstruction of fluid chemistry evolution and led to a chronological classification of five fluid phases with respect to fluid chemistry, CL behavior and related structural processes. Dedolomitization processes along crystal borders and intragranular fractures during initial cataclasis are derived by Ca-rich fluids (Phase P1). Subsequent fluid phases (P2-P5) are characterized by variable Fe- (and Si-content) and therefore variable CL behavior.

Stable isotope signatures ( $^{13}\text{C}$ ,  $^{18}\text{O}$ ) indicate mainly meteoric origin of penetrating fluids and variable amounts of fluid, indicating a repeated change between an open and a closed system. Fe- and Si-enriched fluid phases (phase P2) are assumed to be derived from underlying clastic sequences of the Werfen Formation (Hausegger and Kurz, submitted to Journal of Structural Geology).

## References

Hausegger, S., Kurz, W., Rabitsch, R., Kiechl, E., Brosch, F.J., 2010. Analysis of the internal structure of a carbonate damage zone: Implications for the mechanisms of fault breccia formation and fluid flow. *Journal of Structural Geology* 32, Issue 9, 1349-1362.

Hausegger, S., Kurz, W., submitted. Cataclastic faults along the SEMP fault system (Eastern Alps, Austria) – a contribution to fault zone evolution, internal structure and palaeo-stresses. *Tectonophysics* (submitted to *Tectonophysics*, January 2013).

Hausegger, S., Kurz, W., submitted. Changing fluid chemistry during continuous shearing in cataclastic fault zones – a semiquantitative analysis based on cathodoluminescence, microprobe and stable isotope analysis. *Journal of Structural Geology* (submitted, March 2013).

## Zusammenfassung

Diese Arbeit behandelt die struktureologische Entwicklung von Störungszonen in Karbonaten unter spröder Deformation. Forschungsschwerpunkte wurden auf die strukturelle Entwicklung, die hydraulischen Eigenschaften, den Fluid-Durchfluss und die chemische Zusammensetzung der Fluide gelegt. Die Ergebnisse wurden / werden in drei Publikationen in internationalen Fachblättern veröffentlicht: Hausegger et al. (2010), Hausegger & Kurz (Tectonophysics, eingereicht) und Hausegger & Kurz (Journal of Structural Geology, eingereicht).

Kapitel 1 (Hausegger et al., 2010) legt Schwerpunkte auf die Genese von Störungsgesteinen unter Berücksichtigung der Entwicklung von Bruchstrukturen, Korngrößenzerkleinerung und dem Fluid-Durchfluss an ausgewählten Aufschlüssen entlang der Talhof Störung im östlichen Bereich des SEMP Störungssystems. Untersuchungen an Gesteinsproben eines Querprofils über die Störungszone deuten auf eine polyphase Entwicklung hin. Scherspannungen parallel zur Lagerung der Karbonate führen zu Bruchbildung in steilem Winkel und produzieren durch Bruchstrukturen begrenzte Bruchstücke. Weitergehende Deformation und Korngrößenzerkleinerung beschreibt den Übergang der Damage Zone zum kataklastischen Störungskern. Zementierte Kataklastite werden im Zuge anhaltender Scherspannung erneut deformiert. Dieser Zyklus wurde als „fault rock recycling“ bezeichnet.

Die Zusammensetzung von stabilen Isotopen der Zementproben deutet auf eine anhaltende Äquilibrierung zwischen protolithischen Fragmenten und ausgefallenen Zementen hin. Dies gibt Hinweise auf einen geringen Fluid-Durchfluss und nur temporärem Einfluss von meteorischen Wässern. In einem zyklischen Wechsel von einem offenen zu einem geschlossenen System leitet ein hydraulischer Gradient den Fluid-Fluss von der Damage Zone in den Störungskern.

Abschnitt 2 (Hausegger & Kurz, Tectonophysics, eingereicht) beleuchtet Aufschlussbereiche im Gesäuse und Hochschwabmassiv (Steiermark) entlang des SEMP Störungssystems unter besonderem Augenmerk auf sprödetektonische Entwicklung, Reaktivierung der Störungszonen und Paläostress-Analysen.

Die Auswertung der struktureologischen Daten, des strukturellen Aufbaus der Störungen und der Korngrößenverteilung der Störungskerne führte zu einer Klassifizierung von drei Störungstypen (Typ I, II und III). Zunehmender Versatz und die Aufweitung der Störungskerne bestätigt eine progressive Entwicklung von Typ III Störungen (einzelne, dünne Kataklastit-Bänder) über Typ II (Störungskerne bis zu 1m Mächtigkeit und interne



Segmentierung der Kataklastite) bis hin zu Störungstyp I mit Mächtigkeiten im Bereich mehrerer 10er Meter und komplexem Aufbau des Störungskerns.

Typ I Störungen entwickeln sich ausschließlich in Orientierungen mit maximaler Scherspannung ( $\tau_{\max}$ ) und stellen die Hauptstörungsrichtung der einzelnen Aufschlussbereiche dar. Typ II und III Störungen entwickeln sich sub-parallel zur Hauptstörungsrichtung und in Orientierungen von R, R' oder X Scherflächen mit variablem Verhältnis von Normal- und Scherspannung ( $\sigma_n / \tau$ ).

Das erarbeitete Klassifikationsschema und die Paläostress Analysen beschreiben theoretische und analoge Modelle des Mohr-Coulomb'schen Bruchkriteriums anhand der im Gelände gewonnenen Daten.

Untersuchungen chemischer Veränderungen von Fluiden und mikrostrukturellen Prozessen in den Aufschlüssen analog zu Kapitel 2 werden in einer weiteren Publikation veröffentlicht (Hausegger & Kurz, *Journal of Structural Geology*, eingereicht).

Die analytische Kombination von Kathodenlumineszenz (CL), Mikrosonde und stabilen Isotopen ermöglicht eine Rekonstruktion der Entwicklung des Fluid-Chemismus. In den betreffenden Arbeitsgebieten konnten fünf Phasen von Fluiddurchsatz nach ihrem Chemismus, dem Lumineszenzverhalten und zugehörigen strukturellen Prozessen unterschieden werden.

Dedolomitizierungsränder an Dolomit-Komponenten bzw. bereichsweise vollständige Dedolomitizierung während der initialen Kataklastose deutet auf Ca-reiche Fluide hin (Phase P1). Nachfolgende Phasen (P2-P5) zeigen charakteristische Änderungen in der chemischen Zusammensetzung (variabler Fe-Gehalt) und daher auch im Lumineszenzverhalten. Daten von stabilen Isotopen ( $^{13}\text{C}$  und  $^{18}\text{O}$ ) weisen auf grundsätzlich meteorischen Ursprung der Fluide hin. Zur Fe-Anreicherung wird eine temporäre Zirkulation durch tiefere, klastische Formationen (Werfener Formation) angenommen.

## References

Hausegger, S., Kurz, W., Rabitsch, R., Kiechl, E., Brosch, F.J., 2010. Analysis of the internal structure of a carbonate damage zone: Implications for the mechanisms of fault breccia formation and fluid flow. *Journal of Structural Geology* 32, Issue 9, 1349-1362.

Hausegger, S., Kurz, W., submitted. Cataclastic faults along the SEMP fault system (Eastern Alps, Austria) – a contribution to fault zone evolution, internal structure and palaeo-stresses. *Tectonophysics* (submitted to *Tectonophysics*, January 2013).

Hausegger, S., Kurz, W., submitted. Changing fluid chemistry during continuous shearing in cataclastic fault zones – a semiquantitative analysis based on cathodoluminescence, microprobe and stable isotope analysis. *Journal of Structural Geology* (submitted, March 2013).

# Table of Contents

Acknowledgement .....	III
Eidestättliche Erklärung .....	V
Statutory declaration.....	V
Abstract .....	VI
Zusammenfassung .....	VIII
Table of Contents .....	XI
Introduction.....	14
References .....	15
<b>1</b>	<b>Analysis of the internal structure of a carbonate damage zone: Implications for the mechanisms of fault breccia formation and fluid flow. .... 18</b>
1.1	Abstract .....
1.2	Introduction.....
1.3	Objectives.....
1.4	Methods of structural analysis.....
1.5	Geological and tectonic setting .....
1.6	Site description.....
1.7	Evolution of joints and shear fractures at the damage zone-fault core transition.....
1.8	Fault rocks along the damage zone–fault core boundary .....
1.9	Oxygen and carbon stable isotope compositions.....
1.10	Discussion of structural data .....
1.10.1	Implication for the formation of carbonate fault rocks.....
1.10.2	Mechanisms of deformation and grain size reduction .....
1.10.3	Implications for fluid - rock interaction and fluid flow .....
1.11	Conclusions.....
1.12	Acknowledgements .....
1.13	Appendix .....
	Analytical techniques.....
	Experimental conditions .....
	Coordinates of sites and sampling locations .....
1.14	References.....
<b>2</b>	<b>Cataclastic faults along the SEMP fault system (Eastern Alps, Austria) – a contribution to fault zone evolution, internal structure and palaeo-stresses. .... 52</b>
2.1	Abstract .....
2.2	Introduction.....

2.3	Methods.....	54
2.4	Geological and tectonic setting .....	55
2.5	Site description and structural inventory .....	58
2.5.1	Site Haindlkar .....	59
2.5.2	Site Brandwald .....	62
2.5.3	Site Fölz .....	64
2.6	Results .....	66
2.6.1	Fault type classification .....	66
2.6.2	Fabric and paleostress analysis .....	70
2.6.2.1	Site Haindlkar .....	71
2.6.2.2	Site Brandwald .....	72
2.6.2.3	Site Fölz .....	72
2.7	Discussion .....	73
2.8	Conclusions.....	76
2.9	Appendix .....	77
2.10	References.....	78
<b>3</b>	<b>Changing fluid chemistry during continuous shearing in cataclastic fault zones – a semiquantitative analysis based on cathodoluminescence, microprobe and stable isotope analysis. ....</b>	<b>87</b>
3.1	Abstract .....	87
3.2	Introduction.....	88
3.3	Site description.....	88
3.4	Methods.....	90
3.4.1	Sample preparation .....	91
3.4.2	Optical microscopy and cathodoluminescence .....	91
3.4.3	Microprobe analysis .....	92
3.4.4	Stable isotope composition .....	92
3.4.5	Inductively coupled plasma spectrometry (ICP).....	93
3.5	Results .....	93
3.5.1	Site Haindlkar .....	93
3.5.2	Site Brandwald .....	96
3.5.3	Site Fölz .....	99
3.6	Stable isotope analysis.....	102
3.7	Discussion .....	104
3.7.1	Fault development and comminution .....	104
3.7.2	Fluid phases and properties .....	108
3.7.3	Fluid source and fluid flow.....	110
3.8	Conclusions.....	111
3.9	References.....	112
<b>4</b>	<b>Applied Methodology .....</b>	<b>119</b>
4.1	Particle analysis .....	120
4.1.1	Particle detection.....	120

4.1.2	Measurements and data processing .....	121
4.2	References .....	124
<b>5</b>	<b>Conclusion .....</b>	<b>125</b>
Appendix	.....	127
A	Coordinates of sites and sampling locations .....	127
B	Analytical facilities .....	128
C	Data tables .....	131
	ICP-OES .....	131
	Particle analysis .....	133
D	Additional figures.....	134
Curriculum vitae	.....	137
Publications	.....	139

## Introduction

Investigations on the evolution of (internal) structures of and fluid penetration through brittle fault zones comprise multiple scientific approaches with emphasis on variable combinations of methods. Field studies (e.g., Anderson, 1951; Billi et al., 2003; Caine and Foster, 1999; Chester and Logan, 1986; Faulkner et al., 2003; Faulkner et al., 2008; Hancock, 1985; Mollema and Antonellini, 1999; Storti et al., 2001; Wibberley and Shimamoto, 2003), laboratory experiments and modeling (e.g., Caine and Foster, 1999; Coelho et al., 2006; Dooley and Schreurs, 2012; Gudmundsson, 2001; Konstantinovskaya et al., 2007; Shipton and Cowie, 2003; Wagreich and Decker, 2001) gave contributions to the understanding of the evolution of brittle fault zones in different environments.

This thesis is focused on the evolution of brittle fault zones, internal structural development, fluid flow and changes in fluid chemistry. Investigation areas are located along the central and eastern segment of the Salzach-Ennstal-Mariazell-Puchberg (SEMP) fault system. This sinistral Oligocene-Miocene fault system represents the most distinct structural feature in the Eastern Alps (e.g., Decker et al., 1993; Linzer et al., 1995; Ratschbacher et al., 1991; Ratschbacher et al., 1989; Schmid et al., 2004). Selected sites in the central part of the SEMP fault system are located in the Mürzalpen nappe of the Northern Calcareous Alps and crop out in Ladinian Wetterstein-limestone/ -dolomite units (site Haindlkar, Gesäuse Mountains; site Brandwald and Fölz on the south side of the Hochschwab massif). The Talhof fault (eastern segment of the SEMP fault) forms the boundary between the Lower Austroalpine Semmering-Wechsel nappe system, in the south, and the Upper Austroalpine nappe system, comprising the Greywacke zone and the Northern Calcareous Alps, in the north (Hausegger et al., 2010). Outcrops (site Stiegerinhütte) exhibit Lower Triassic (Anisian) marbles and Permian to Triassic quartzites.

The work proceeding comprises extended field studies (large and small scale mapping), sample collection from all structural domains of investigated fault zones (host rock, damage zone, transition zone, fault core), analysis of structural data (fabric and paleostress analysis), sample preparation (scans of specimen, thin sections, powder samples) and subsequent interpretation of analytical data. Executed analytical methods involve particle size analysis of cataclastic fault core rocks, petrographic microscopy, Cathodoluminescence microscopy, X-ray diffraction, ICP-OES, microprobe and stable isotope analysis ( $\delta^{13}\text{C}$ ,  $\delta^{18}\text{O}$ ).

Three publications constitute the main part of this thesis. Hausegger et al. (2010) is focused on the internal structure of carbonate damage zones, fault breccia formation and

fluid flow in the eastern part of the investigation area (Talhof fault). Chapter 2 (Hausegger and Kurz, submitted) gives contribution to fault zone evolution, internal structure and palaeo-stresses in the central part of the SEMP fault system (site Haindlkar, Brandwald and Fölz). Further investigations on changing fluid chemistry and fluid flow through different fault zone types classified in chapter 2 led to a manuscript (chapter 3), comprising cathodoluminescence microscopy, microprobe and stable isotope analysis. This combination of analytical methods provides to distinguish different phases of fluid flow in a chronological sequence and allows conclusions on the source and amount of circulating fluids.

## References

- Anderson, E.M., 1951. *The Dynamics of Faulting*. Oliver and Boyd, Edinburgh.
- Billi, A., Salvini, F., Storti, F., 2003. The damage zone-fault core transition in carbonate rocks: implications for fault growth, structure and permeability. *Journal of Structural Geology* 25, 1779–1794.
- Caine, J.S., Foster, C.B., 1999. Fault zone architecture and fluid flow: insights from field data and numerical modelling. in: Haneberg, W.C., Mozley, P.S., Moore, J.C., Goodwin, L.B. (Eds.) - *Faults and Subsurface Fluid Flow in the Shallow Crust*. Geophysical Monograph, Vol. 113. American Geophysical Union, 101–127.
- Chester, F.M., Logan, J.M., 1986. Implications for mechanical properties of brittle faults from observations of the Punchbowl Fault, California. *Pure and Applied Geophysics* 124, 79–106.
- Coelho, S., Passchier, C., Marques, F., 2006. Riedel-shear control on the development of pennant veins: Field example and analogue modelling. *Journal of Structural Geology* 28, Issue 9, 1658-1669.
- Decker, K., Mechede, M., Ring, U., 1993. Fault slip analysis along the northern margin of the Eastern Alps (Molasse, Helvetic nappes, North and South Penninic flysch, and the Northern Calcareous Alps). *Tectonophysics* 223, 291-312.
- Dooley, T.P., Schreurs, G., 2012. Analogue modelling of intraplate strike-slip tectonics: A review and new experimental results. *Tectonophysics* 574/575, 1–71.

- Faulkner, D.R., Lewis, A.C., Rutter, E.H., 2003. On the internal structure and mechanics of large strike-slip fault zones: field observations of the Carboneras fault in southeastern Spain. *Tectonophysics* 367, 235–251.
- Faulkner, D.R., Mitchell, T.M., Rutter, E.H., Cembrano, J., 2008. On the structure and mechanical properties of large strike-slip faults. in: Wibberley, C. A. J., Kurz, W., Imber, J., Holdsworth, R. E. & Collettini, C. (eds), *The Internal Structure of Fault Zones: Implications for Mechanical and Fluid-Flow Properties*, 139–150.
- Gudmundsson, A., 2001. Fluid overpressure and flow in fault zones: field measurements and model. *Tectonophysics* 336, 183–197.
- Hancock, P.L., 1985. Brittle microtectonics: principles and practice. *Journal of Structural Geology* 7, 447-457.
- Hausegger, S., Kurz, W., Rabitsch, R., Kiechl, E., Brosch, F.J., 2010. Analysis of the internal structure of a carbonate damage zone: Implications for the mechanisms of fault breccia formation and fluid flow. *Journal of Structural Geology* 32, Issue 9, 1349-1362.
- Hausegger, S., Kurz, W., submitted. Cataclastic faults along the SEMP fault system (Eastern Alps, Austria) – a contribution to fault zone evolution, internal structure and palaeo-stresses. *Tectonophysics* (submitted, January 2013).
- Konstantinovskaya, E.A., Harris, L.B., Poulin, J., Gennady, M.I., 2007. Transfer zones and fault reactivation in inverted rift basins: Insights from physical modelling. *Tectonophysics* 441, 1–26.
- Linzer, H.-G., Ratschbacher, L., Frisch, W., 1995. Transpressional collision structures in the upper crust: the fold-thrust belt of the Northern Calcareous Alps. *Tectonophysics* 242, 41-61.
- Mollema, P.N., Antonellini, M., 1999. Development of strike-slip faults in the dolomites of the Sella Group, Northern Italy. *Journal of Structural Geology* 21, 273–292.
- Ratschbacher, L., Frisch, W., Linzer, H.-G., Merle, O., 1991. Lateral extrusion in the Eastern Alps. Part 2: structural analyses. *Tectonics* 10, 257–271.
- Ratschbacher, L., Frisch, W., Neubauer, F., Schmid, S.M., Neugebauer, J., 1989. Extension in compressional orogenic belts: the eastern Alps. *Geology* 17, 404–407.
- Schmid, S.M., Fügenschuh, B., Kissling, E., Schuster, R., 2004. Tectonic map and overall architecture of the Alpine orogen. *Eclogae geol. Helv.* 97, 93-117.



- Shipton, Z.K., Cowie, P.A., 2003. A conceptual model for the origin of fault damage zone structures in high-porosity sandstone. *Journal of Structural Geology* 25, 333-344.
- Storti, F., Rossetti, F., Salvini, F., 2001. Structural architecture and displacement accommodation mechanisms at the termination of the Priestley Fault, northern Victoria Land, Antarctica. *Tectonophysics* 341, 141–161.
- Wagreich, M., Decker, K., 2001. Sedimentary tectonics and subsidence modelling of the type Upper Cretaceous Gosau basin (Northern Calcareous Alps, Austria). *International Journal for Earth Sciences* 90, 714-726.
- Wibberley, C.A.J., Shimamoto, T., 2003. Internal structure and permeability of major strike-slip fault zones: the Median Tectonic Line in Mie Prefecture, Southwest Japan. *Journal of Structural Geology* 25, 59–78.

# 1 Analysis of the internal structure of a carbonate damage zone: Implications for the mechanisms of fault breccia formation and fluid flow

Published in Journal of Structural Geology, Volume 32, Issue 9, September 2010, Pages 1349–1362

Stefan HAUSEGGER\*, Walter KURZ\*\*, Robert RABITSCH\*, Eva KIECHL\*, Franz-Josef BROSCH\*

\* Graz University of Technology, Institute of Applied Geosciences, Rechbauerstrasse 12, A-8010 GRAZ, Austria

\*\* University of Graz, Institute of Earth Sciences, Heinrichstrasse 26, A-8010 GRAZ, Austria

## 1.1 Abstract

This study reports the structural evolution along a segment of the Salzach- Ennstal fault zone (Talhof fault, Eastern Alps). The results are consistent with joint nucleation by layer-parallel shear, causing the formation of joint-bounded slices oriented at high angles (65 – 85°) with respect to the shear zone boundary (SZB). Subsequent slice rotation resulted in joint drag along the SZB, joint reactivation as antithetic shears, pervasive slice kinking, and breaking-up of the individual slices into smaller fragments. The latter process, due to the longitudinal constraint of slices with impeded shear zone widening, marked the transition to cataclasite formation and fault core evolution during shear localization. Cataclasites got cemented subsequently and underwent continuous shear deformation by re-fracturing. Pressure solution and cement precipitation from fluids therefore played a fundamental role in the evolution of the fault zone. Stable isotope compositions ( $\delta^{13}\text{C}$ ,  $\delta^{18}\text{O}$ ) of fault rock cements indicate a continuous equilibration between protolith-derived fragments and cements. This points to limited fluid amounts, only temporally replenished by supposed meteoric water, and a hydraulic gradient that directed fluid flow from the

damage zone towards the fault core. A cyclic change between an open and a closed system thus occurred during fault evolution.

**Keywords:** Fault zone, carbonates, high-angle fractures, joint- bounded slices, fault rocks, fluid – rock interaction

## 1.2 Introduction

Knowledge of the internal structure of brittle fault zones has been gathered from both field studies (e.g., Anderson, 1951; Tchalenko, 1970; Sibson, 1986; Chester & Logan, 1987; Chester et al., 1993; Caine et al., 1996; Billi et al., 2003; Faulkner et al., 2003; Wibberley & Shimamoto, 2003), and laboratory experiments (e.g., Riedel, 1929; Reches, 1978; 1983; Logan et al., 1979, 1992; Reches & Dietrich, 1983; Sagy, et al. 2001; Katz et al., 2003). Fluid infiltration into faults, and the subsequent fluid-rock interaction, influence the fault mechanical behavior (Hubbert and Rubey, 1959; Janssen et al., 1998; Kurz et al., in press). Characterization of the internal structure of fault zones is an essential pre-requisite to understanding and predicting their mechanical, hydraulic and seismic properties (e.g., Faulkner et al., 2003). Generally, the following structural elements may be discriminated across brittle fault zones (following Chester and Logan, 1986; Caine et al., 1996; Caine and Foster, 1999; Billi et al. 2003; Faulkner et al., 2003):

- (1) The host rock, or protolith, consisting of the rock mass bounding the fault-related structures. The host rock is characterized by a lower amount of finite deformation with respect to the main fault zone.
- (2) The damage zone, characterized by subordinate faults, veins, and networks of shear and extensional fractures generally related to the processes of fault growth. Generally, the transition from the host rock to the damage zone is quite gradual. The damage zone is defined as the domain that bounds the fault core.
- (3) The fault core, where shear displacement is localized, is associated with the development of fault rocks by bulk crushing, particle rotation, abrasion and grain size diminution that obliterate the original rock fabric (e.g., Billi et al., 2003; Storti et al., 2003; Billi and Storti, 2004; Billi, 2005, 2007). The evolution of fault rocks within the fault core particularly depends on normal and shear stresses, displacement and strain rate.
- (4) Another structural element playing a significant role in describing the growth processes of a single discrete fault zone is the 'process zone'. Following the definition of Vermilye and Scholz (1998), the process zone comprises those features that result directly from

propagation of the fault tip. It may overlap with the damage zone as well as with parts of the fault core.

These structural elements may also be seen as representing the evolutionary steps of fault development. As the fault core evolves continuously within the damage zone (e.g., Billi et al., 2003; Faulkner et al., 2003), the spatial zoning from the protolith to the core, including the development of fault rocks, corresponds to these evolutionary steps (e.g., Micarelli et al., 2006).

### **1.3 Objectives**

In this study we discuss the structural evolution of carbonate fault rocks along a large fault zone in the Eastern Alps. We focus on the structures that formed during the initial phases of fracturing and on these related to subsequent fault zone evolution. In other words, we study fractures that formed prior to the full development of fault rocks, and those in the transition from the fault damage zone to the fault core. The aim is to provide new insights on the structural evolution of fault zones and on the mechanisms of fault rock formation.

In particular we present new observations on the internal structure of a large strike-slip fault within the Eastern Alps (Fig. 1-1). This structure is controlled by an anisotropic host rock fabric. This fabric, together with the repeated activation of discontinuities, may have obliterated the original fracture-mechanical rock properties, and modified the angular relationships of fractures generated during faulting (e.g., Paterson, 1978; Jaeger and Cook, 1979; Rispoli, 1981; Peacock and Sanderson, 1992; Willemse et al., 1997; Mollema & Antonelli, 1999). For this reason the importance of fractures at high-angles to any pre-existing deformation-related anisotropy, being re-activated by layer-parallel shear, will be discussed in detail. Moreover, we focus on the role of these structures in the development of brittle shear zones and brecciation. Finally we investigate the fluid-rock interaction with emphasis on dissolution and precipitation mechanisms. Stable isotope analysis of selected samples provides information on the interaction of fractured domains and fault rocks with fluid phases and on the origin of fluids entrapped within the fault zone.

## 1.4 Methods of structural analysis

In the field, samples were taken from the damage zone towards the fault core in order to infer the evolution of structures towards increasing displacement. Samples were saw-cut into serial sections parallel to the local direction of shear, and perpendicular to the shear zone boundary (SZB). The traces of the fracture network, voids and pores were highlighted by staining with a permanent black marker pen, and subsequent polishing along the cut sample surfaces.

We described the fractures by considering their orientation with respect to the overall shear direction. Orientation distributions of distinct fracture sets were analyzed by using the program package Tectonics FP 1.6.2, a 32-bit Windows™-Software for Structural Geology (Reiter and Acs, 2002). The sizes of fragments and grains (maximum and minimum diameter,  $F_{max}$  and  $F_{min}$ ) were determined by measuring the normal distances between two parallel tangents to the fragment margins at opposite points along the fragment boundaries. This was done by the application of an automated image analysis package (analysis auto 5.0, © 1986-2006, Olympus Soft Imaging Solution GmbH).

## 1.5 Geological and tectonic setting

We selected several sites along the Talhof fault (Gmeindl, 1999), which is a 15 km long segment of the Salzach – Ennstal - Mariazell - Puchberg (SEMP) fault system in the Eastern Alps (Fig. 1-1) (Ratschbacher et al., 1989, 1991; Decker et al., 1993; Decker and Peresson, 1996; Wang and Neubauer, 1998; Frisch et al., 2000). The WSW–ENE oriented SEMP fault extends for 400 km along the Eastern Alps. The maximum left lateral displacement along the central segments of the SEMP approximates 70 km (Linzer et al., 2002). The fault trends sub- parallel to the regional orogenic strike from the western part of the Tauern Window to the Vienna Basin (Fig. 1-1), and crosses all Austroalpine tectono-stratigraphic units. The fault zone separates the Austroalpine and Penninic units of the central Eastern Alps, which experienced substantial orogen- parallel extension during the Oligocene and Miocene. The SEMP forms the lateral ramp of west- and east-directed detachment faults that accounted for the tectonic exhumation of the Tauern metamorphic dome. Deeper structures of the western fault segment were exhumed by the late Neogene uplift of the Tauern Window. Ductile deformation structures adjacent to the Tauern Window change eastward into a narrow zone deformed under ductile–brittle transitional conditions. On the contrary the central and eastern segments show brittle deformation distributed over a broad shear zone.

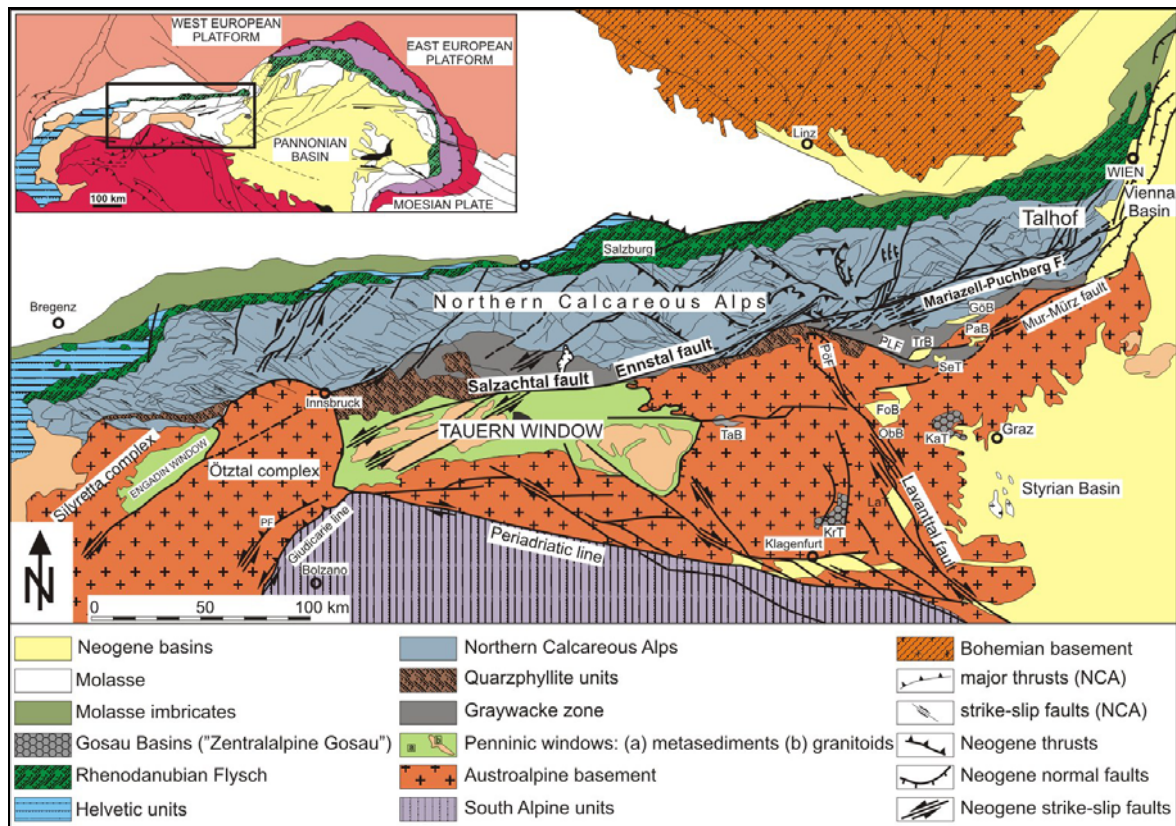


Figure 1-1: Tectonic map of the Eastern Alps displaying the Paleogene to Neogene fault system (after Linzer et al., 2002). The sites discussed in this contribution are located along the Talhof segment of the Salzach-Ennstal-Mariazell-Puchberg fault (SEMP) (see Fig. 1-2).

TH=Talhof fault segment of the Salzach-Ennstal-Mariazell-Puchberg fault system; AF=Ahrtal fault; AnF=Annaberg fault; BL=Brenner line; DHL: Döllach-Heiligenblut line; EL=Engadine line; GöF=Göstling fault; HoF=Hochstuhl fault; InF=Inntal fault; IsF=Iseltal fault; KL=Katschberg line; KLT=Königssee –Lammertal –Traunsee fault; LoF=Loisach fault; LS=Lower Schieferhülle; MöF=Mölltal fault; ÖT: Ötztal thrust; PF=Peijo fault; PeF=Pernitz fault; PLF =Palten – Liesing fault; PöF=Pöls fault; PyF=Pyhrn fault; RTS=Radstadt thrust system; RW=Rechnitz window; SaF=Salzsteig fault; TF=Telfs fault; WeF=Weyer fault; WGF=Windischgarsten fault; Z=Zell pull-apart structure; ZC=Zentralgneiss core. GöT=Göriach basin; PaT=Parschlug basin; SeT=Seegraben basin; FoT=Fohnsdorf basin; ObT=Obdach basin; WiT Wiesenau basin; StT=St. Stefan basin.

In the area described in this study, the SEMP forms the boundary between the Lower Austroalpine Semmering-Wechsel nappe system, in the south, and the Upper Austroalpine nappe system, comprising the Greywacke zone and the Northern Calcareous Alps, in the north. Nappe assembly of Austroalpine nappes took place during the Early Cretaceous. The main thrusts, however, were re-activated and overprinted during Oligocene to Miocene faulting.

The subvertical, approximately E-W striking Talhof fault segment (Fig. 1-2) shows left-lateral displacement. It is cut by the NE- trending left-lateral Altenberg and Mur-Mürz faults

in the west and in the east, respectively. The Talhof fault zone is marked by trenches and ridges formed by subvertical to steeply dipping carbonate beds.

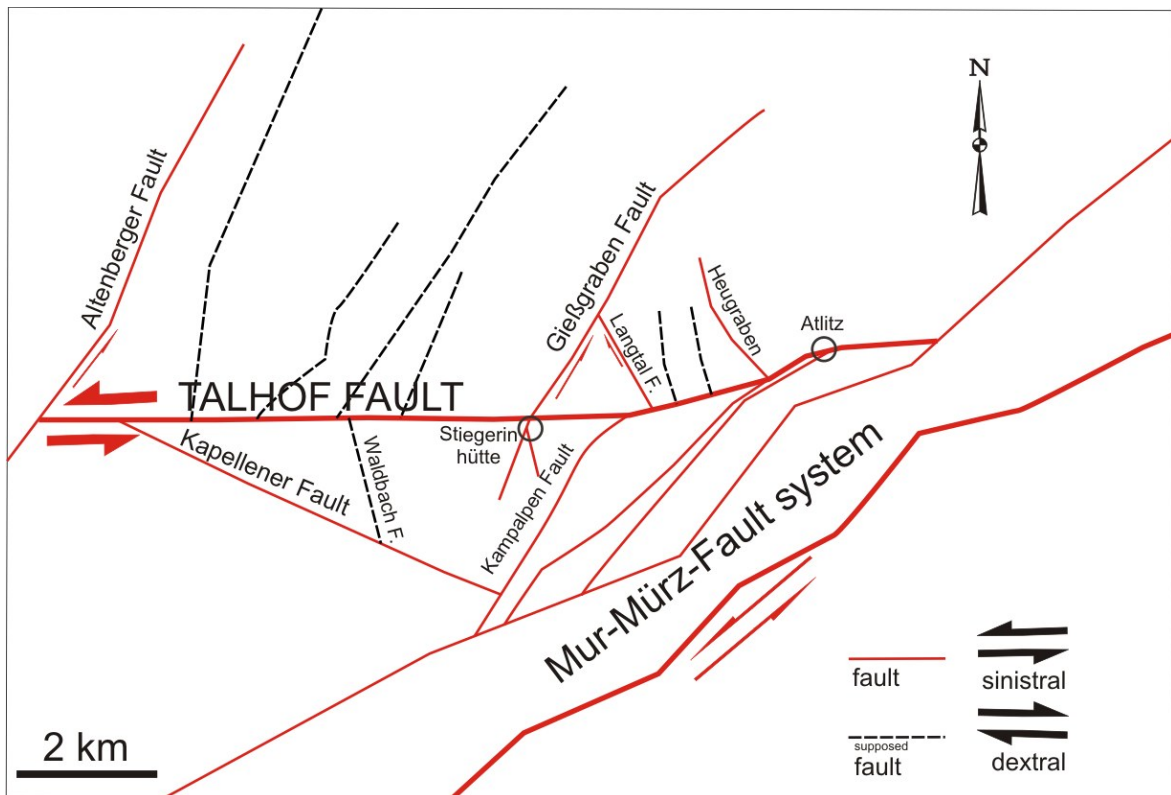


Figure 1-2: Fault map showing the surface intersections and strike directions of the Talhof fault and associated conjugate faults (after Kiechl 2007).

## 1.6 Site description

The site described in this study provides a nearly complete exposure of a section across the Talhof and Giessgraben fault zones, i.e. from the protolith to the fault core (Fig. 1-3). At the Talhof - Giessgraben fault intersection (Fig. 1-2), Lower Triassic (Anisian) fine grained layered marbles are separated from quartzites of Permian to Triassic protolith age, both belonging to the Lower Austro-Alpine unit (Fig. 1-1). Within the quartzites, the protolith is almost totally disintegrated up to the formation of incoherent, impermeable fault gouges (the fault core). Within the marbles, the fault-related deformation is concentrated along the nearly vertical discontinuities defined by a composite metamorphic foliation and sedimentary bedding that acted as slip planes. For this reason, the latter are considered as the shear zone boundaries (SZB) (Brosch & Kurz, in press). The general width of the

fault zone is difficult to estimate due to the susceptibility of highly disintegrated parts to weathering and erosion. We measured a width ranging from a few to approximately 25 m. The section exposed at the site “Stiegerinhütte” can be subdivided into several structural domains (Fig. 1-3). The damage zone adjacent to the core is made up of SW-NE striking layered carbonates showing a sharp, subvertical slickensides contact to the fault core. Domain 1 is characterized by cemented carbonate fault breccias and cataclasites with a thickness up to 0.5 m. Domains 2-4 include fault rocks derived from a quartzitic protolith. Domain 2 has a thickness of approximately 1.5 m, and consists of fine-grained quartz-rich gouges (up to 90% quartz) with minor contents of carbonates. The grain size is usually less than 0.5 mm. Lenses of highly disintegrated basement gneisses, mainly transformed into fault gouges, are exposed in domains 2a and 2b. Domain 3 is similar to domain 2 but conversely is characterized by a larger grain size (0.7 to 2 mm) and by the lack of carbonates. Domain 4 consists of irregularly fragmented and un-cemented quartzite. Fragment sizes vary between 1 and 5 cm.



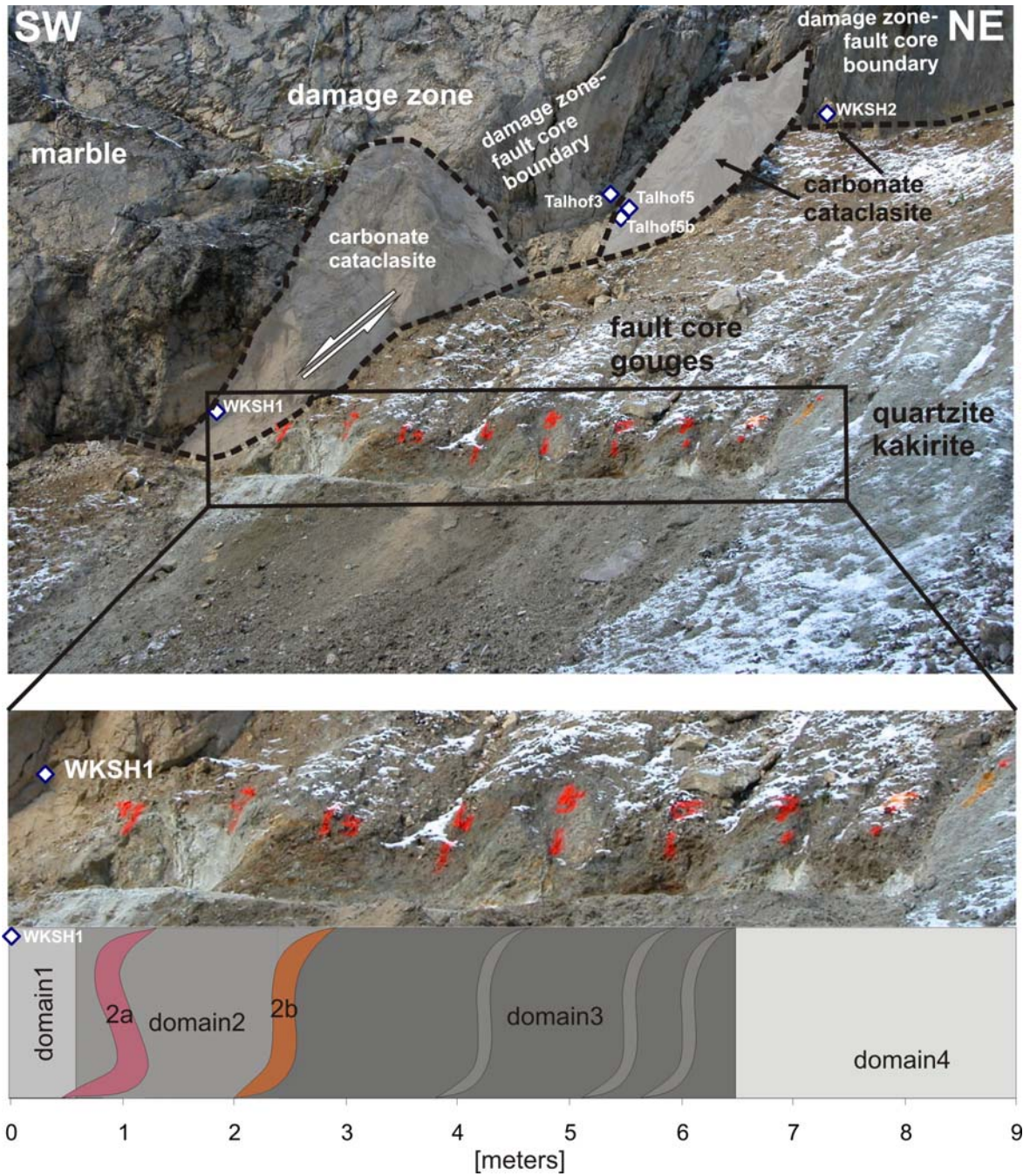


Figure 1-3: Field view and section across the Talhof fault – Giessgraben fault - intersection at site “Stiegerinhütte”, including the subdivision of fault core domains (see text), and locations of sampling. For site coordinates see Appendix.

## 1.7 Evolution of joints and shear fractures at the damage zone-fault core transition

Rocks of the damage zone adjacent to domain 1 are characterized fractures at high (50 - 120°) and low (10 - 30°) angles to the shear zone boundary. In this study, these fractures are named as high- and low- angle fractures, respectively. The relative timing of fracture formation can be determined by abutting and crosscutting relationships. The high-angle fractures generally form as cross joints (Mollema and Antonelli, 1999) within the moderately wide spaced layers, and show subsequent reactivation as sheared fractures. This reactivation is indicated by the offset of the bedding and pre-existing foliation. Low-angle fractures at angles between 20 and 30°, measured in an anticlockwise sense to the SZB, are sheared fractures. Structures at angles between 0 and 20°, clockwise to the SZB, are pressure solution seams (stylolites) (Figs. 1-4 to 1-9).

The original primary fracture fabric is dominated by a set of sub-parallel joints at high angles (50-85°) to the SZB (Figs. 1-4 to 1-6), with a spacing of 0.5 to 2 cm. A frequency maximum is developed at 75° (Fig. 1-4c). Consequently, the general structure is characterized as an array of roughly prismatic rock slices (Figs. 1-4a, b, 1-5a, b, 1-6a). These slices were termed “lamellae” by Brosch and Kurz (in press). The mean thickness of the slices in population varies between 2 and 25 mm, with mean values between 7.5 and 20 mm (Tab. 1-1), the length between approximately 20 and 160 mm (mean between 13.6 and approx. 37 mm) (Tab. 1-1). The ratio of the maximum to minimum diameter of the slices,  $F_{\max}$  and  $F_{\min}$  respectively, varies from 1.6 to 3.3, with mean values between 2.08 and 2.84 (Tab. 1-1). In general the slices tend to decrease in length and thickness towards the fault core (particularly mean  $F_{\max}$  decreases from approximately 37 to 18 mm) (Tab. 1-1). The  $F_{\max}/F_{\min}$  ratio, however, seems to attain constant values (within a  $1\sigma$  standard deviation) between 2.8 and 2.3 (Tab. 1-1). Concerning the general shear direction along the SZB, most slices exhibit antithetic displacements due to the shearing of joints. Voids and pull-aparts along the sheared joints are partly healed with sparitic calcite cement.

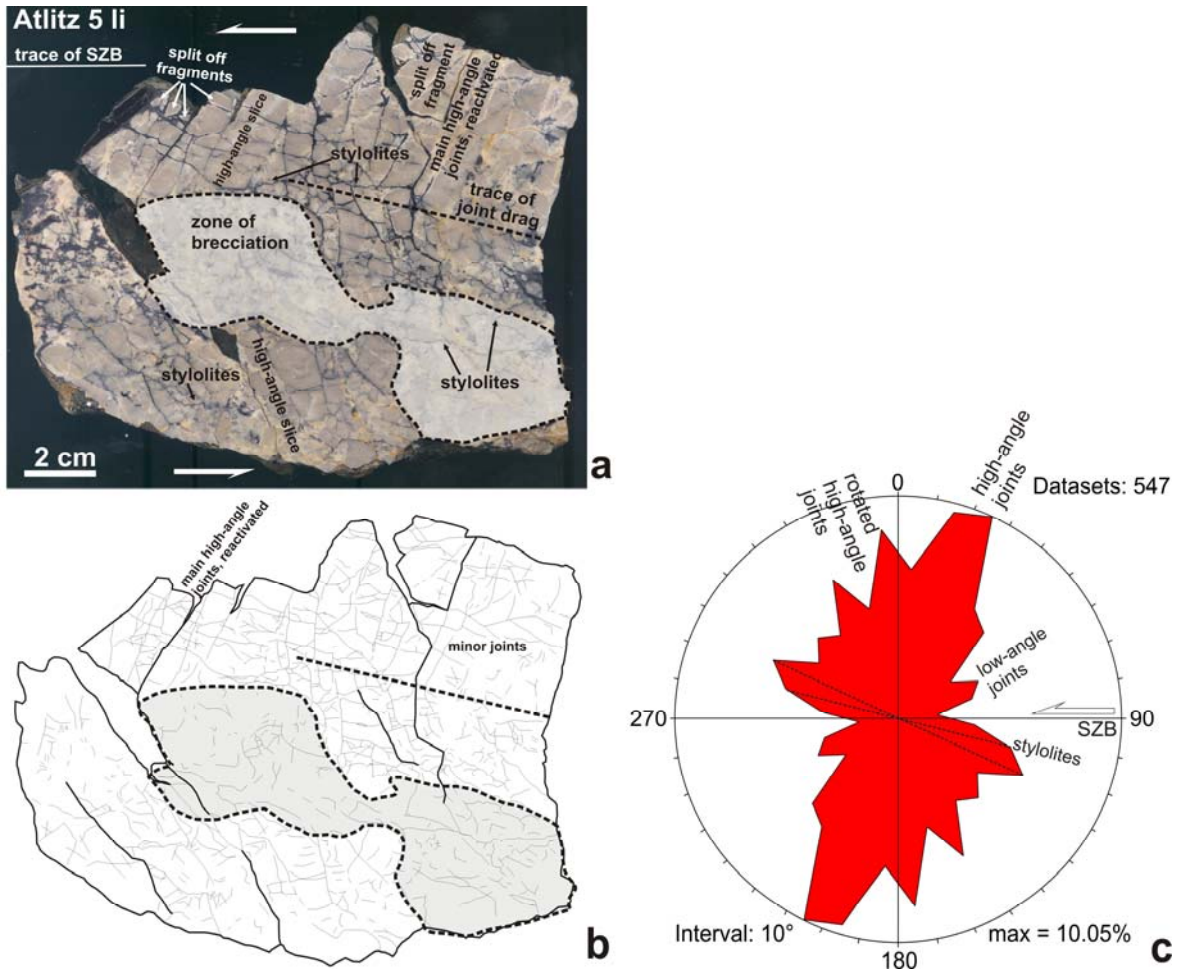


Figure 1-4: (a), (b) Fracture pattern of carbonate rocks located within the Talhof fault damage zone, at a distance of approximately 60 cm to the damage zone – fault core contact. The shear zone boundary (SZB) runs parallel to the bedding/foliation. Slices with a thickness of approximately 1 cm are bordered by sub-vertical major fractures (thick lines) formed at high angles to the SZB. Minor joints (thin lines) in the internal parts of the slices either run sub-parallel to the SZB or occur as probably conjugate sets. Pressure solution seams (stylolites) form pre-dominantly at low angles, 10-15° clockwise to the SZB. Slice-bounding fractures are partly dragged, the slices in the upper part of the samples are partly kinked, the trace of the kink band is marked by a stippled line. Slices in the lower part of the sample are rotated anticlockwise related to a sinistral sense of shear along the SZB. The kink zone in the central part is characterized by the formation of slice-derived fragments embedded within a finer-grained carbonate matrix. The shear sense within the kink zone coincides with the general sense of shear along the SZB. Sample from site “Atlitz” (see Appendix). (c) The Rose diagram displays the orientation of the distribution of minor joints relative to the SZB, with a maximum frequency at 75-85° anticlockwise from the SZB, and additional maxima within the NW sector of the diagram, interpreted as rotated high-angle joints. Sub-maxima at low angles to the SZB are interpreted to represent conjugate minor shears to the SZB. Arrows indicate the displacement along reactivated structural elements.

Most slices show an internal fabric formed by low- and high- angle joints, too (Figs. 1-4 to 1-7). Since these joints are only present within individual slices, they are considerably shorter (average length of 1-2cm) than the slice- bounding ones. These internal fractures



do not show any considerable displacement and usually terminate against slice- bounding ones. In this study these fracture sets are described as minor joints. The maximum and minimum diameters ( $F_{max}$ ,  $F_{min}$ ) of fragments surrounded by these range from 2 to 10 and 1 to 6 mm, respectively, with a mean between 3.6 and 9.6 mm for the maximum ( $F_{max}$ ) and 2 and 4.8 mm for the minimum diameter ( $F_{min}$ ). The  $F_{max}/F_{min}$  ratios show mean values between 1.60 and 2.40, and a bulk mean value of  $1.94 \pm 0.69$  (Tab. 1-1). With decreasing distances to the fault core, the slice-internal structure is dominated by low-angle joints, with a maximum frequency oriented at angles between 5 and 30° (Figs. 1-6b, c). Structures oriented sub- parallel to the SZB are mainly characterized by pressure solution seams (Figs. 1-4 to 1-8). (Sub-) maxima at quite high angles turn up at 75°, 100°, and 120° anticlockwise to the SZB (see rose diagrams in Figs. 1-4 to 1-7).

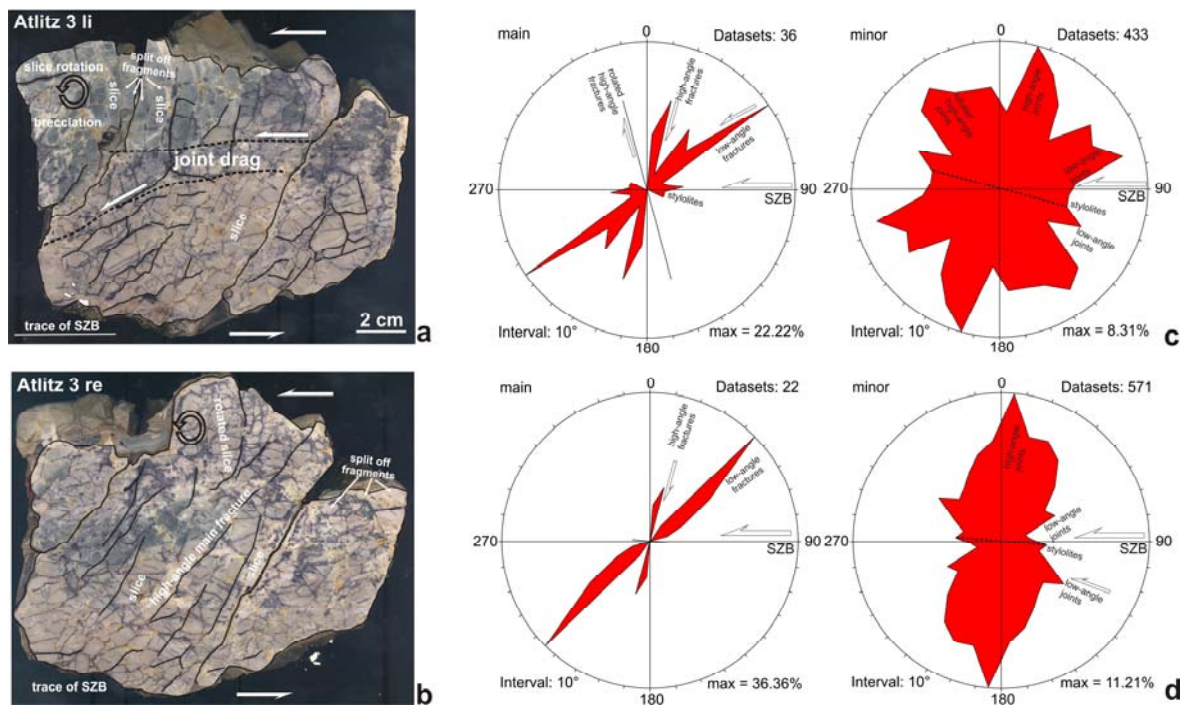


Figure 1-5: (a), (b) Fracture pattern of carbonate rocks located within the Talhof fault damage zone at a distance of approximately 45 cm and 40 cm to the damage zone – fault core contact, respectively. Thick lines: major fractures, thin lines: minor joints. (c), (d) The Rose diagrams display the orientation of the distribution of major and minor fractures relative to the shear zone boundary (SZB). Maximum frequencies of slice- bounding joints are located between 65° and 85° anti-clockwise from the SZB, with additional maxima between 100° and 130° anti-clockwise from the SZB. These are interpreted to represent rotated high-angle joints. Stylolites predominantly form at low angles, 10-15° clockwise to the SZB. Arrows indicate the displacement along reactivated structural elements. Sample from site “Atlitz” (see Appendix).

Along distinct, 0.5 to 2 cm thick zones oriented sub-parallel to the SZB, the slices are fractured perpendicular to their long axes. This results in the development of kinked slices

(Figs. 1-4 to 1-7). Prior the kinking, both joints and slices were rotated in an anti-clockwise sense (i.e. synthetically to the general shear direction). This resulted in the dragging of the slice- bounding joints along the SZB and shearing (Figs. 1-5a, b). Within the kink zones, slices are irregularly fractured and broken up to fragments, which are embedded within a fine-grained matrix of crushed host rock material or within sparitic carbonate cement (Figs. 1-4a, 1-6a). The fragments show an isometric shape with angular to sub-rounded boundaries. Fragment interfaces may show distinct displacements at the scale of millimeters. Pressure solution seams (stylolites) are formed along fragment contacts aligned sub-parallel, or at low angles, to the confining kink zone boundary or SZB (Figs. 1-4a, 1-6a). Locally, a completely developed matrix-supported fault breccia characterized by structural features indicating fragment wear, attrition, and fragment rotation developed within and between the slice domains. The matrix consists of fine-grained carbonate and residual clay minerals in the clay/silt grain size fractions.

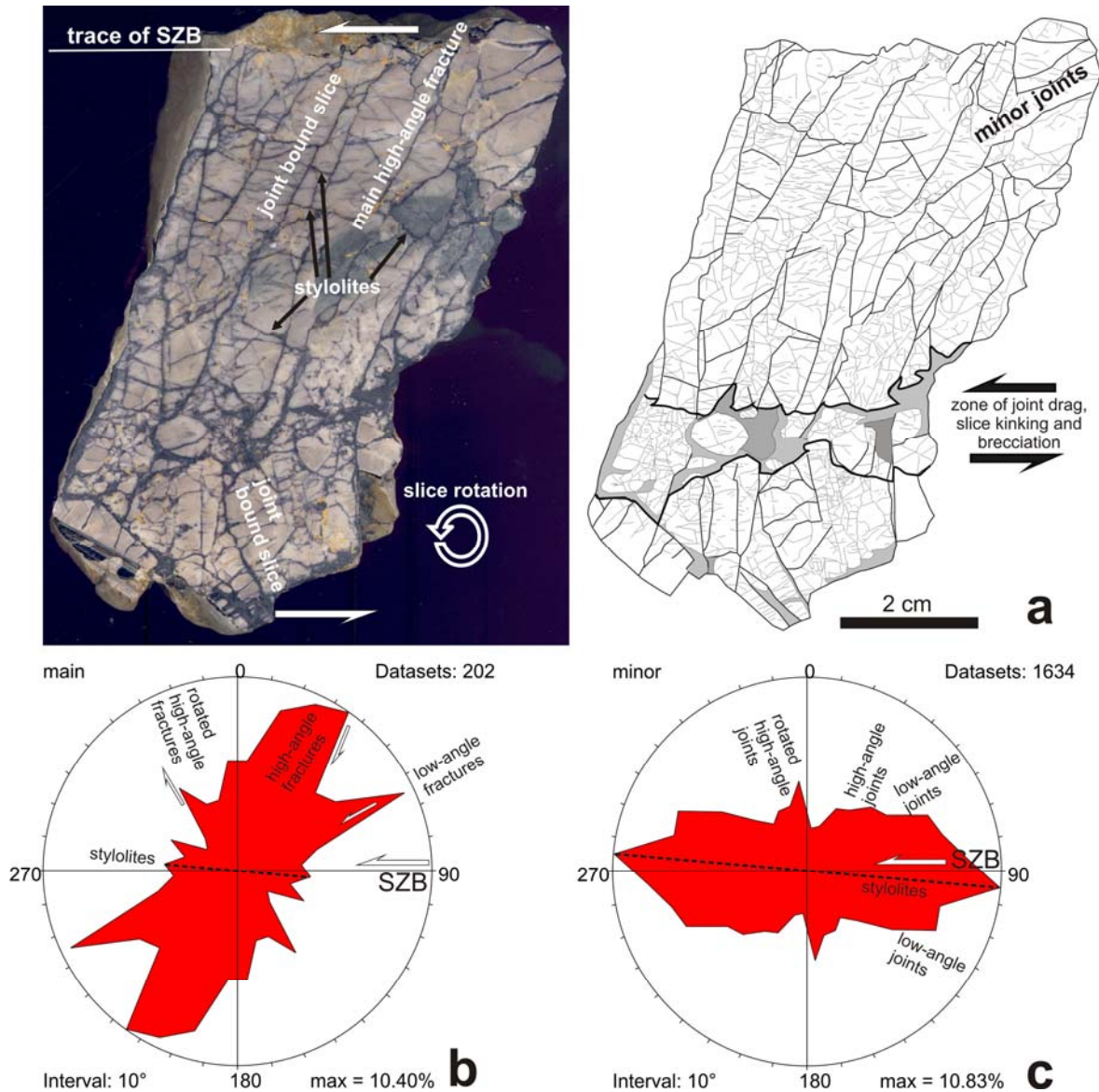


Figure 1-6: (a) Fracture pattern of carbonate rocks along the Talhof fault damage zone – fault core transition. The distance to the damage zone – fault core boundary is approximately 30 cm. The shear zone boundary (SZB) runs parallel to the bedding/foliation. Thick lines: major fractures, thin lines: minor joints. The Rose diagrams display the orientation of the distribution of major (b) and minor (c) fractures relative to the SZB. Note the predominance of low-angle and SZB- parallel minor shears. The slices are kinked related to a sinistral sense of shear along the SZB. The kink zone is characterized by the formation of slice-derived fragments embedded within a finer-grained carbonate matrix. The shear sense within the kink zone coincides with the general sense of shear along the SZB. Arrows indicate the displacement along reactivated structural elements. Sample from site “Stiegerinhütte” (see Appendix). See Fig. 1-3 for sampling site.

Close to the fault core, the slice- dominated fabrics described above are obliterated by increasing fragmentation due to development of fractures at low angles to the SZB (samples Atlitz2 and Atlitz1) (Figs. 1-7, 1-8). The partly dismembered survivor slices show an antithetic rotation of more than 30° related to the initial slice orientation. Beside

rotation, the slices were affected by fragmentation and fragment rotation, which resulted in the development of voids and extension fractures (Figs. 1-7a, b, 1-8a) partly filled with sparitic cement, fine-grained carbonate, and pulverized carbonate in the clay/silt grain size fractions. Within the domains along the damage-zone fault core contact, displayed by samples Atlitz1 and Atlitz2,  $F_{max}$  and  $F_{min}$  of joint- bounded slices are significantly smaller than in the samples described above. In particular  $F_{max}$  decreases due to fragmentation. In these domains,  $F_{max}$  reaches mean values between 13.6 and 17.7 mm (Tab. 1-1), so the  $F_{max}/F_{min}$  ratio is about 1.7 (Tab. 1-1).

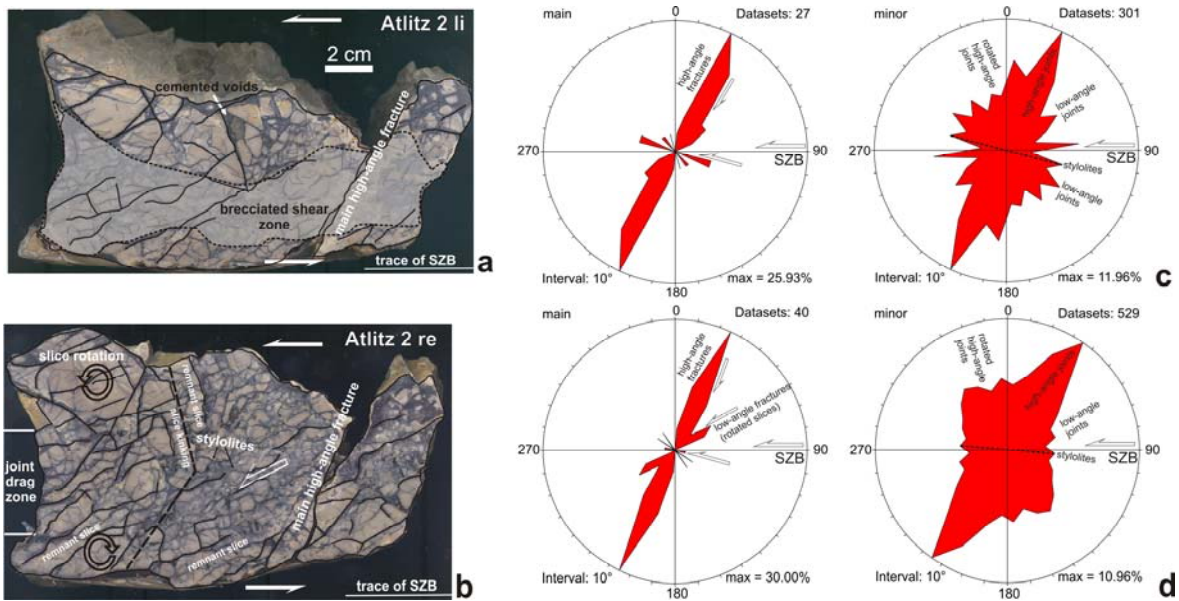


Figure 1-7: (a), (b) Fracture pattern within carbonate rocks along the Talhof fault damage zone at a distance of approximately 25 cm (a) and 20 cm (b) to the damage zone – fault core contact, showing the increasing rotation of joint- bounded slices along a zone of joint drag and slice kinking towards the fault core. In the lower parts of the samples slices rotate into a low-angle orientation as well. Thick lines: major fractures, thin lines: minor fractures. The shear zone boundary (SZB) runs parallel to the bedding/foliation. (c), (d) The Rose diagrams display the orientation of the distribution of major and minor fractures relative to the SZB. Arrows indicate the displacement along reactivated structural elements. Sample from site “Atlitz” (see Appendix).



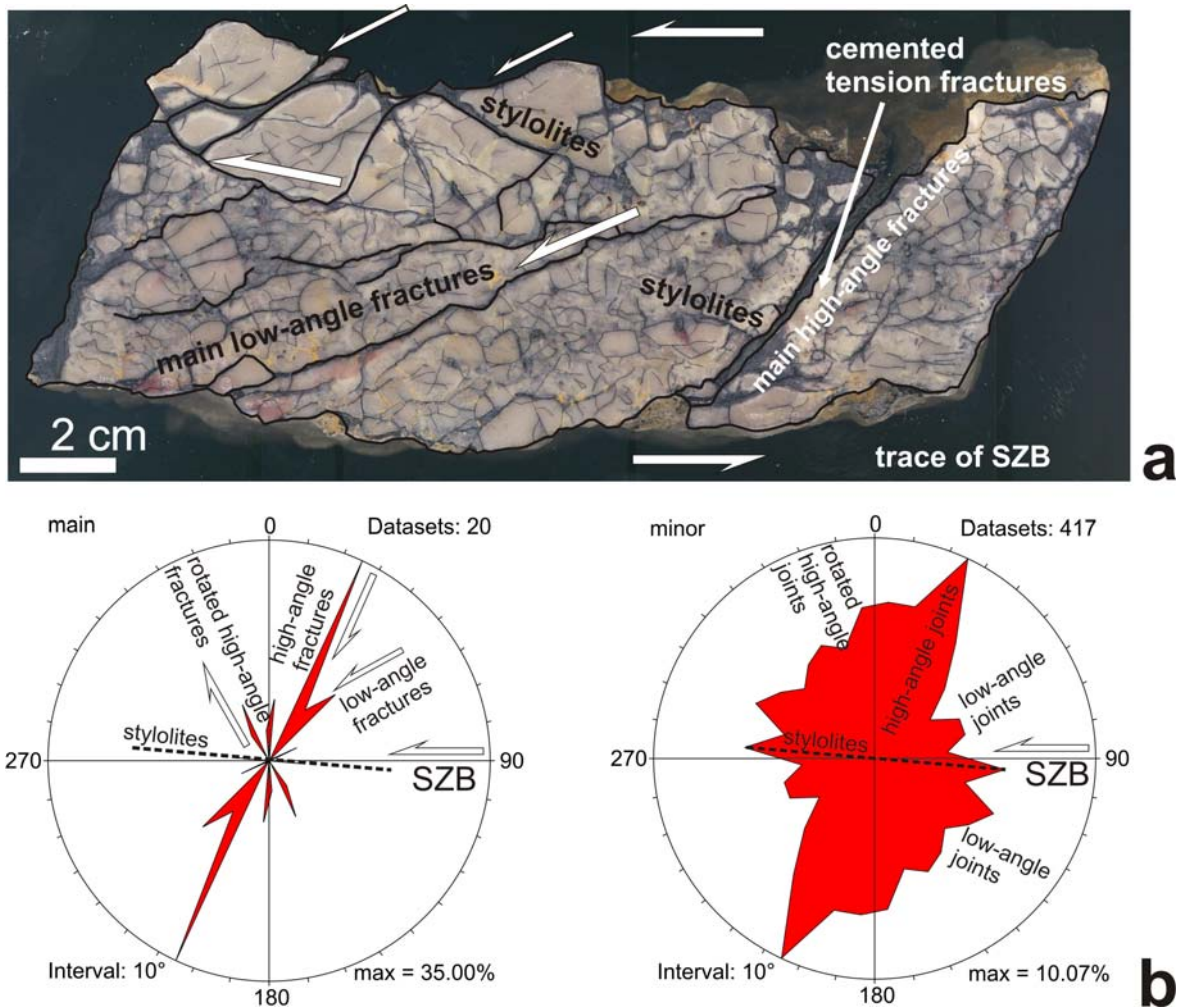


Figure 1-8: (a) Fracture pattern within carbonate rocks along the Talhof fault damage zone at a distance of approximately 15 cm (a) and 10 cm (b) to the damage zone – fault core contact, showing the increasing occurrence of main joint- bounded slices at a low-angle orientation to the SZB, and the subsequent development of slice-internal fractures, mainly at a high-angle orientation. Stylolites predominantly form at low angles, 10-15° clockwise to the SZB. thick lines: major fractures, thin lines: minor joints. Also note the increasing fragmentation of joint- bounded slices related to the formation of minor joints. The SZB runs parallel to the bedding/foliation. (c), (d) The Rose diagrams display the orientation of the distribution of major and minor fractures relative to the SZB. Arrows indicate the displacement along reactivated structural elements. Sample from site “Atlitz” (see Appendix).

## 1.8 Fault rocks along the damage zone–fault core boundary

The fault rocks (coarse-grained cataclasite, fault breccia) are characterized by an irregular grain-size distribution (Figs. 1-9, 1-10). SHWK2 is entirely made up of a medium-grained cemented cataclasite. Talhof5 is characterized by two distinct domains (Fig. 1-9). The portions immediately adjacent to the fault plane consist of medium-grained carbonate cataclasites, those near the damage zone grade into a grain-supported fault breccia.



Remnants of former joint-bounded slices are still observable (Fig. 1-9a). Usually, the fragments are characterized by polygonal shapes and show irregular, angular to slightly rounded, boundaries.

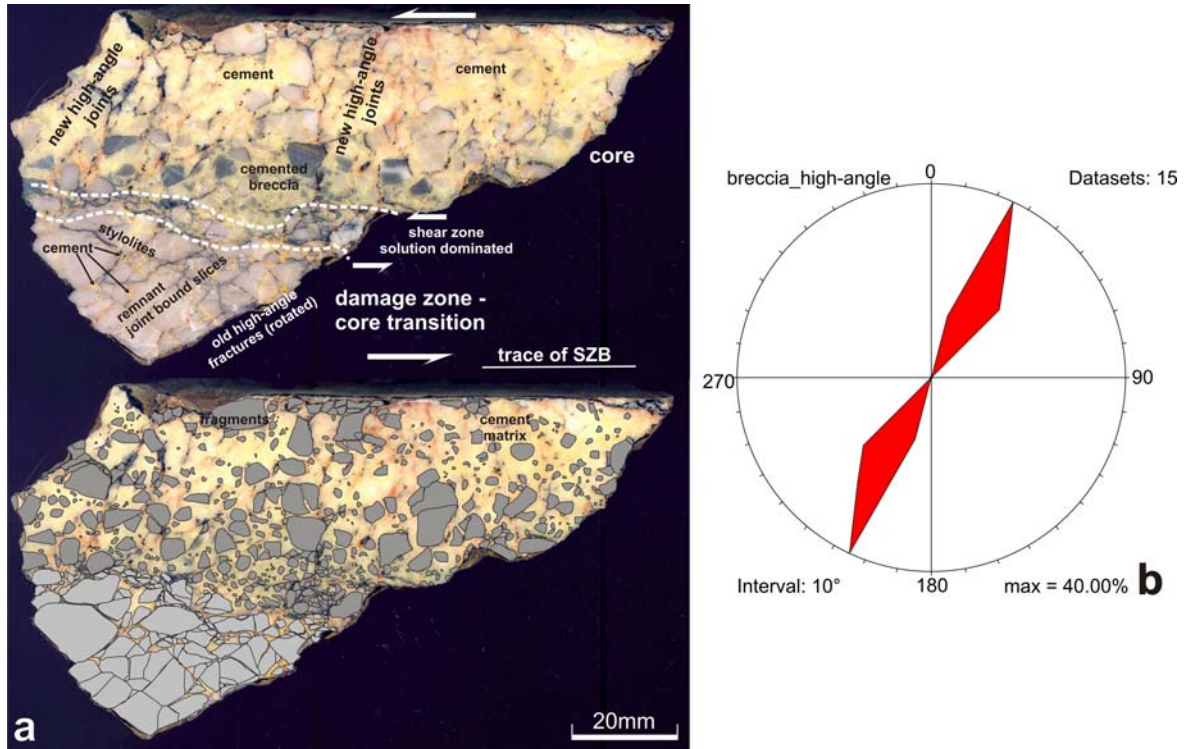


Figure 1-9: (a) Cemented fault core breccia, with analyzed cataclasite fragments (below) (sample Talhof 5, site “Stiegerinhütte”). The domain in the lower part of the sample mainly comprises fragmented joint-bounded slices, the domain in the upper part a mainly matrix supported cataclasite. These domains are separated by a zone of closely spaced stylolites. The shear zone boundary (SZB) runs parallel to the bedding/foliation. Stylolites predominantly form at low angles, 10-15° clockwise to the SZB. Note that the cemented breccia is crosscut by high-angle joints at an orientation of 75° anti-clockwise from the SZB. (b) The rose diagram displays the orientation of the distribution of high-angle joints crosscutting the cemented fault breccia. For sample site see Appendix and Fig. 1-3. Arrows indicate the displacement along reactivated structural elements.

The fault rocks show an exponential fragment-size distribution (Fig. 1-10). Within the cemented cataclasite, the size of the fragments varies between 0.1 and 11 mm ( $F_{max}$ ), with a mean of 1.74 mm, and between 0.05 mm and 6.5 mm ( $F_{min}$ ), with a mean of 1.03. Fragment to fragment contacts are observed only close to the damage zone. Towards the fault core, fragment to fragment contacts may hardly be detected. The section area covered by fragments within the cemented cataclasites averages approximately 33.5 to 38%. This fault rock is crosscut by high-angle joints with respect to the SZB (Fig. 1-9). These joints are spaced at approximately 1 cm. This arrangement resulted in the development of new joint-bounded slices within the cataclasites (Fig. 1-9a).

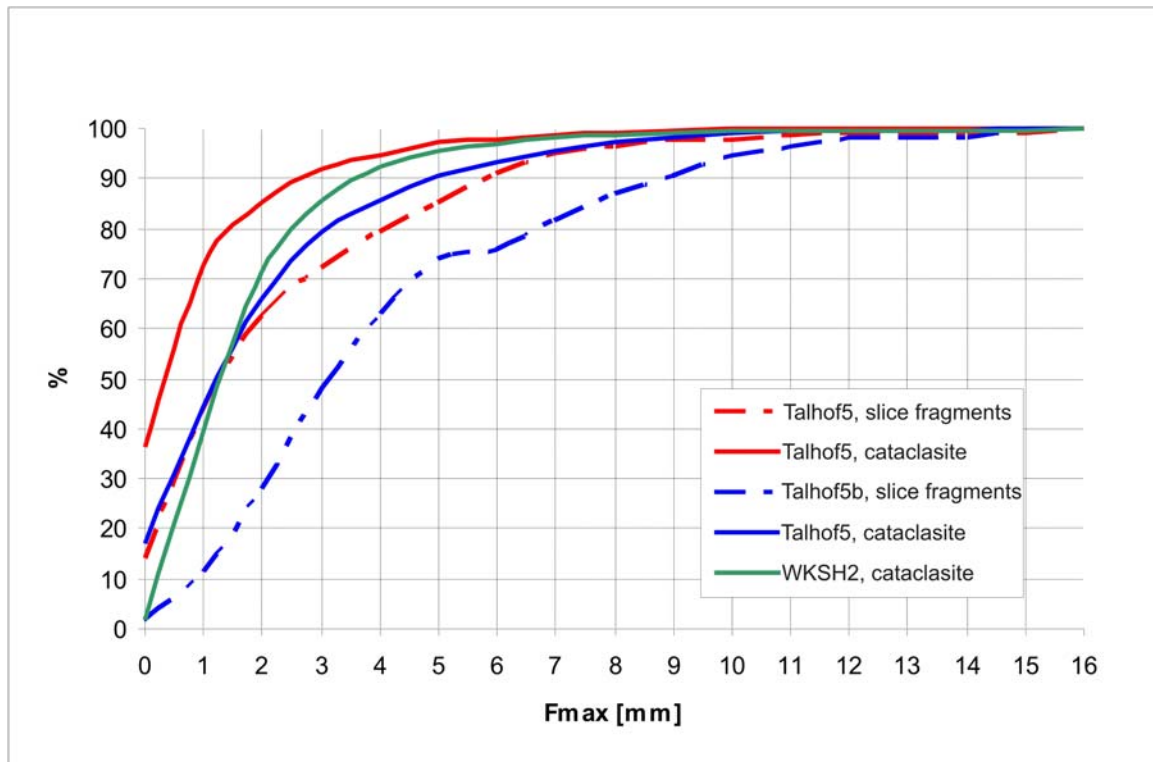


Figure 1-10: Fragment size (maximum diameter  $F_{max}$ ) distribution diagram (fragment size vs. bulk percentage of grains smaller than a given size) of fault core rocks. The sampling sites are displayed in Fig. 3. The distributions for Talhof5 and Talhof5b are given for separate domains, characterized by fragmented fracture- bounded slices and matrix supported cemented cataclasite, respectively (see Fig. 1-9).

The transition from the cataclasite to the damage zone is marked by pressure solution seams. These stylolitic fabrics are oriented at low angles to the SZB (Fig. 1-9a). In this domain (below the shear zone indicated in Fig. 1-9a) relics of slices can be observed, rotated by 30-50° in a clockwise sense with regard to their original orientation. The size of the fragments formed by these structures varies between 0.1 mm and 16 mm ( $F_{max}$ ), with a mean of 3.18 mm, and between 0.05 mm and 10.8 mm ( $F_{min}$ ), with a mean of 1.69. The aspect ratio of the fragments ( $F_{max}/F_{min}$ ) varies between 1.1 and 5.2, with a mean of 1.99. The section area covered by fragments averages approximately 60 - 78 %. These domains are characterized by an exponential fragment size distribution, too. The distribution, however, is more homogenous (Fig. 1-10).

	Structural position	mean $F_{\max}$ (mm)	std.dev. (1 $\sigma$ )	$F_{\min}$ (mm)	std.dev. (1 $\sigma$ )	mean $F_{\max}/F_{\min}$	std. dev. (1 $\sigma$ )	fragment quantity.
<b>Main fractures</b>								
<b>Sample</b>								
Talhof3	DZ-core transition	17.47	9.08	7.47	2.87	2.27	0.70	13
Atlitz re1	DZ-core transition	17.73	9.35	9.52	6.50	2.24	0.78	9
Atlitz2 li	DZ-core transition	13.63	7.66	8.29	4.95	1.71	0.38	12
Atlitz2 re	DZ-core transition	16.92	8.17	9.85	5.74	1.80	0.43	14
Atlitz3 li	DZ	19.35	11.23	7.97	3.77	2.42	0.80	20
Atlitz3 re	DZ	33.85	33.56	14.86	9.37	2.08	0.66	8
Atlitz4 li	DZ	36.88	13.62	15.03	7.03	2.58	0.59	9
Atlitz4 re	DZ	27.70	18.34	9.60	4.54	2.84	0.95	11
Atlitz5 li	DZ	26.10	8.80	11.82	5.88	2.46	0.88	10
Atlitz5 re	DZ	26.07	9.03	10.90	3.89	2.41	0.25	6
<b>Minor fractures</b>								
Talhof3	damage zone-core							
internal	transition	5.14	1.91	2.63	1.09	2.02	0.53	18
internal		3.87	2.08	1.98	1.23	2.15	0.87	24
internal		4.95	2.52	2.99	1.81	1.88	0.67	8
internal		4.07	0.73	2.16	0.56	1.97	0.49	9
internal		6.65	3.86	2.88	1.82	2.40	0.62	11
internal		3.86	1.21	2.28	0.46	1.68	0.32	8
internal		4.35	1.59	2.05	0.63	2.16	0.54	16
internal		4.81	2.20	2.55	1.30	2.03	0.71	42
internal		4.46	3.11	3.61	1.83	1.87	0.46	6
internal		3.58	0.60	2.33	0.76	1.60	0.33	7
internal		5.04	1.8	2.66	1.11	2.07	0.85	23
internal		6.14	1.72	2.89	1.16	2.20	0.28	3
internal		4.67	2.02	2.46	0.61	1.89	0.57	19
bulk		4.61	2.20	2.41	1.17	1.94	0.69	194
Atlitz re1	DZ-core transition	7.34	5.25	4.3	3.06	1.76	0.50	113
Atlitz2 li	DZ-core transition	8.73	4.79	4.74	2.64	1.90	0.53	103
Atlitz2 re	DZ-core transition	7.66	4.44	4.01	1.94	1.95	0.63	166
Atlitz3 li	DZ	8.10	4.46	4.35	2.16	1.96	0.70	211
Atlitz3 re	DZ	8.21	3.51	4.27	2.06	2.05	0.63	150
Atlitz4 li	DZ	9.63	4.94	4.71	2.36	2.14	0.72	145
Atlitz4 re	DZ	8.17	3.79	4.42	2.27	1.96	0.55	171
Atlitz5 li	DZ	8.64	4.45	4.53	2.27	2.01	0.64	135
Atlitz5 re	DZ	8.45	3.86	4.77	2.41	1.86	0.55	177

Table 1-1: Maximum ( $F_{\max}$ ) and minimum ( $F_{\min}$ ) diameters of fracture- bounded fragments from samples taken along the Talhof fault damage zone. The diameters were determined by measuring the distances between two parallel tangents to the fragment margins at opposite points.

Exemplified for sample Talhof3 the dimensions of fragments bounded by minor joints are displayed as well (data from the other samples are not displayed here mainly for space reasons, but are available from the corresponding author). For the bulk samples the  $F_{\max}/F_{\min}$  ratios obtain a constant value around 2 within the 1  $\sigma$  standard deviation.

DZ: damage zone.

## 1.9 Oxygen and carbon stable isotope compositions

Powder samples were obtained by microdrilling of the rock specimens described above. These samples were analyzed by stable isotope geochemistry in order to determine the isotopic composition of (1) host rock- derived slices within the damage zones (Figs. 1-4 to 1-9), of (2) cataclasite fragments and (3) fault rock cements (Fig. 1-9). The analytical techniques are described in the Appendix, carbon and oxygen isotopic ratios are plotted in Fig. 11 and listed in Tab. 1-2.  $\delta^{13}\text{C}$  and  $\delta^{18}\text{O}$  isotope analysis provides the characterization of the isotopic signature of fault-related calcites, and the origin of the fluids from which these calcite phases were precipitated (e.g., Kerrich, 1986; Pili et al., 2002).

The slice- dominated samples show two different types of sparitic cement located in voids and pull-aparts between fracture- bounded slices. The slice fragments have carbon ( $\delta^{13}\text{C}$ ) and oxygen ( $\delta^{18}\text{O}$ ) isotope values ranging from +3.18 ‰ to 3.46 ‰ and -6.52 ‰ to -6.71 ‰, respectively. The cement isotopic data define a trend in the  $\delta^{13}\text{C}$  -  $\delta^{18}\text{O}$  diagram with increasing  $\delta^{13}\text{C}$  values and decreasing  $\delta^{18}\text{O}$  values towards the fault core (Fig. 11). The cement composition varies between -2.46 ‰ and -2.98 ‰ ( $\delta^{13}\text{C}$ ) and -5.19 ‰ to -6.35 ‰ ( $\delta^{18}\text{O}$ ) (white sparitic cement), and -0.71 ‰ to -0.81 ‰ and -5.47 ‰ to -5.90 ‰ (red cement), respectively. Within the fault rocks the isotope composition of the fragments ranges from approximately 0.5 ‰ to 2.9 ‰ ( $\delta^{13}\text{C}$ ) and -5.7 ‰ to -7.8 ‰ ( $\delta^{18}\text{O}$ ). The cement isotope compositions show  $\delta^{13}\text{C}$  values of -0.26 ‰ to 1.08 ‰ and  $\delta^{18}\text{O}$  values of -6.4 ‰ to -9.4 ‰. The relatively low  $\delta^{13}\text{C}$  and  $\delta^{18}\text{O}$  values are typical for carbonate rocks that have precipitated from, or exchanged with, meteoric water at low temperatures (e.g., Kerrich, 1986; Ghisetti et al., 2001). The rather tight range of  $\delta^{13}\text{C}$  values in cements rules out the incorporation of carbon from low  $\delta^{13}\text{C}$  organic sources (e.g., Kerrich, 1986). In general, the cements between slice fragments show significantly lower  $\delta^{13}\text{C}$  values compared to the  $\delta^{13}\text{C}$  isotopic composition of the protolith slices. Cements from the cataclasites, however, show a  $\delta^{13}\text{C}$  isotopic composition more similar to the protolith slices, suggesting that the carbon was derived from the latter.

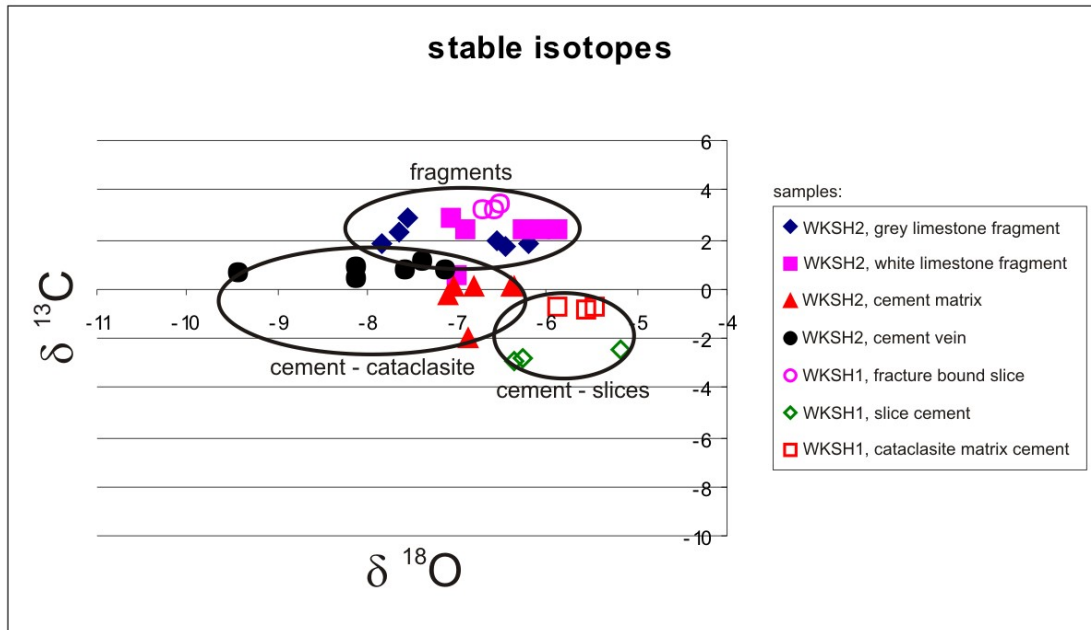


Figure 1-11: Stable isotope compositions ( $\delta^{13}\text{C}$  and  $\delta^{18}\text{O}$  in ‰) of host rock slices from the fault damage zone, fault rock fragments and fault rock cements from the fault core, showing the concordance of cement isotope signatures with increasing fragmentation, i.e. from slice to cataclasite formation. Sample WKSH2 is a matrix-supported cataclasite, WKSH1 consists of cemented fractured slices, both according to the domain description in Fig. 1-9. The sampling sites are displayed in Fig. 1-3.

Apparently, cements between host rock- derived slices are depleted in  $\delta^{18}\text{O}$  with respect to the slices, whereas calcite veins crosscutting cemented cataclasites are partly enriched in  $\delta^{18}\text{O}$ . Matrix cement from the cataclasites show a similar  $\delta^{18}\text{O}$  composition with respect to the host rock- derived fragments, being consistent with local isotopic equilibrium between the cement-forming fluid and these fragments. This process was probably facilitated by the surface-controlled exchange between fluids and fine-grained fragments. The low  $\delta^{18}\text{O}$  values of calcite veins with respect to the host rock- derived fragments indicate that calcite precipitated from fluids with either lower  $\delta^{18}\text{O}$  composition or higher temperatures (e.g., Kerrich, 1986; Marquer and Burkhard, 1992). The similar carbon isotopic compositions of cataclasite fragments and surrounding cements could be due to a mineralizing fluid buffered with the adjacent surrounding cataclastic material (Marquer and Burkhard, 1992; Micarelli et al., 2005). The slight difference in  $\delta^{13}\text{C}$  compositions may reflect the presence of a relatively open system.

Sample		$\delta^{18}\text{O}$ (‰)	$\delta^{13}\text{C}$ (‰)
WKSH2K11	grey limestone fragment	-7.82	1.88
WKSH2K12	grey limestone fragment	-7.55	2.91
WKSH2K13	grey limestone fragment	-7.64	2.28
WKSH2K11-1	grey limestone fragment	-6.21	1.85
WKSH2K11-2	white limestone fragment	-6.56	1.97
WKSH2K11-3	white limestone fragment	-6.45	1.72
WKSH2K14	white limestone fragment	-7.07	2.83
WKSH2K15	white limestone fragment	-6.92	2.44
WKSH2K16	white limestone fragment	-7.01	0.53
WKSH2K15-1	white limestone fragment	-6.26	2.36
WKSH2K15-2	white limestone fragment	-6.07	2.40
WKSH2K15-3	white limestone fragment	-5.87	2.36
WKSH2Z9	sparitic cement	-6.88	-2.00
WKSH2Z10	sparitic cement	-7.05	0.05
WKSH2Z11	sparitic cement	-7.10	-0.26
WKSH2Z10-1	sparitic cement	-6.36	0.08
WKSH2Z10-2	sparitic cement	-6.40	0.04
WKSH2Z10-3	sparitic cement	-6.80	0.03
WKSH2Z12	sparitic cement	-8.12	0.85
WKSH2Z13	sparitic cement	-9.42	0.65
WKSH2Z14	sparitic cement	-8.12	0.38
WKSH2Z12-1	sparitic cement	-7.12	0.82
WKSH2Z12-2	sparitic cement	-7.58	0.79
WKSH2Z12-3	sparitic cement	-7.38	1.08
WKSH1-K-1	slab	-6.60	3.19
WKSH1-K-2	slab	-6.71	3.18
WKSH1-K-3	slab	-6.52	3.46
WKSH1Z-1	white cement between slab	-6.26	-2.86
WKSH1Z-2	white cement between slab	-6.35	-2.98
WKSH1Z-3	white cement between slab	-5.19	-2.46
WKSH1RZ-1	red cement between fragments	-5.47	-0.75
WKSH1RZ-2	red cement between fragments	-5.57	-0.81
WKSH1RZ-3	red cement between fragments	-5.90	-0.71

Table 1-2: Stable isotope composition of host rock lamellae within the Talhof fault damage zone, fault rock fragments and fault rock cements.

## 1.10 Discussion of structural data

### 1.10.1 Implication for the formation of carbonate fault rocks

The structural evolution presented in this study (Fig. 1-12) implies that fault zone development within layered carbonates starts with shearing of the pre-existing composite foliation. This process includes cross jointing between layer-parallel shears (Fig. 1-12a, b). These joints form a penetrative fabric, which is in contrast to some previous examples (e.g., Wilcox et al., 1973; Paterson, 1978; Gamond, 1983, 1987; Naylor et al., 1986; Olson

and Pollard, 1991; Davis et al., 1999; Mollema and Antonelli, 1999; Katz et al., 2004; Kim et al., 2004; Mandl, 2005).

Strain may have been accommodated by sliding along the SZB (foliation planes) without major fracturing and disintegration (Fig. 1-12a), joint drag and bookshelf rotation of joint-bounded slabs, including the shearing of high-angle joints (Fig. 1-12b). As suggested by slice kinking (Fig. 1-12c), the widening of the shear zone was inhibited (e.g., Means, 1995) due to the high ratio between the effective normal stress acting perpendicular to the externally imposed general shear direction ( $\sigma_{\perp}$ ) and the normal stress acting parallel to that direction ( $\sigma_{\parallel}$ ) (e.g., Mandl, 1988, 2000; Wibberley et al., 2000; Brosch & Kurz, in press) (Figs. 1-12b, c). Accordingly, the maximum principal stress is assumed to be oriented at very high angles to the SZB.

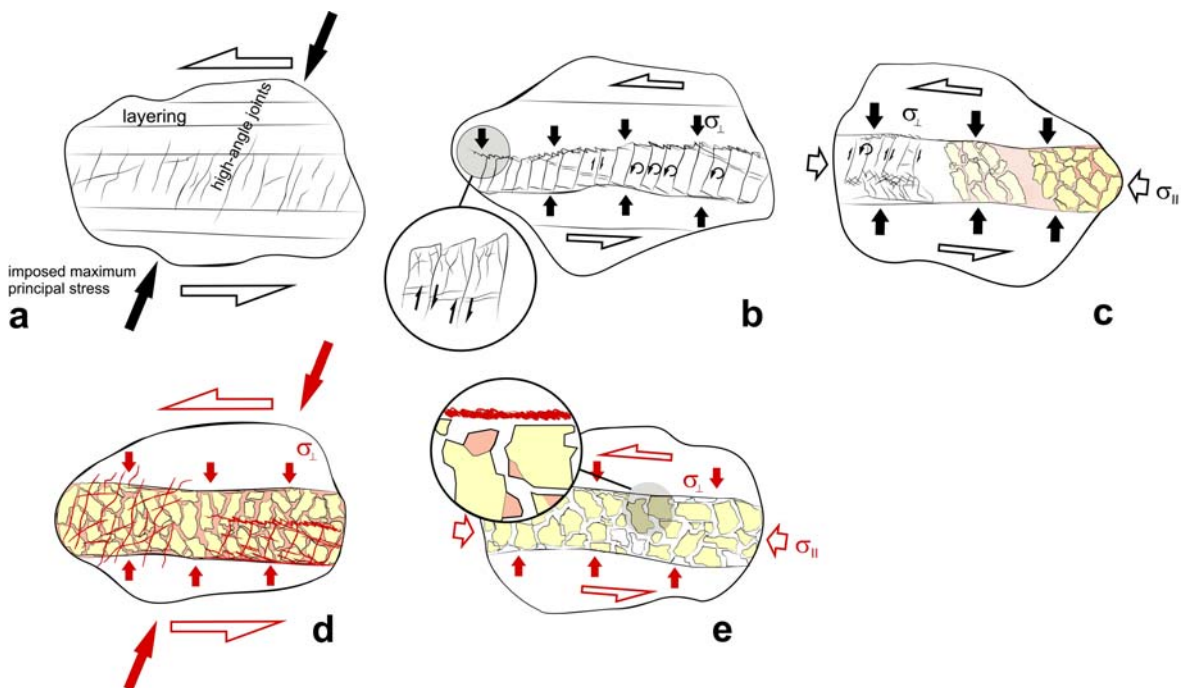


Figure 1-12: Schematic model of shear zone evolution during layer-parallel shear along the Talhof fault deduced from field and sample observations (after Brosch and Kurz, in press). (a) Formation of distinct cross joints at high angles to the pre-existing bedding/foliation planes. (b) Formation of joint-bounded slices, rotation of slices, reactivation of joints as shears with antithetic displacement, and formation of secondary joints at the tips and internal parts of slices. Widening of the fault zone is inhibited by external compressive stresses at high angles to the SZB, stylolites are formed at low angles to the SZB, perpendicular to maximum principal stress orientation. (c) Kinking and disintegration of slices by joint drag and bookshelf rotation, developing into a cataclastic shear zone at advanced stages of displacement. (d) Cementation of disintegrated slices and subsequent formation of new high-angle joints. (e) Second cycle of brecciation. The newly formed fragments consist of both slice fragments and fragments of sparitic cement.  $\sigma_{\perp}$ : effective normal stress acting perpendicular to the externally imposed general shear direction.  $\sigma_{\parallel}$ : effective normal stress acting parallel to the externally imposed general shear direction.

The structures described above are interpreted to represent the initial states in shear zone development. The slices originally bounded by joints approach a constant shape and geometry, defined by the  $F_{\max} / F_{\min}$  ratio (Tab. 1-1). In general, this ratio lies between 2.8 and 2.1, with a mean value of approximately 2.3. Towards the fault core, this ratio decreases. In particular,  $F_{\max}$  shows a strong decrease due to fragmentation and the  $F_{\max}/F_{\min}$  ratio lowers to values of 1.7 (Tab. 1-1). The detection of isolated slice fragments within the fault breccia indicates that these were progressively incorporated into the fault core. Within the fault core cataclasites, however, the mean fragment size decreases continuously (Fig. 1-10). Following Billi et al. (2003), rocks in damage zones adjacent to fault cores show very similar structural fabrics and consist of nearly isometric lithons with a cross-sectional aspect ratio of about 1.4 (despite different sizes, kinematics, and inherited structural fabrics of the protolith). This value was interpreted as the upper limit for the systematic initiation of particle rotation and grinding.

#### **1.10.2 Mechanisms of deformation and grain size reduction**

At temperatures below 250°C calcite mainly deforms by fracturing, jointing, grain-size-sensitive processes such as solution transfer and grain-boundary sliding (Kennedy and Logan, 1998; Kennedy and White, 2001; Mazzoli et al., 2001), and twinning (e.g., Burkhard, 1993). The formation of joints, as well as kinking and cracking, enabled the inflow of fluids into the fault zone. The presence of fluid phases and related fluid pressures generally decreases the effective normal stresses and therefore facilitates fracturing of rocks (e.g., Sibson et al., 1975; Sibson, 1981, 1990, 1992, 1996; Ramsay, 1980; Byerlee, 1993; Janssen et al., 1998; Petit et al., 1999; Tenthorey et al., 2003; Agosta and Aydin, 2006). Fracturing generally results in a reduction of internal stresses within the rock mass, and a reduction of pore fluid pressure. The additional inflow of fluids into the fault zone results in a decrease of shear stresses until the precipitation of solid phases, like sparitic cement, is initiated. This will result in sealing of the fault zone, the build up of fluid pressure, and the potential to transfer stresses across the fault zone. Healing and cementation of the fault zone increase the cohesive strength in terms of hardening and shift the failure envelope to higher values with time. Precipitation of sparitic cements can therefore change the strength and behavior of fault zones via crack healing and sealing (Sibson et al., 1975; Ramsay, 1980; Sibson, 1996; Tenthorey et al., 2003; Tarasewicz et al., 2005; Yasahuara et al., 2005; Collettini et al., 2006).



Highly fractured material along the damage zone – fault core boundary behaved similar to loose, granular material deformed by cataclastic flow. Cementation of cataclasites, however, resulted in strain hardening with the subsequent formation of new high-angle joints (Figs. 1-9, 1-12d, e). Joint formation may therefore be described as a cyclic process of cementation, healing, and re-fracturing. Multiple cyclic fracturing is therefore an important mechanism for the development of isometric grain shapes, and for grain size reduction of host rock- derived fragments within carbonate fault rocks (Figs. 1-9, 1-10). Hardening of the carbonates, however, resulted in the shifting of shear localization towards the un-cemented quartzitic domains, now forming the main fault core. Consequent shear localization in these domains resulted in the development of quartz gouges in fault core domains 2-4 (Fig. 1-3).

### **1.10.3 Implications for fluid - rock interaction and fluid flow**

Stable isotope geochemistry may provide some hints on the origin of the fluids, the fluid-rock ratio, and fluid-rock interaction. The damage zone slices have carbon ( $\delta^{13}\text{C}$ ) and oxygen ( $\delta^{18}\text{O}$ ) isotope values ranging from +3.18 ‰ to 3.46 ‰ and -6.52 ‰ to -6.71 ‰, respectively. These are supposed to reflect the original host rock signature. The cataclasite fragments within the fault core show a similar isotope composition for  $\delta^{18}\text{O}$ . In contrast, several cement compositions deviate significantly from this isotope signature (Fig. 1-11; Tab. 1-2).

Within the cataclasites, the cement isotope compositions show  $\delta^{13}\text{C}$  values of -0.26 ‰ to 1.08 ‰ and  $\delta^{18}\text{O}$  values of -6.4 ‰ to -9.4 ‰, being closer to the signature of the host rock fragments (Fig. 1-11; Tab. 1-2). The rather large range of the  $\delta^{18}\text{O}$  isotopic composition of cements may also indicate a repeated infiltration of different fluids (Janssen et al., 1998). The light  $\delta^{18}\text{O}$  values for calcite veins (Fig. 1-11) are typical of a meteoric- derived fluid from a near-surface source (e.g., Kerrich, 1986). As the fluid that entered the fault zone usually shows a constant isotope composition, the relative position of the individual datum in the  $\delta^{13}\text{C}$  and  $\delta^{18}\text{O}$  trend is more related to variations in the amount of fluids (Kirschner and Kennedy, 2001; Pili et al., 2002; Agosta and Kirschner, 2003). Samples with isotopic values similar to the carbonate host rocks either interacted with small quantities of fluid, or precipitated from a fluid that had previously equilibrated with the host rock. Conversely, samples with lower isotopic values either interacted with larger quantities of fluid, or precipitated from a fluid that had partly retained its original isotopic values (Agosta and Kirschner, 2003).

This evolution of the isotopic composition indicates four main points:

- (1) Within the damage zone, a high fluid – rock ratio prohibited the complete isotopic homogenization between host rock- derived slices and fluids. This might alternatively also be interpreted in terms of enhanced fluid flow along, or across, the damage zone rather than in terms of a stagnating fluid.
- (2) Within the cataclasites, the fluid-rock ratio was low, resulting in a buffered isotopic signature composition. Alternatively, the reduced fragment size, and increased surface area within the cataclasites caused this isotope homogenization.
- (3) The fact that only a few joints are healed while all cataclasites are cemented suggests either a rapid opening of joints (hydraulic fracturing) (Beach, 1980; Ramsay, 1980; Sibson, 1981), or preferential fluid flow within the fault core (Bussolotto et al., 2007).
- (4) Meteoric water is one of the more common fluids in the earth's crust with sufficiently low  $\delta^{13}\text{C}$  and  $\delta^{18}\text{O}$  values to account for the low isotopic values of calcite precipitated at low temperatures (Kerrich, 1986; Marquer and Burkhard, 1992; Janssen et al., 1998; Agosta and Kirschner, 2003). Although not definitive, the incursion of deeply sourced  $\text{CO}_2$ -bearing fluids (e.g., from mantle, or metamorphic decarbonation of limestones) into the studied fault zone is neither supported by the observed structures, nor from the isotopic data

Within the fault zone carbonates, the large range in  $\delta^{18}\text{O}$  values indicates considerable fluid-rock interaction. Cementation and sealing may also have resulted in diminishing the replenishment of fluids into the carbonates, but increased infiltration of the adjacent quartzite domains. The negligible contents of carbonate cements in domains 2-4 (Fig. 1-3) (Kiechl, 2007) also indicate that these domains were not infiltrated by carbonate-bearing fluids from the adjacent domain1, and that quartz gouges in domains 2-4 probably acted as a barrier to fluid flow. These fluids were therefore entrapped in the carbonate domains along the damage zone – fault core boundary. Both cementation and the adjacent barrier therefore gave rise to elevated fluid pressures in the carbonate domains, convenient for subsequent frictional failure, and the development of a temporally open system being accessible for fluid infiltration.

## 1.11 Conclusions

- (1) In anisotropic rocks with layer parallel shear, formation of cataclastic shear zones may start with the development of cross joints at high angles to the shear zone boundary

(SZB). This results in the formation of joint bound, closely spaced slices, forming a penetrative fabric at the scale of the shear zone.

(2) The predominance of discontinuities parallel to the general shear direction (layering, foliation) and of high-angle cross joints do not immediately require the incipient generation of shear fractures for strain accommodation at low angles to the shear zone.

(3) The formation of slices bounded by en-echelon joints at high angle to the SZB was probably due to the influence of the high ratio of effective normal stresses acting orthogonal to the normal stresses parallel to the SZB. Slice rotation, associated with inhibited widening of the shear zone, led to joint drag and kinking with subsequent cataclasis.

(4) Rupturing along kink zones and breaking-up to smaller fragments with rotational and translational displacement mark the transition to cataclastic flow. This is interpreted to represent the initial states in the development of a brittle shear zone in anisotropic rocks. Subsequent shear is localized along these zones, ending up with the evolution of a fault core.

(5) Formation of joint- bounded slices may proceed repeatedly in the case that breccias get cemented and, subsequently, undergo continuous brittle deformation in terms of a cyclic process of healing and fracturing. This enforces the development of isometric shapes of host rock- derived fragments, and is one of the main mechanisms of fragment size reduction.

(6) Stable isotope compositions ( $\delta^{13}\text{C}$  and  $\delta^{18}\text{O}$ ) indicate that fault cements most probably precipitated from meteoric- derived fluids infiltrating the fault zone. The fluid–rock ratio decreases towards the fault core, displayed by the continuous homogenization of the isotope signatures from the damage zone towards the fault core.

(7) Cementation and sealing resulted in diminishing fluid flow through the carbonates, and in the development of a temporally closed system because of the low cataclasite porosity. This process may have resulted in shear localization in adjacent gouge domains.

(8) The cyclic change between fluid infiltration, due to brittle failure, and cataclasite cementation implies a cyclic change between an open and a closed system.

## 1.12 Acknowledgements

This study has been carried out during a research project (P 17697-N10) granted by the Austrian Science Fund (FWF). We greatly appreciate the field-work support by Heiko Gaich and Gerfried Winkler. The formal reviews by David Peacock and Fabrizio Storti

contributed a lot to the improvement of the first manuscript version. Fabrizio Agosta and Emanuele Tondi are thanked for their thorough editorial comments.

### 1.13 Appendix

#### *Analytical techniques*

Oxygen and carbon isotope ratios were measured in the isotope lab of the Institute of Earth Sciences (University of Graz) with a „Delta-Plus“ mass spectrometer equipped with a dual inlet system, and at the Joanneum Research Forschungsgesellschaft mbH (Graz, Austria). These systems provide a continuous-flow isotope ratio mass spectrometric analysis. Isotope extraction from calcite was performed using the commercial “Kiel II” system. The analyses were calibrated against NBS28 (quartz), and NBS18 (calcite) standards (IAEA). Oxygen data are displayed as  $\delta^{18}\text{O}$  with respect to Standard Mean Ocean Water (SMOW).

Phosphoric acid is added dropwise into individual sample vials by a fully automated acid dosing system. The evolved  $\text{CO}_2$  is slowly passed through a sampling loop in a trickling stream of helium. Repetitive loop injections onto an isothermal GC column create a series of pulses of pure  $\text{CO}_2$  in He, which enter the IRMS via an open split. An overall precision of 0.08 ‰ for  $\delta^{18}\text{O}$  and of 0.06 ‰ for  $\delta^{13}\text{C}$  has been achieved.

#### *Experimental conditions*

Borosilicate sample bottles are washed in diluted acid, then twice in de-ionized water and overnight dried at 70°C. After adding the samples to the vials in air, they are sealed using unused septa. Residual air is removed from the sample vials by automated autosampler-assisted flushing with He, using a flow of 100 ml/min of He for 5 minutes. The phosphoric acid, which is maintained at the reaction temperature, is added dropwise under computer control to each individual reaction vessel. In these experiments, 3 drops of acid were added to each sample prior to measurement. A reaction time of 60 minutes was used. Both the amount of the acid and the reaction time are controlled by the software.

#### *Corrections applied for different sample sizes:*

Data were extracted to an EXCEL file by using the ISODAT NT EXCEL export utility and further calculation steps were carried out using a predefined EXCEL Worksheet. The small linear dependence of  $\delta^{18}\text{O}$  on increasing peak intensities (within the linearity specifications of the DELTAplus) was corrected using a linearity factor (the slope of a line

in m/z 44 intensity vs.  $\delta^{18}\text{O}$ ). The slope determined is small for  $\delta^{18}\text{O}$  (0.015 ‰/nA). For  $\delta^{13}\text{C}$ , no slope correction was applied.

*Coordinates of sites and sampling locations:*

“Stiegerinhütte”: Topographic map of Austria, 1:50000, sheet no. 104 (Mürzzuschlag); 15° 44' 29" E; 47° 39' 17" N.

„Atlitz Topographic map of Austria, 1:50000, sheet no. 104 (Mürzzuschlag); 15° 47' 23" E; 47° 39' 28" N.

## 1.14 References

- Agosta, F., Aydin, A., 2006. Architecture and deformation mechanism of a basin-bounding normal fault in Mesozoic platform carbonates, central Italy. *Journal of Structural Geology* 28, 1445-1467.
- Agosta, F., Kirschner, D. L., 2003. Fluid conduits in carbonate-hosted seismogenic normal faults of central Italy. *Journal of Geophysical Research* 108, 2002JB002013.
- Anderson, E. M., 1951. *The Dynamics of Faulting*. Oliver & Boyd, Edinburgh, 206 pp.
- Aydin, A., Schultz, R., 1990. Effect of mechanical interaction on the development of strike-slip faults with echelon patterns. *Journal of Structural Geology* 12, 123-129.
- Beach, A., 1980. Numerical models of hydraulic fracturing and the interpretation of syntectonic veins. *Journal of Structural Geology* 2, 425-438.
- Billi, A., 2005. Grain size distribution and thickness of breccia and gouge zones from thin (<1 m) strike-slip fault cores in limestone. *Journal of Structural Geology* 27, 1823-1837.
- Billi, A., 2007. On the extent of size range and power law scaling for particles of natural carbonate fault cores. *Journal of Structural Geology* 29, 1512-1521.
- Billi, A., Salvini, F., Storti, F., 2003. The damage zone-fault core transition in carbonate rocks: implications for fault growth, structure and permeability. *Journal of Structural Geology* 25, 1779-1794.
- Billi, A., Storti, F., Salvini, F., 2003. Particle size distributions of fault rocks and fault transpression: are they related? *Terra Nova* 15, 61-66.

- Billi, A., Storti, F., 2004. Fractal distribution of particle size in carbonate cataclastic rocks from the core of a regional strike-slip fault zone. *Tectonophysics* 384, 115-128.
- Brosch, F. J., Kurz, W., in press. Fault damage zones dominated by high-angle fractures within layer-parallel brittle shear zones: examples from the Eastern Alps. *Geological Society of London Special Publication* in press.
- Burkhard, M., 1993. Calcite twins, their geometry, appearance and significance as stress-strain markers and indicators of tectonic regime: a review. *Journal of Structural Geology* 15, 355-368.
- Bussolotto, M., Benedicto, A., Invernizzi, C., Micarelli, L., Plagnes, V., Deiana, G., 2007. Deformation features within an active normal fault zone in carbonate rocks: The Gubbio fault (Central Apennines, Italy). *Journal of Structural Geology* 29, 2017-2037.
- Byerlee, J., 1993. Model for episodic flow of high-pressure water in fault zones before earth-quakes. *Geology* 21, 303-306.
- Caine, J. S., Evans, J. P., Forster, C. B., 1996. Fault zone architecture and permeability structure. *Geology* 24, 1025-1028.
- Caine, J. S., Foster, C. B., 1999. Fault zone architecture and fluid flow: insights from field data and numerical modelling. In: Haneberg, W. C., Mozley, P. S., Moore, J. C. , Goodwin, L. B. (eds.), *Faults and Subsurface Fluid Flow in the Shallow Crust*. Geophysical Monograph, American Geophysical Union 113, 101-127.
- Chester, F. M., Evans, J. P., Biegel, R. L., 1993. Internal structure and weakening mechanisms of the San Andreas. *Journal of Geophysical Research* 98, 771-786.
- Chester, F. M., Logan, J. M., 1986. Implications for mechanical properties of brittle faults from observations of the Punchbowl Fault, California. *Pure and Applied Geophysics* 124, 79-106.
- Chester, F. M., Logan, J. M., 1987. Composite planar fabric of gouge from the Punchbowl Fault, California. *Journal of Structural Geology* 9, 621-634.
- Chester, F. M., Logan, J. M., 1990. Frictional faulting in polycrystalline halite: correlation of microstructure, mechanism of slip and constitutive behavior. *American Geophysical Monographs* 56, 49-56.
- Collettini, C., De Paola, N., Holdsworth, R. E., Barchi, M. R., 2006. The development and behavior of low-angle normal faults during Cenozoic asymmetric extension in the Northern Apennines, Italy. *Journal of Structural Geology* 28, 333-352.

- Davis, G. A., Bump, A. P., Garcia, P. E., Ahlgren, S. G., 1999. Conjugate Riedel deformation band shear zones. *Journal of Structural Geology* 22, 169-190.
- Decker, K., Meschede, M., Ring, U., 1993. Fault slip analysis along the northern margin of the Eastern Alps (Molasse, Helvetic nappes, North and South Penninic flysch, and Northern Calcareous Alps). *Tectonophysics* 223, 291-312.
- Decker, K., Peresson, H., 1996. Tertiary kinematics in the Alpine-Carpathian-Pannonian system: links between thrusting, transform faulting and crustal extension. In: Wessely, G., Liebl, W. (eds.), *Oil and Gas in Alpidic Thrustbelts and Basins of Central and Eastern Europe*. EAGE Special Publication, 69-77.
- Faulkner, D. R., Lewis, A. C., Rutter, E. H., 2003. On the internal structure and mechanics of large strike-slip fault zones: field observations of the Carboneras fault in southeastern Spain. *Tectonophysics* 367, 235-251.
- Frisch, W., Dunkl, I., Kuhlemann, J., 2000. Post-collisional orogen-parallel large-scale extension in the Eastern Alps. *Tectonophysics* 327, 239-265.
- Gamond, J.F., 1983. Displacement features associated with fault zones: a comparison between observed examples and experimental models. *Journal of Structural Geology* 5, 33-45.
- Gamond, J.F., 1987. Bridge structures as sense of displacement in brittle fault zones. *Journal of Structural Geology* 9, 609-620.
- Ghisetti, F., Kirschner, D. L., Vezzani, L., Agosta, F., 2001. Stable isotope evidence for contrasting paleofluid circulation in thrust faults and normal faults of the central Apennines, Italy. *Journal of Geophysical Research* 106, 8811-8825.
- Gmeindl, M., 1999. Sprödtektonische Strukturanalyse der Talhofstörung (Semmeringgebiet). Diploma Thesis, Institute of Applied Geology, University of Natural Resources and Life Sciences Vienna, 143 pp.
- Hubbert, M. K., Rubey, W. W., 1959. Role of pore fluid pressure in the mechanics of overthrust faulting. *Geological Society of America Bulletin* 70, 115-205.
- Janssen, C., Laube, N., Bau, M., Gray, D. R., 1998. Fluid regime in faulting deformation of the Waratah Fault Zone, Australia, as inferred from major and minor element analyses and stable isotope signatures. *Tectonophysics* 294, 109-130.
- Katz, O., Reches, Z., Baer, G., 2003. Faults and their associated host rock deformation: Part I. Structure of small faults in a quartz-syenite body, southern Israel. *Journal of Structural Geology* 25, 1675-1689.

- Katz, Y., Weinberger, R., Aydin, A., 2004. Geometry and kinematic evolution of Riedel shear structures, Capitol Reef National Park, Utah. *Journal of Structural Geology* 26, 491-501.
- Kennedy, L. A., Logan, J. M., 1998. Microstructures of cataclasites in a limestone-on-shale thrust fault: implications for low-temperature recrystallisation of calcite. *Tectonophysics* 295, 167-186.
- Kennedy, L. A., White, J. C., 2001. Low-temperature recrystallization in calcite: mechanisms and consequences. *Geology* 29, 1027-1030.
- Kerrich, R., 1986. Fluid Infiltration into Fault Zones: Chemical, Isotopic and Mechanical Effects. *Pure and Applied Geophysics* 124, 225-267.
- Kiechl, E., 2007. Die hydrogeologische Wirksamkeit von Störungen und Störungszonen am Beispiel der Talhofstörung (Ostalpen).- Master thesis, Institut für Angewandte Geowissenschaften, Technische Universität Graz, 86 pp.
- Kim, Y.-S., Peacock, D. C. P. Sanderson, D. J., 2004. Fault damage zones. *Journal of Structural Geology* 26, 503-507.
- Kirschner, D. L., Kennedy, L. A., 2001. Limited syntectonic fluid flow in carbonate-hosted thrust faults of the Front Ranges, Canadian Rockies, inferred from stable isotope data and structures. *Journal of Geophysical Research* 106, 8827-8840.
- Kurz, W., Wibberley, C. A. J., Imber, J., Holdsworth, R. E., Collettini, C., in press (2008). The internal structure of fault zones: fluid flow and mechanical properties - Introduction. *Geological Society of London Special Publication* 299, 1-3.
- Linzer, H.-G., Decker, K., Peresson, H., Dell'Mour, R., Frisch, W., 2002. Balancing lateral orogenic float of the Eastern Alps. *Tectonophysics* 354, 211-237.
- Logan, J. M., Dengo, C. A., Higgs, N. G., Wang, Z. Z., 1992. Fabrics of experimental fault zones: their development and relationship to mechanical behavior. In: Evans, B., Wong, T. (eds.), *Fault Mechanics and Transport Properties of Rocks*. Academic Press, San Diego, 33-67.
- Logan, J. M., Friedman, M., Higgs, M., Dengo, C., Shimamoto, T., 1979. Experimental studies of simulated gouge and their application to studies of natural fault zones. *Analysis of Actual Fault Zones in Bedrock, Conference Proceedings VIII*, 305-343.
- Mandl, G., 1988. *Mechanics of Tectonic Faulting. Models and Basic Concepts*. Elsevier, Amsterdam. 407pp.
- Mandl, G., 2000. *Faulting in brittle rocks*. Springer, Berlin, 434 pp.



- Mandl, G., 2005. Rock joints - the mechanical genesis. Springer, Berlin, 221 pp.
- Marquer, D., Burkhard, M., 1992. Fluid circulation, progressive deformation and mass-transfer processes in the upper crust: the example of basement-cover relationships in the External Crystalline Massifs, Switzerland. *Journal of Structural Geology* 14, 1047-1057.
- Mazzoli, S., Zampetti, V., Zuppetta, A., 2001. Very low temperature, natural deformation of fine-grained limestone: a case study from the Lucania region, southern Apennines, Italy. *Geodinamica Acta* 14, 213-230.
- Means, W.D., 1995. Shear zones and rock history. *Tectonophysics* 247, 157-160.
- Micarelli, L., Benedicto, A., Invernizzi, C., Saint-Bezar, B., Michelot, J. L., Vergely, P., 2005. Influence of P/T conditions on the style of normal fault initiation and growth in limestones from the SE-Basin, France. *Journal of Structural Geology* 27, 1577-1598.
- Micarelli, L., Benedicto, A., Wibberley, C. A. J., 2006. Structural evolution and permeability of normal fault zones in highly porous carbonate rocks. *Journal of Structural Geology* 28, 1214-1227.
- Mollema, P. N., Antonelli, M., 1999. Development of strike-slip faults in the dolomites of the Sella Group, Northern Italy. *Journal of Structural Geology* 21, 273-292.
- Naylor, M. A., Mandl, G., Seijpensteijn, C. H., 1986. Fault geometries in basement-induced wrench faulting under different initial stress states. *Journal of Structural Geology* 8, 737-752.
- Olson, J. E., Pollard, D. D., 1991. The initiation and growth of en echelon veins. *Journal of Structural Geology* 13, 595-609.
- Paterson, M. S., 1978. *Experimental Rock Deformation - The Brittle Field*. Springer, Berlin, 254 pp.
- Peacock, D. C. P., Sanderson, D. J., 1992. Effects of layering and anisotropy on fault geometry. *Journal of the Geological Society of London* 149, 792-802.
- Petit, J.-P., Wibberley, C. A. J., Ruiz, G., 1999. 'Crack-seal', slip: a new fault valve mechanism? *Journal of Structural Geology* 21, 1199-1207.
- Pili, E., Poitrasson, F., Gratier, J.-P., 2002. Carbon-oxygen isotope and trace element constraints on how fluids percolate faulted limestones from the San Andreas Fault system: partitioning of fluid sources and pathways. *Chemical Geology* 190, 231-250.

- Ramsay, J. G., 1980. The crack-seal mechanism of rock deformation. *Nature* 284, 135-139.
- Ratschbacher, L., Frisch, W., Linzer, H.-G., Merle, O., 1991. Lateral Extrusion in the Eastern Alps. Part 2: Structural Analyses. *Tectonics* 10, 257-271.
- Ratschbacher, L., Frisch, W., Neubauer, F., Schmid, S. M., Neugebauer, J., 1989. Extension in compressional orogenic belts: The eastern Alps. *Geology* 17, 404-407.
- Reches, Z., 1978. Analyses of faulting in three-dimensional strain field. *Tectonophysics* 47, 109-129.
- Reches, Z., 1983. Faulting of rocks in three-dimensional strain fields; II: Theoretical analyses. *Tectonophysics* 95, 133-156.
- Reches, Z., Dietrich, J. H., 1983. Faulting of rocks in three-dimensional strain fields; I. Failed rocks in polyaxial, servo-control experiments. *Tectonophysics* 95, 111-132.
- Reiter, F., Acs, P., 1996-2001. *Tectonics FP 1.6.2, a 32-bit Windows™-Software for Structural Geology*.
- Riedel, W., 1929. Zur Mechanik geologischer Brucherscheinungen. *Zentralblatt für Mineralogie, Geologie und Paläontologie* 1929B, 354-368.
- Rispoli, R., 1981. Stress fields about strike-slip faults inferred from stylolites and tension gashes. *Tectonophysics* 75, T29-T39.
- Rothery, E., 1988. En echelon vein array development in extension and shear. *Journal of Structural Geology* 10, 63-71.
- Sagy, A., Reches, Z., Roman, I., 2001. Dynamic fracturing: field and experimental observations. *Journal of Structural Geology* 23, 1223-1239.
- Sibson, R. H., 1981. Controls on low-stress hydro-fracture dilatancy in thrust, wrench and normal fault terrains. *Nature* 289, 665-667.
- Sibson, R. H., 1986. Brecciation processes in fault zones: inference from earthquake rupturing. *Pure and Applied Geophysics* 124, 159-175.
- Sibson, R. H., 1990. Conditions for fault-valve behavior. In: Knipe, R. J. Rutter, E. H. (eds), *Deformation Mechanisms, Rheology and Tectonics*. Geological Society of London Special Publication 54, 15-28.
- Sibson, R. H., 1992. Implications on fault-valve behavior for rupture nucleation and recurrence. *Tectonophysics* 211, 283-293.

- Sibson, R. H., 1996. Structural permeability of fluid-driven fault-fracture meshes. *Journal of Structural Geology* 18, 1031-1042.
- Sibson, R. H., Moore, J. M., Rankin, A. H., 1975. Seismic pumping - a hydrothermal fluid transport mechanism. *Journal of the Geological Society of London* 131, 653-659.
- Storti, F., Billi, A., Salvini, F., 2003. Particle size distributions in natural carbonate fault rocks: insights for non-self-similar cataclasis. *Earth and Planetary Science Letters* 206, 173-186.
- Tarasewicz, J. P. T., Woodcock, N. H., Dickson, J. A. D., 2005. Carbonate dilation breccias: Examples from the damage zone to the Dent Fault, northwest England. *Geological Society of America Bulletin* 117, 736-745.
- Tchalenko, J. S., 1970. Similarities between shear zones of different magnitudes. *Geological Society of America Bulletin* 81, 1625-1640.
- Tenthorey, E., Cox, S. F., Toff, H. F., 2003. Evolution of strength recovery and permeability during fluid-rock reaction in experimental fault zones. *Earth and Planetary Science Letters* 206, 161-172.
- Vermilye, J.M., Scholz, C.H., 1998. The process zone: a microstructural view of fault growth. *Journal of Geophysical Research* 103, 12223-12237.
- Wang, X., Neubauer, F., 1998. Orogen-parallel strike-slip faults bordering metamorphic core complexes: the Salzach-Enns fault zone in the Eastern Alps, Austria. *Journal of Structural Geology* 20, 799-818.
- Wibberley, C. A. J., Shimamoto, T., 2003. Internal structure and permeability of major strike-slip fault zones: the Median Tectonic Line in Mie Prefecture, Southwest Japan. *Journal of Structural Geology* 25, 59-78.
- Wibberley, C. A. J., Petit, J.-P., Rives, T., 2000. Micromechanics of shear rupture and the control of normal stress. *Journal of Structural Geology* 22, 411-427.
- Wilcox, R. E., Harding, T. P., Seely, D. R., 1973. Basic wrench tectonics. *American Association of Petroleum Geologists Bulletin* 57, 74-96.
- Willemsse, E. J. M., Peacock, D. C. P., Aydin, A., 1997. Nucleation and growth of strike-slip faults in limestones from Somerset, U.K. *Journal of Structural Geology* 19, 1461-1477.
- Yasuhara, H., Marone, C., Elsworth, D., 2005. Fault zone restrengthening and frictional healing: The role of pressure solution. *Journal of Geophysical Research* 110, 2004JB003327.

## **2 Cataclastic faults along the SEMP fault system (Eastern Alps, Austria) – a contribution to fault zone evolution, internal structure and palaeo-stresses.**

Submitted to Tectonophysics, January 2013

Stefan HAUSEGGER\*, Walter KURZ\*\*

\* Graz University of Technology, Institute of Applied Geosciences, Rechbauerstrasse 12, A-8010 GRAZ, Austria

\*\* University of Graz, Institute of Earth Sciences, Heinrichstrasse 26, A-8010 GRAZ, Austria

### **2.1 Abstract**

In this study three different sites along the ENE-trending, sinistral Salzach-Ennstal-Mariazell-Puchberg (SEMP) fault zone were investigated with respect to brittle fault zone evolution and fault re-activation. All sites crop out in Triassic carbonates (Ladinian Wetterstein limestone/ -dolomite). Simultaneously (re-) activated faults were investigated with focus on fault-slip data and structural inventory of each individual fault zone. Configuration of (internal) structural elements, fault core thickness, strike direction and slip sense in addition to particle analysis of fault core cataclasites add up to three different fault types (Fault type I, II and III).

Fault type I is classified by a complex internal fault core structure with thicknesses up to several 10s of meters and generally evolve in a strike direction of maximum shear stress ( $\tau_{max}$ ). Type II faults, characterized by cataclastic fault cores with thicknesses up to 1m, as well as type III faults (thin solitary cataclastic layers) evolve sub-parallel to the main fault direction and in orientation according to R, R' or X shear fractures with variable ( $\sigma_n / \tau$ ) ratio. Progressive development from type III to type II and type I faults is consistent with increasing displacement and increasing fault core width.

Fault type classification and related paleostress analysis provides evidence from field observation compared to theoretical and analogue models of Mohr-Coulomb fracture evolution.

**Keywords:** Cataclasite, Brittle faults, Fault zone evolution, Northern Calcareous Alps.

## 2.2 Introduction

The structural evolution and related deformation mechanisms at brittle conditions in carbonate rocks have been of keen interest in the past decades. Numerous authors have contributed to this topic using different approaches (e.g., Antonellini et al., 1994; Billi et al., 2003; Billi and Storti, 2004; Caine et al., 1996; Caine et al., 1993; Chester and Logan, 1986; Dooley and Schreurs, 2012; Evans et al., 1997; Faulkner et al., 2010; Faulkner et al., 2008; Gudmundsson, 2000; Renshaw, 1996; Shipton and Cowie, 2003; Sibson, 1977; Sibson, 1996; Storti et al., 2003; Wibberley et al., 2000) as for example from field studies, analogue models, and numerical modeling.

Brittle fault zones typically show a complex internal structure with a continuous change in structural characteristics along strike and depth (Aydin and Berryman, 2010; Bonson et al., 2007; Chambon et al., 2006; Childs et al., 2009; Dooley and Schreurs, 2012; Faulkner et al., 2008; Faulkner and Rutter, 2003; Storti et al., 2001; Wibberley et al., 2008).

Concerning cross sections through brittle fault zones, the internal structure usually can be sub-divided into a host rock domain, a damage zone, a transition zone and a fault core (following e.g., Billi et al., 2003; Caine et al., 1996; Caine and Foster, 1999; Chester and Logan, 1986; Childs et al., 2009; Faulkner et al., 2010; Kim et al., 2004).

The width and elongation of these distinct domains along strike, however, is highly variable and may depend on the lithology of the protolith, displacement along the fault zone, strain rate, the orientation of principal stresses relative to the fault zone, and the magnitude of differential (effective) stress as well as shear and normal stresses and fluid pressure (for summary, see Faulkner et al., 2010).

Kinematics of brittle faults and the formation of related secondary fractures are preferably referenced with Riedel shearing (e.g., Ahlgren, 2001; Cladouhos, 1999; Davis et al., 2000; Elter et al., 2011; Katz et al., 2004; Misra et al., 2009). This prevalent concept was first described by Cloos (1928) and Riedel (1929) in clay-cake deformation experiments which led to the basic understanding of brittle fault pattern development and was also applied to Mohr-Coulomb fracture mechanics (Chester and Logan, 1986).

The structural evolution and geometry of brittle fault elements have been investigated in detail through both field studies (e.g., Agosta and Aydin, 2006; Bastesen et al., 2010; Billi et al., 2003; Caine and Foster, 1999; Collettini et al., 2006; Faulkner et al., 2003; Salvani et al., 1999; Storti et al., 2001; Wibberley and Shimamoto, 2003) and laboratory experiments (e.g., Chambon et al., 2006; Del Ventisette et al., 2006; Dooley and

Schreurs, 2012; Dresen, 1991; Misra et al., 2009). Evaluation of field observations and experimental results (Cladouhos, 1999; Davis et al., 2000; Dooley and Schreurs, 2012; Dresen, 1991; Misra et al., 2009) show variations in the arrangement and orientation with respect to the classical fault pattern after Riedel (1929). Passive rotation after fault development, changes in boundary conditions during fault formation (change of the stress field) and material properties (changes of rheology) influence the formation and orientation of Riedel type structures.

In this study, three sites in the Northern Calcareous Alps (Austria) with fault zone dominated by strike-slip displacement were investigated with emphasis on the development of cataclastic fault cores and the related deformation-related structures of the fault cores and the adjacent damage zones. The fault type classification in this study was defined following the Riedel-shear geometry based on Mohr-Coulomb fracture mechanics (Chester and Logan, 1986). Orientation analysis of principal stress orientations and semi-quantitative evaluations of normal and shear stresses follow these assumptions as well.

### **2.3 Methods**

Study areas were determined by large-scale field mapping with focus on localizing cataclastic shear zones. Further structural analysis of this primary data pool led to the selected sites of this work. Subsequent small-scale mapping with emphasis on brittle structures was the key aspect of field data acquisition.

Samples were taken from all structural domains of each investigated fault zone (host rock/damage zone, transition zone and fault core). In-cohesive and highly fractured specimens were stabilized with synthetic resin. All samples were saw-cut in several sections with respect to the orientation of the related fault zone, coated with clear lacquer and scanned in high resolution (600dpi) for further image and particle analysis.

Particle size analysis of cataclastic fault core rocks was conducted by the program package "analysis auto 5.0© 1986–2006, Olympus Soft Imaging Solution GmbH". The size of particles was determined by Fmax-values (maximum Feret) which represent the maximum, normal distance between parallel tangents at opposite points on the particle margin. Automated analysis routines detected particles with  $F_{max} \geq 0.5$  millimeters. Limited by contrast and image resolution, grain size fraction  $F_{max} < 0.5$  millimeters is attributed to the matrix of analyzed cataclasites (Tab. 2-2).

Fabric analysis was conducted by the program package Win\_Tensor 4.0.3 (Delvaux, 2012). Data sets were divided with respect to synchronous fault development/fault re-

activation, fault type classification and strike direction. Paleostress analysis follows the principle of the Right Dihedron method, originally developed by Angelier and Mechler (1977). Improvements of this method (Improved Right Dihedron Method (Delvaux and Sperner, 2003)), also allow to estimate not only directions of the main stress axis  $\sigma_1$ ,  $\sigma_2$  and  $\sigma_3$  but also the stress ratio  $R$  ( $R = [\sigma_2 - \sigma_3]/[\sigma_1 - \sigma_3]$ ).

For further interpretation of structural evolution, all planes were displayed in Mohr stress circle diagrams. The concept of graphical representation of 3D stress, plotting normal stress ( $\sigma_n$ ) versus shear stress ( $\tau$ ) was introduced by Mohr (1882). Beyond displaying planes in a given stress state, the Mohr-circle concept was adapted for various applications such as strain analysis and strain refraction (e.g., Means, 1983; Nadai, 1950; Ramsay, 1967; Treagus, 1986), vorticity analysis (e.g., Passchier and Urai, 1988) or flow tensors (Lister and Williams, 1983). This method became, not only in structural geology, a useful tool to illustrate three-dimensional stress states in a two-dimensional projection which assigns values for  $\sigma_n$  and  $\tau$  for any given plane (e.g., Coelho and Passchier, 2008). By convention, in this work  $\sigma_1$  is fixed at 100 and  $\sigma_3$  at 0 (in arbitrary units). Hence, the magnitude of  $\sigma_2$  is calculated from the stress ratio  $R$  ( $\sigma_2=R \times 100$ ) and consequently maximum shear stress  $\tau$  equals 50 (Delvaux and Sperner, 2003). Plotting fault planes in suitable Mohr circle diagrams results in relative values for  $\sigma_n$  and  $\tau$  for each plane and contributes to the interpretation and understanding of fault evolution and related kinematics (Fig. 2-10g – h).

## 2.4 Geological and tectonic setting

The Northern Calcareous Alps [NCA], a fold-and-thrust belt in the northern part of the Eastern Alps, represent the Permian to Mesozoic cover sequences of the Paleozoic Austroalpine basement nappes (Greywacke Zone) and extend over more than 500 km from West to East (Fig. 2-1). Several tectonic and metamorphic events affected these units and lead to a complex internal structure (e.g., Decker et al., 1993; Frisch and Gawlick, 2003; Gasser et al., 2009; Mandl, 2000; Ortner, 2003; Ratschbacher, 1986; Tollmann, 1980, 1985).

Despite successive investigations over decades and improved stratigraphic, structural, metamorphic and geochronological data, the nappe structure and stacking order of the NCA is still a matter of controversy (Frisch and Gawlick, 2003). For general information concerning the geological and tectonic evolution of the Northern Calcareous Alps see, for example, Behrmann and Tanner (2006), Decker et al. (1993), Frisch and Gawlick (2003), Frisch et al. (1998), Linzer et al. (2002), Linzer et al. (1997), Linzer et al. (1995), Peresson

and Decker (1997), Schmid et al. (2004), Schuster et al. (2004) and Tollmann (1966, 1976, 1980, 1985).

Summarizing common concepts (e.g., Frisch and Gawlick, 2003; Linzer et al., 1997; Nemes et al., 1995; Peresson and Decker, 1997; Tollmann, 1976), the Northern Calcareous Alps underwent two major tectonic stages:

(1) Top-to-NW thrusting and nappe-stacking in a transpressional scenario from late Early Cretaceous to Lower Eocene times, induced by the northward movement of the Apulian upper plate towards Europe (Linzer et al., 1995; Nemes et al., 1995; Schmid et al., 2004). Related to the complex movement of involved (micro-) plates, a repeated change from compressional to extensional deformation affected the NCA in this tectonic stage. For instance, faulting and extension in Turonian to Coniacian times led to the formation of pull-apart basins of the Gosau group (Wagreich, 1995, 2000; Wagreich and Decker, 2001). Most prominent large-scale structures derived from N(W)-S(E) compression from late Early Cretaceous to Eocene times are (W)NW-(E)SE striking, dextral strike-slip faults as well as top (W)NW-striking thrust and reverse faults (Deformation stage D1 after Decker, 2002). Small-scale investigations reveal conjugated strike-slip fault sets, indicating NW compression (Decker et al., 1994; Decker, 2002; Linzer et al., 1995, 1997).

In Eocene times the scenario changed to an N-S compressional regime. This deformation stage (Deformation stage D2 after Decker, 2002) is demonstrated by top-to-N thrusting, S-directed backthrusts and conjugated strike-slip faults, striking NW-SE and NNE-SSW (Decker et al., 1993; Linzer et al., 1997; Linzer et al., 1995; Nemes et al., 1995; Tollmann, 1985).

(2) Post-collisional lateral extrusion and eastward displacement of the southern parts of the NCA in the Late Oligocene to Middle Miocene generated E-W to NE-SW oriented sinistral strike-slip faults (Frisch et al., 2000; Frisch and Gawlick, 2003; Frisch et al., 1998; Linzer et al., 1997; Wang and Neubauer, 1998). Additionally conjugated strike-slip fault sets and (N)NE-directed reverse faults are decisive for this deformation stage (D3 after Decker, 2002). Subsequent transtensional deformation events (D4 and D5 after Decker, 2002) are mainly characterized by re-activation of pre-existing fault planes. E-W compression in post Middle Miocene times regionally reactivated prior established fault systems (Decker and Peresson, 1996; Decker et al., 1994; Linzer et al., 1997; Peresson and Decker, 1997).

These tectonic stages, especially Paleogene and Neogene tectonic events, can be subdivided into several sub-events associated with the development of new fault planes and fault re-activation, and with variable principal stress orientations at a regional as well as a local scale. A sequence of the evolution of fault zones and the related deformation structures and stress orientation within the NCA was elaborated by e.g., Decker and



Peresson (1996), Decker et al. (1994), Linzer et al. (2002), Linzer et al. (1997), Linzer et al. (1995), Ortner (2003) and Peresson and Decker (1997).

The most distinct structural feature in the Eastern Alps is the sinistral Oligocene-Miocene Salzach-Ennstal-Mariazell-Puchberg [SEMP] fault system (e.g., Decker et al., 1993; Decker and Peresson, 1996; Frisch et al., 2000; Ratschbacher et al., 1991; Ratschbacher et al., 1989; Schmid et al., 2004; Wang and Neubauer, 1998). The fault system extends over 400 km from the Northern margin of the Tauern Window to the Vienna Basin (Fig. 2-1) and shows a maximum displacement of up to 60km (Linzer et al., 2002; Linzer et al., 1997). Late Neogene formation of the Tauern Window (Fig. 2-1) exhumed ductile structures in the Western segments of the fault system. Central and eastern parts exhibit brittle deformation over a broad segmented shear zone (Frisch et al., 2000; Frost et al., 2009; Hausegger et al., 2010; Linzer et al., 2002) that is mainly localized along the southern margin of the NCA. In addition to this major fault zone numerous sub-parallel E-W to NE-SW striking faults developed simultaneously, also within the NCA.

All investigated sites are located in the Mürzalpen nappe of the NCA. According to Frisch and Gawlick (2003) this is part of the Ultra-Tirolic Units and Imbricated Belt. This unit in the southern part of the NCA transgressively overlies the Paleozoic Greywacke Zone and is separated from the Tirolic units in the North by the SEMP fault system (e.g., Bauer, 1998; Frisch and Gawlick, 2003; Linzer et al., 2002; Mandl, 2001; Schmid et al., 2004; Tollmann, 1980).

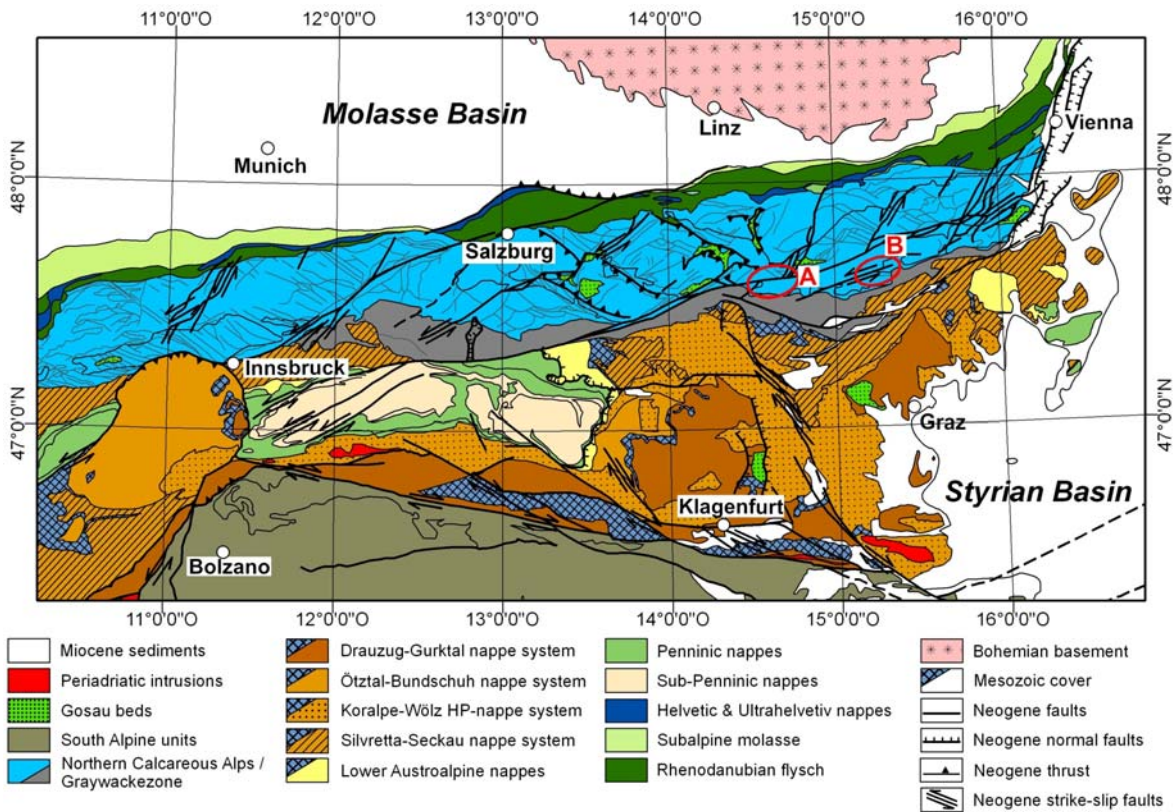


Figure 2-1: Tectonic map of the Eastern Alps with Paleogene/Neogene fault systems (modified after Linzer et al., 2002; Schmid et al., 2004). Encircled areas mark the investigated sites: (A) site Haindlkar, (B) site Brandwald and Fölz.

## 2.5 Site description and structural inventory

The investigated sites of this study are located in the Gesäuse Mountains (site Haindlkar) and on the south side of the Hochschwab massif (site Brandwald and Fölz). All sites crop out in Ladinian Wetterstein-limestone/-dolomite units of the Mürzalpen nappe which is composed of a sequence of Permo-Skythian to Norian sediments, mainly platform carbonates (Fig. 2-2).

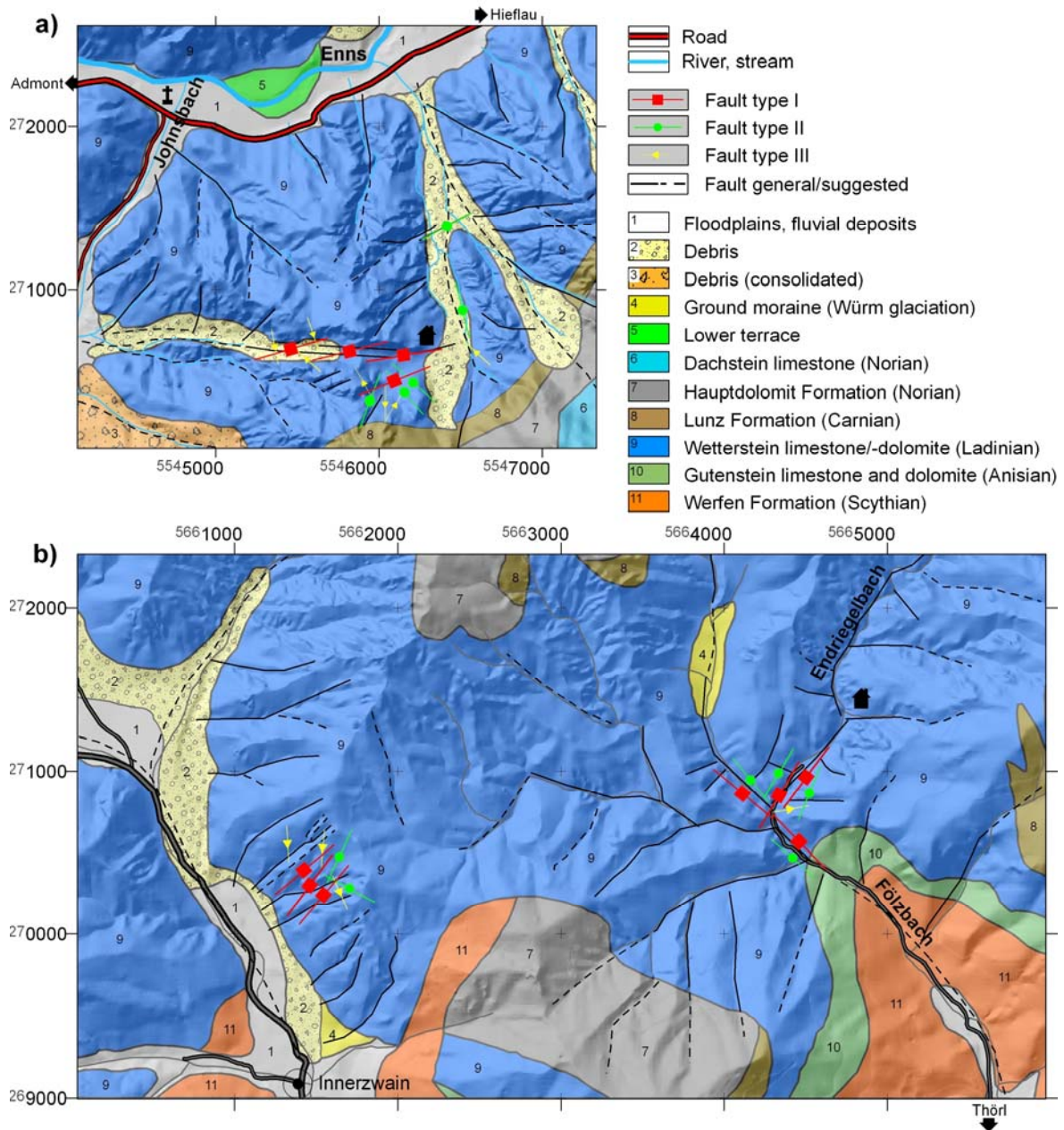


Figure 2-2: Digital Terrain Model (DTM) with overlaying geological map of (a) site Haindlkar, (b) site Brandwald (West) and site Fölz (East). Investigated faults, according to fault types and strike direction as well as supposed faults are indicated.

### 2.5.1 Site Haindlkar

Site Haindlkar, south of the river Enns, extends from the narrow Johnsbach valley in the West to the Haindlkar (cirque) in the East and is directly affected by the Ennstal/Gesäuse fault, a segment of the SEMP fault system.

The most dominant structural features on site Haindlkar (Fig. 2-2a) are E-W to ENE-WSW-striking faults (main fault direction) which extend to thicknesses of several meters to few tens of meters and cross the entire site sub-parallel to the Enns valley. These dominant faults are traceable from the so called Gsengscharte to the Haindlkar (cirque) and in a sub-parallel gorge south of the Gsengscharte (Fig. 2-2a). The fault cores are framed by moderately ( $<60^\circ$ ) to steep slickensides ( $>60^\circ$ ) with mainly flat lineation ( $20-35^\circ$ ) plunging towards E and SW. Striated steps indicate left-lateral displacement (Fig. 2-3). Most notably in the western segments, distinct internal fault planes are well developed in the broad fault cores. These internal fault planes strike sub-parallel (E-W) or in sets with various angles to the main fault trend (N-S, NW-SE, ENE-WSW) and show inclinations between  $40^\circ$  to  $60^\circ$ . Most of these planes are polished slickensides, though, some lineation, flat to moderately steep plunging to North, could be recorded.

Minor faults with steep fault planes ( $65-90^\circ$  dip angle), striking sub-parallel to the main fault trend (E-W), are found in the stream bed north of the Haindlkar towards the Enns valley. Lineation on slickensides plunges flat to the E. Kinematic indicators document left-lateral displacement.

Further fault sets predominantly strike N-S to NW-SE and WNW-ESE. Distinct lineations on slickensides are very rare but few records on NNW-SSE striking fault planes show a moderately steep inclination towards NNW. Scratching marks indicate right-lateral displacement (Fig. 2-2a).



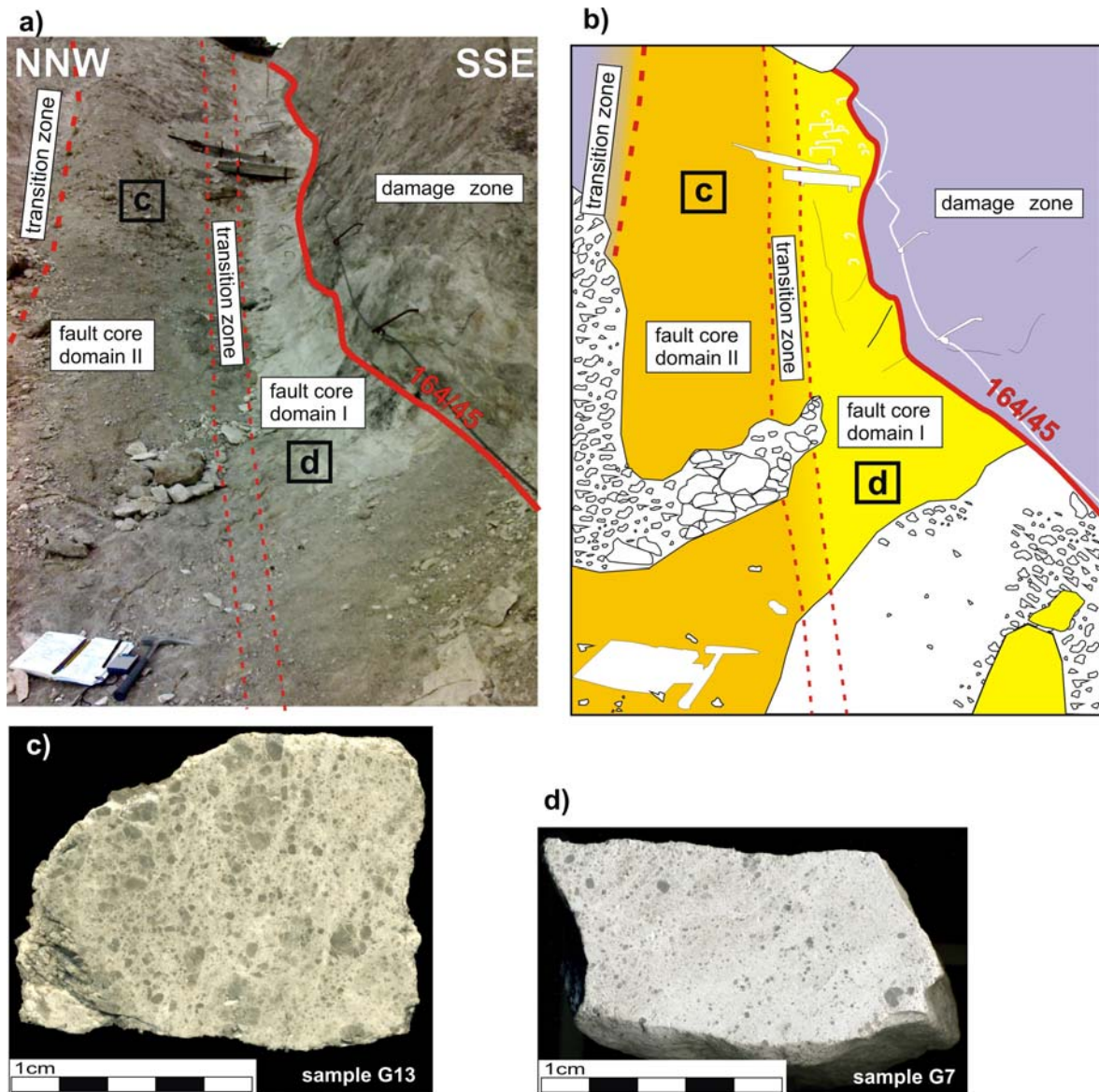


Figure 2-3: (a, b) Example of the main fault zone at site Haindlkar. The main fault plane strikes in ENE-WSW direction parallel to the SEMP- fault (165/45) and marks a distinct boundary between the damage zone and the fault core. The fault core is divided into two different domains of cataclasites (domain I & II; c, d).

(c) The cataclasites in domain II show a clast-supported fabric with fragment diameters up to 15mm (sample G13) and crosses over to the footwall damage zone.

(d) Fault core domain I consists of matrix-supported cataclasite with dolomite fragments in a fine-grained calcite matrix. Fragment diameters hardly exceed 5mm (sample G7). The thickness of this domain ranges from 50 to 250cm.

A narrow transition zone (~ 25cm) marks a continuous change in the fragment/matrix-ratio from fault core domain I to domain II. This change in the fragment/matrix-ratio and fragment size indicates a gradient of affiliated displacement and consequent grain size reduction from the fault core close to the fault plane (high displacement and advanced grain size reduction, sample G7) to less mature material (sample G13) close to the footwall damage zone.

### 2.5.2 Site Brandwald

Site Brandwald represents the western part of the investigated area on the south side of the Hochschwab massif, approximately 1km north of Innerzwain. The entire slope toe is covered by several meters of debris, deposited by numerous gorges that cut through the steep SW-facing slope (Fig. 2-2b). The main outcrop, approximately 200 m above the valley floor, takes course along the steep slope for 250 meters.

The main fault orientation on site Brandwald is clearly indicated by distinct ridges that are built up of cemented (fault core-) cataclasite. These ridges were exposed by erosion of the surrounding, closely fractured damage/transition zone (Fig. 2-4).

Main fault orientation varies from SW-NE (main fault direction) to SSW-NNE. Main fault development in SW-NE direction is manifested by steep slickensides dipping to SE, indicating left-lateral displacement along well preserved striated steps and lineations plunging approx. 40° to SW. Minor faults in sub-parallel orientation (SSW-NNE) consist of fault planes (slickensides) dipping 55-75° to ESE. Flat lineation (10-30°), plunging to SSW and NNE, with accordant fibrous and striated steps also indicates left-lateral displacement.

Another set of steeply dipping (70-85°) minor faults strike WNW-ESE. Striated steps and scratching marks exhibit right-lateral displacement with moderate steep plunge (35-60°) to E and SE, respectively.

Further minor faults appear in two sub-parallel sets. (1) Steep (65-80°) N-S striking slickensides exhibit kinematic indication for left-lateral displacement along a moderately steep, N-plunging lineation. (2) Steep (60-80°) NNW-SSE striking fault planes (slickensides) show a flat lineation plunge to the S (~20°) and indication of sinistral strike-slip movement. Additionally N-S striking, calcite filled tension fractures in en-echelon orientation to the main fault direction were recorded.



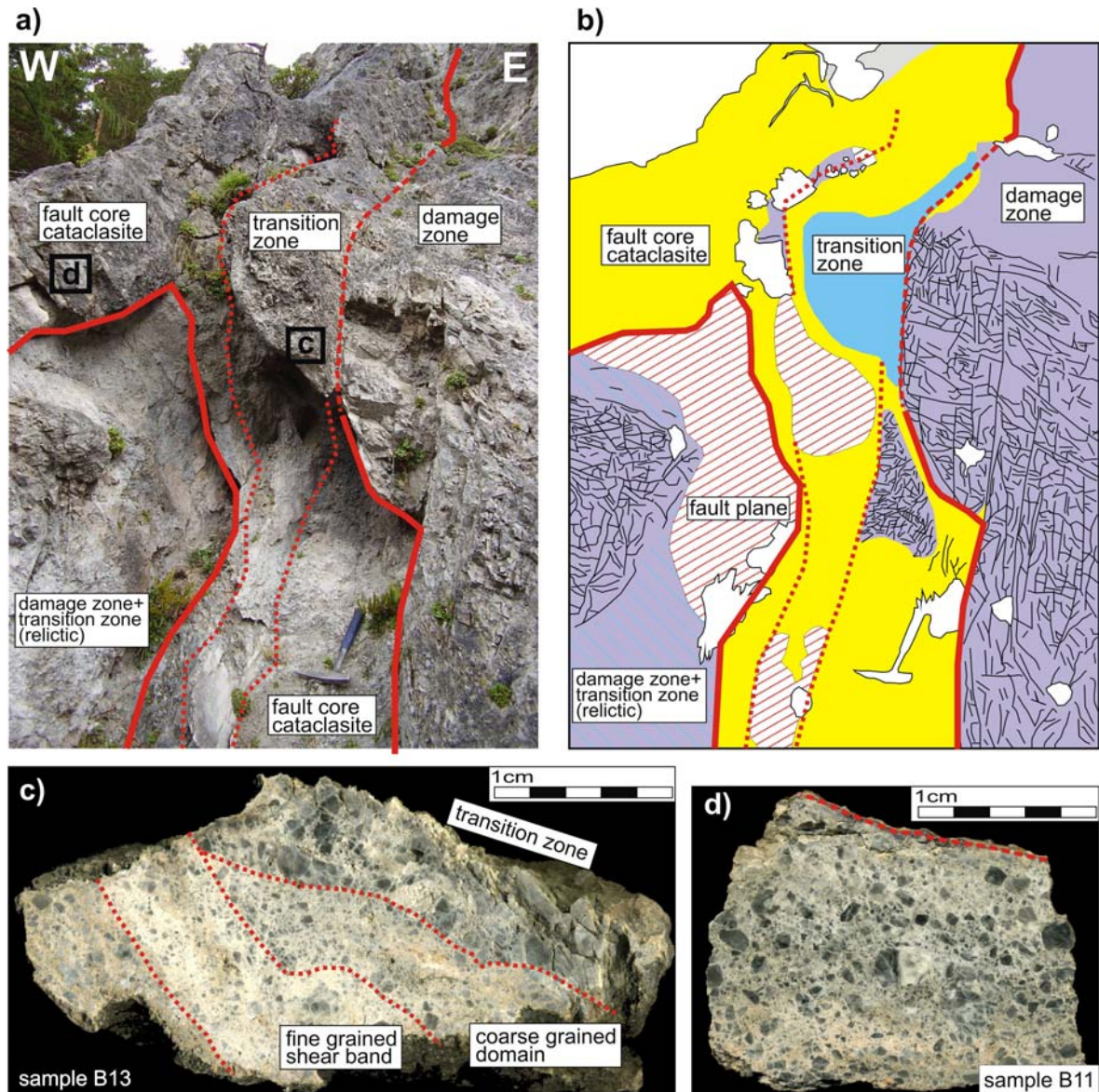


Figure 2-4: (a, b) Example of the main fault zone at site Brandwald. The main fault plane strikes in NNE-SSW direction and marks a distinct boarder between the damage zone and the fault core. The fault core developed in an irregular shape. The cataclastic fault core is characterized by various shear bands, internal slickensides and relictic damage zone lenses. The damage zone is closely fractured with a dominant discontinuity set which runs sub-parallel to the main fault strike. A small transition zone towards the footwall fault plane and extended thicknesses (up to 20cm) towards the hanging wall damage zone marks the boundary between fault core and damage zone. Weathering of the closely fractured damage zone turns out ridges of fault core cataclasites with thicknesses and heights up to 1m. (c) Cataclasites near the hanging wall transition zone show various domains of grain size distribution and fragment/matrix ratios. Fine grained shear bands exhibit matrix-supported fabrics and strike sub-parallel to the main fault direction. (d) Cataclasites in close range to the foot wall fault plane generally show coarser grained fabrics. Spacing of internal slickensides increases towards the foot wall border. This internal fault core architecture indicates increasing displacement and consequent grain size reduction from the foot wall towards the hanging wall.

### 2.5.3 Site Fölz

Site Fölz is the easternmost part of this study. The main working area is situated around the confluence of the Fölz- und Endriegel stream and surrounded by mainly steep slopes. In most instances outcropping main faults follow the stream beds, striking NE-SW and NW-SE (Fig. 2-2b).

In contrast to the sites described above, at site Fölz a different geometrical arrangement of structures was obtained. Outcrops, as well as the main fault orientations follow the stream beds of the rivers Endriegel (NNE-SSW) and Fölz (NW-SE) and give distinct indication of a well-developed, conjugated main fault system (Fig. 2-2b).

The Fölz stream and affiliated steep main and sub-parallel minor faults strike NW SE (mean orientation 230/75). Striated steps and calcite fibers on fault-bordering slickensides indicate right-lateral displacement with moderate dip of 30 to 40° to (W)NW. The conjugated counterpart of the main fault system is formed by steep fault planes (70-85° dip angle) striking NNE-SSW to NE-SW. Sinistral displacement is indicated by calcite fibers and linear steps. Lineation plunge varies from SW/SSW (15-20°) and S/SW (~60°). Internal fault planes of major and minor faults predominantly strike sub-parallel to the main fault directions and transect the well developed, broad fault cores (Fig. 2-5).

Further minor fault sets appear as distinct set of steep cataclasite layers (dip ~ 80°), striking approximately E-W and showing evidence of sinistral displacement (calcite fibers) along flat lineations (5 -30°) plunging towards E and W.



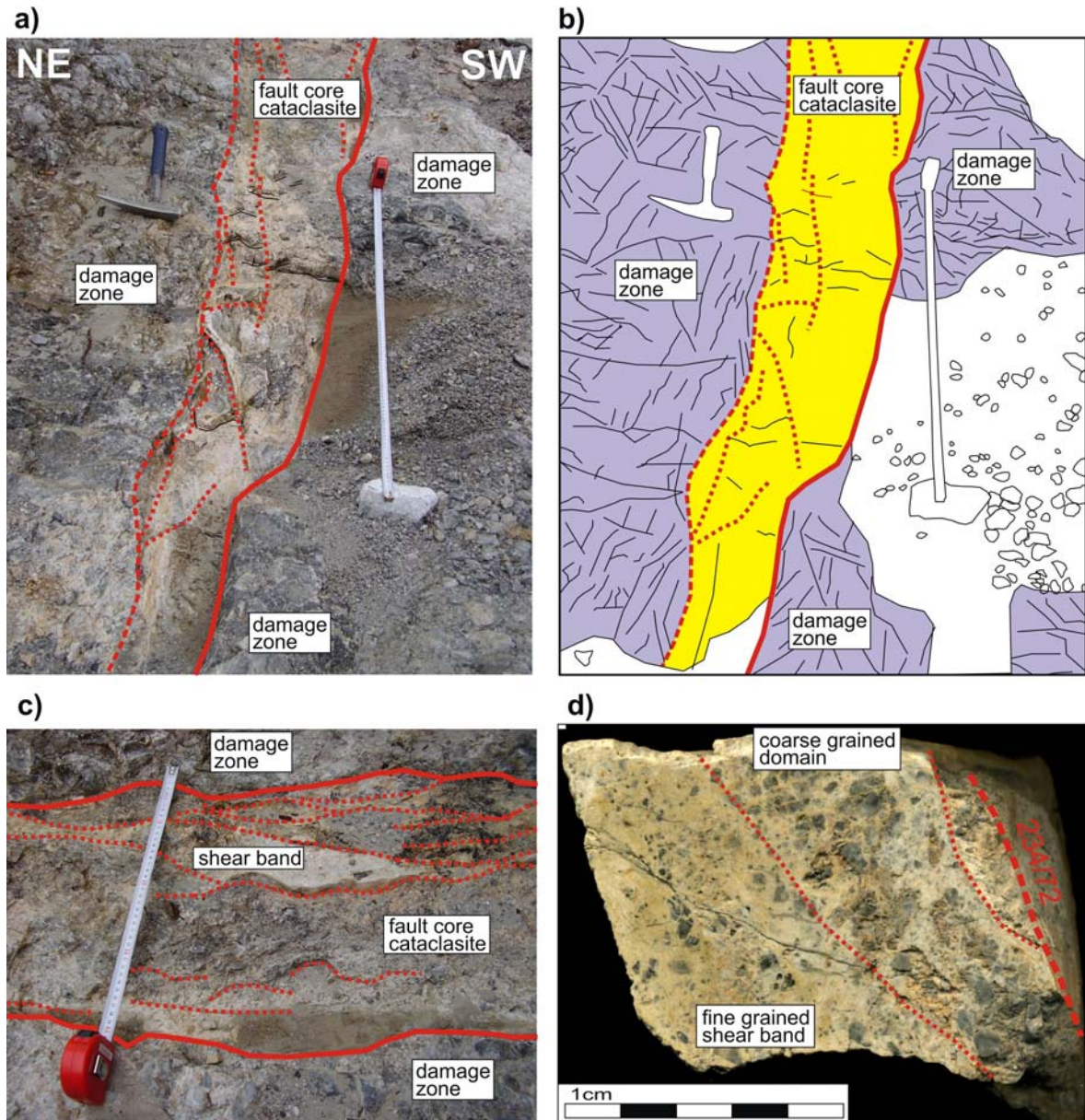


Figure 2-5: (a, b) Example of a type II fault at site Fölz. Fault direction strikes NW-SE, sub-parallel to the Fölz stream (218/72). Fault core thickness varies from 20 to 50cm. The damage zone shows fractures with close to intermediate spacing. Secondary calcite cementation is dominant in this part of site Fölz. (c) Detail of the internal fault core structure. Slickensides, sub-parallel to the main fault direction, border internal shear bands and divide the fault core in various domains of grain size distribution and fragment/matrix ratio. (d) Fault core cataclasite sample with fine- and coarser grained domains, bordered by internal slickensides, striking sub-parallel to the main fault direction.

## 2.6 Results

Brittle behavior of the dolomite host rock during multiple tectonic faulting events (see Linzer et al., 1997) led to a widespread fragmented and variable rock mass. Hence, a discrete distinction between “intact” host rock and damage zones can not be determined. Field data acquisition with emphasis on cataclastic fault core development and adjacent domains reveals generally non-uniform fragmented damage zones.

Particularly major faults show considerable variations in spacing and orientation of discontinuities between hanging and foot wall damage zones. Therefore cross sections of major faults reveal asymmetric damage zones. Fractures are preferably arranged in various sets with irregular orientation pattern. However, major discontinuity sets, striking mainly sub-parallel to the main fault direction, were preferably recorded in connection to conspicuously developed transition zones. Closely spaced (mm to view cm) sub-sets in irregular orientations in between these main fracture sets are responsible for an advanced segmentation of the rock mass.

### 2.6.1 Fault type classification

Structural field data acquisition, fault zone- and particle analysis of fault core rocks result in a classification of three different fault types (Fig. 2-6d-f, 2-7, 2-8, 2-9; Tab. 2-1). Fault core cataclasites are composed of comminuted dolomite fragments (or particles) embedded in a fine grained matrix of pulverized dolomite and secondary calcite.



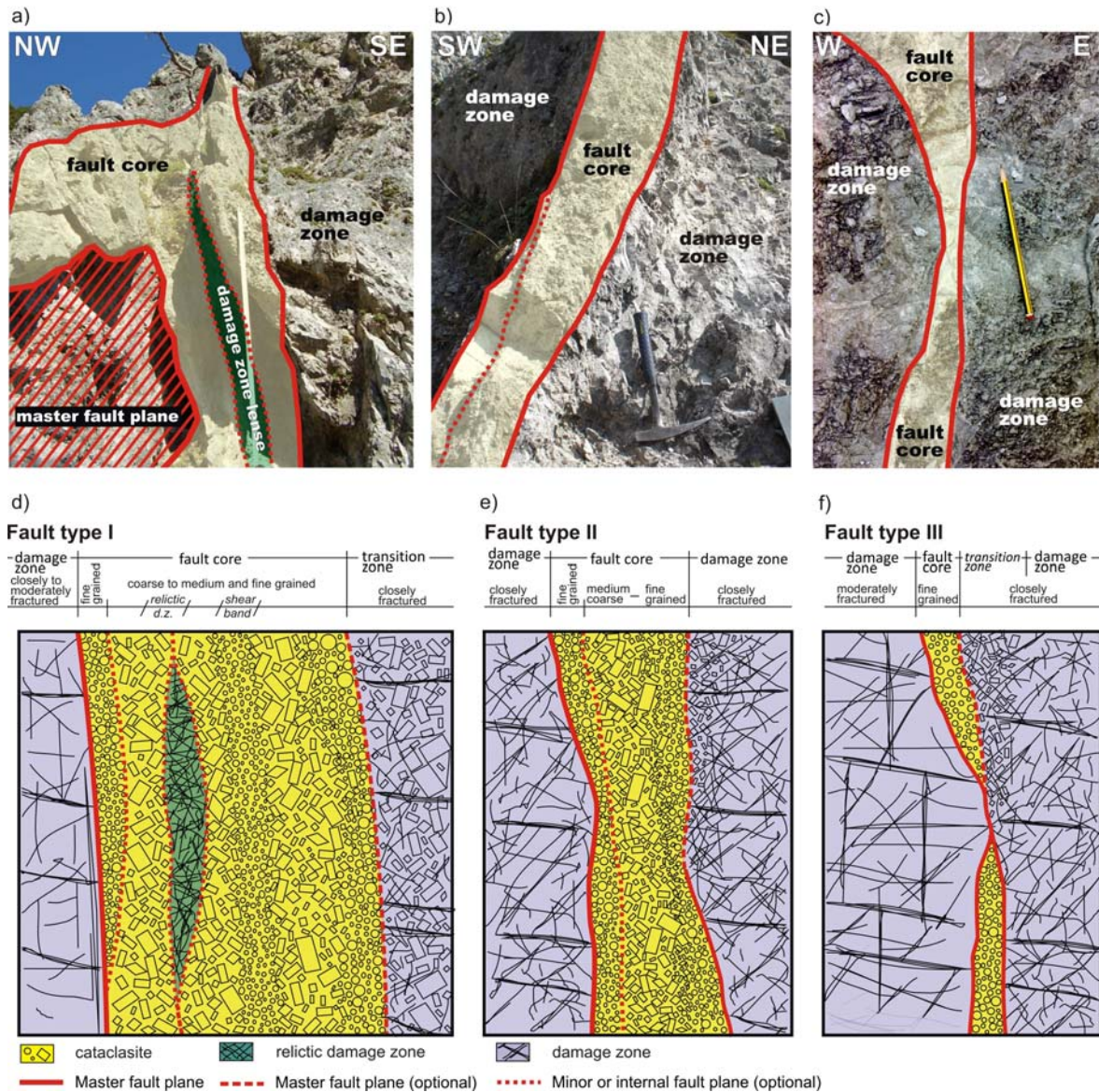


Figure 2-6: (a-c) Examples of fault types and (d-f) derived fault type classification. (a) Site Brandwald, sinistral NE-SW-striking major fault with a total thickness of up to 120 cm. (b) NW-SE striking fault core at site Brandwald; thickness up to 30 cm. (c) Solitary cataclastic layer showing a range in thickness from a few mm up to 10 cm, from site Haindlkar. (d-f) Conceptual cross sections of (d) Fault type I, (e) Fault type II and (f) Fault type III.

All fault cores are composed of comminuted fragments in a very fine-grained matrix of pulverized host rock and secondary calcite.

**Fault type I** is characterized by the most complex fault core structure in the working area. This fault type is strictly connected to the main fault strike direction on each site. Fault core thickness reaches widths of several 10's of meters. Bordered by a continuous master fault plane, developed as slickenside with striated (linear to lunate) steps as kinematic indicators, the fault core may contain several domains of variable composed cataclasites and relictic lenses of not fully disintegrated damage zone matter. These

domains can be bordered either by internal fault planes (mainly polished slickensides, sub-parallel to the master fault plane) or show a gradual transition to adjacent domains. Besides the master fault plane, a very variable transition zone between fault core and damage zone is common for this fault type. Internal fault planes usually strike sub-parallel to the master fault (Fig. 2-6a, d).

**Fault type II** is classified by an advanced internal segmentation of the fault core and thickness up to 100 cm. Embedded in a closely to moderately fractured damage zone, the fault core is always bordered by a master fault plane (continuous slickenside) and either another fault plane or merging into a transition zone towards the damage zone. Bulk proportion of matrix in the fault core varies between 70 and 85% with a maximum fragment diameter of approximately 8 mm. The internal structure of the fault core is not uniform but characterized by one to several, fine grained shear bands. These shear bands can be bordered by internal fault planes or pass into coarser grained domains in a smooth transition (Fig. 2-6b, e).

**Fault type III** develops as solitary cataclastic layer. Fault core thickness varies in lateral extension from a few mm up to 20 cm. The fault core is bordered by mainly polished, continuous fault planes and surrounded by a moderately to closely fractured damage zone. However, an approximately 20 cm thick transition zone can be noticed infrequently in very closely fractured damage zones (Fig. 2-6c, f). The uniform fault core is composed of fine grained (micritic) matrix (proportion of area up to 90%) and fragments/components with a maximum diameter ( $F_{\max}$ ) less than 5 mm (Tab. 1).

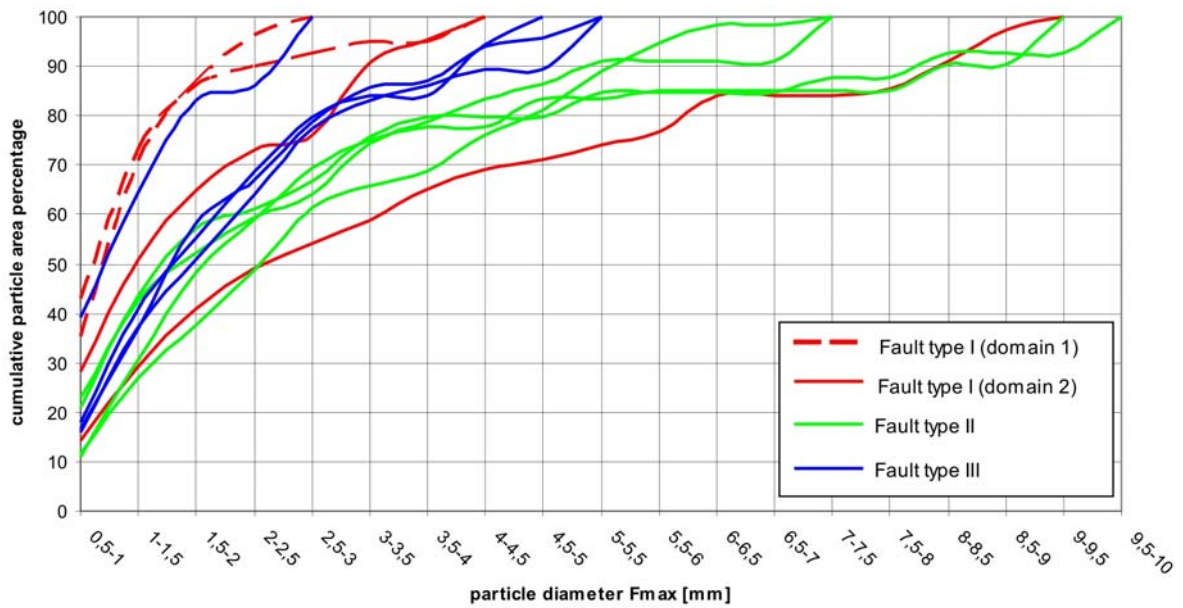


Figure 2-7: Fragment size (maximum particle diameter  $F_{max}$ ) distribution diagram (fragment size vs. bulk percentage of grains smaller than a given size) of fault core rocks from site Haindlkar. (1) Type I samples plot in distribution curves with variable gradient and variable maximum particle sizes. This variability underlines the classified structural inventory of type I faults: complex internal fault core structure with different domains of cataclasites. Domain I cataclasites plot in steep curves with maximum particle size of 4mm. Domain II shows significant higher particle sizes (up to 9,5mm) and lower gradients of the distribution curve. (2) Tape II and type III faults plot in the field of fault type I, domain II. Type II faults exhibit maximum particle sizes from 7 up to 10mm. Type III faults plot in slightly steeper curves with maximum particle sizes below 5mm.

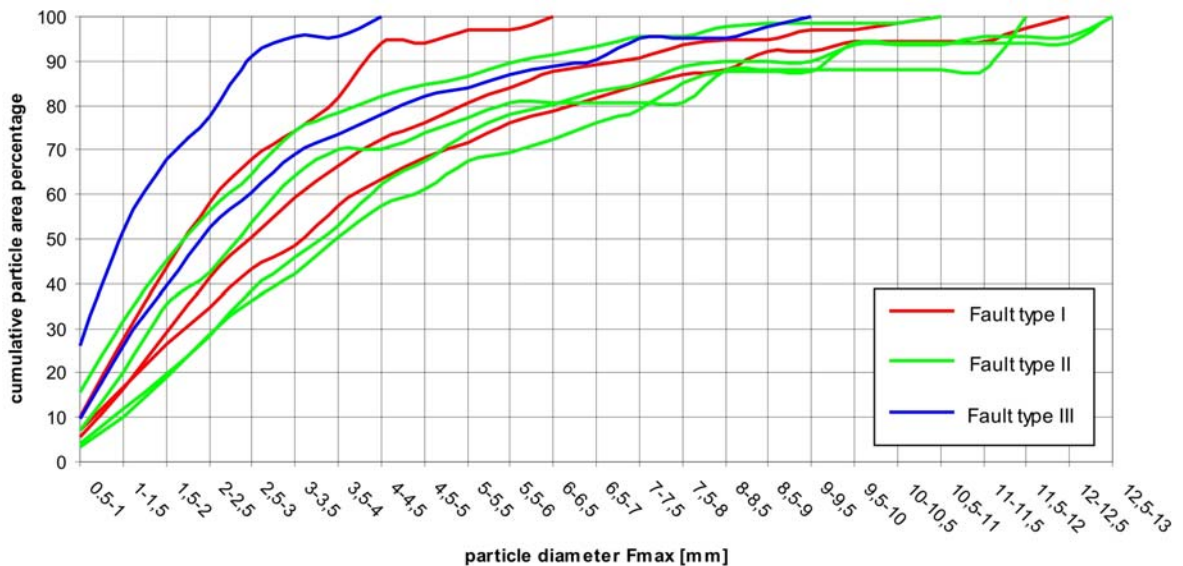


Figure 2-8: Fragment size (maximum particle diameter  $F_{max}$ ) distribution diagram (fragment size vs. bulk percentage of grains smaller than a given size) of fault core rocks from site Brandwald. Sub-parallel faults (type I and II) show similar distributions with maximum particle diameters up to 12 and 13mm, respectively. Internal segmentation and different cataclasite domains in type I faults exhibit steeper distribution curves and maximum particle sizes of 6 mm. Type III cataclasites plot in



parallel curves with respect to type I faults but show smaller maximum grain sizes of 4,5 and 9,5 mm, respectively.

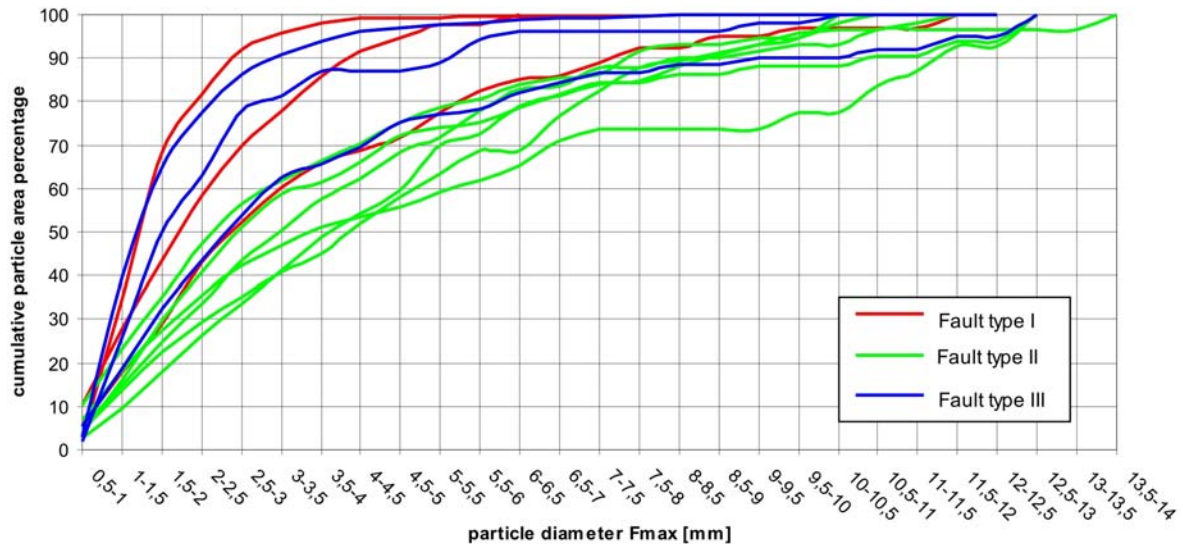


Figure 2-9: Fragment size (maximum particle diameter  $F_{max}$ ) distribution diagram (fragment size vs. bulk percentage of grains smaller than a given size) of fault core rocks from site Fölz. Particle distribution curves cluster in to domains. (1) Steep curves with mainly small grain sizes (90% < 4,5mm), represented by a fault type I domain sample and fault type III cataclasites, and (2) rather flat curves of type II samples with maximum particle sizes up to 14 mm. However, also type I and III samples show domains in similar distribution and plot parallel to type II samples.

## 2.6.2 Fabric and paleostress analysis

Fabric and paleostress analyses were conducted by evaluation of structural data under the assumption of synchronous fault development or synchronous fault re-activation, respectively. Selected data sets are presumed to be affected by coherent tectonic faulting and therefore coherent paleostress conditions.

Paleostress analyses indicate an orientation of principal stresses characteristic for a strike-slip regime with a transpressional (site Haindlkar and Brandwald) and transtensional (site Fölz) component. The maximum plunge of the  $\sigma_1$ -axis is  $21^\circ$ , the orientation of the  $\sigma_2$ -axis is sub-vertical, the  $\sigma_3$ -axis sub-horizontal.

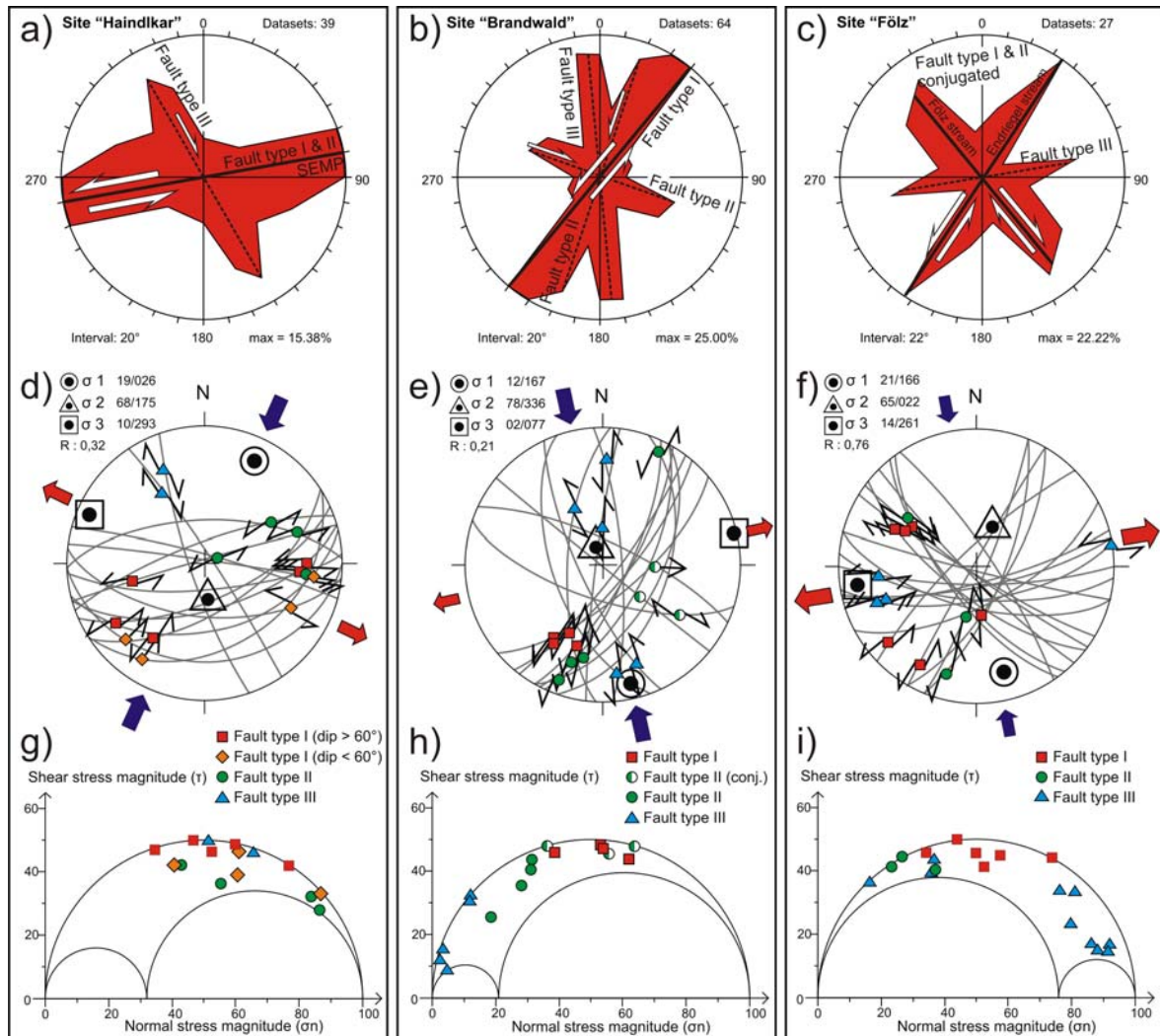


Figure 2-10: (a-c) Orientation data, strike of classified faults and related structures. (d-f) Paleostress analysis carried out by Improved Right Dihedral method (Delvaux and Sperner, 2003). Fault types are illustrated in black squares (Fault type I), grey circles (Fault type II) and white triangles (Fault type III). (d) Fault type I at site Haindlkar is sub-divided into two domains. Black squares indicate steep fault planes with dip angles over 60°. White rhombuses mark fault planes with dip angles less than 60°. (h) Conjugated type II faults at site Brandwald are indicated by black/white circles. (g-i) Equivalent Mohr diagrams of classified faults.

### 2.6.2.1 Site Haindlkar

The transpressional stress regime is characterized by subhorizontal  $\sigma_1$ - (026/19) and  $\sigma_3$ -axis (296/10) with an estimated stress ratio  $R=0.32$ . Type I faults had been subdivided into two categories:

- (1) Type Ia comprises steeply dipping major fault planes with dip angles exceeding 60° (red squares in Fig. 2-10d).

(2) Type Ib contains major fault planes with dip angles less than  $60^\circ$  (orange rhombuses in Fig. 2-10d).

Both fault types show sinistral displacement, sub-parallel to the Enns valley, and indicate the main fault direction of this site.

Type Ia faults plot in a cluster of maximum shear stress ( $\tau_{max}$ ) in the Mohr-circle diagram ( $\sigma_n / \tau \sim 1$ ). Due to the lower dip angle of Type Ib, a slight shift towards lower shear stresses ( $\tau$ ) and higher normal stresses ( $\sigma_n$ ) is observed ( $\sigma_n / \tau > 1$ ) (Fig. 2-10g).

Type II faults, striking sub-parallel to the main fault direction with an average deviation of  $15^\circ$  (dip  $\sim 80^\circ$  to the N), denote further decreasing shear stress but appear to be more variable in normal stress values ( $\sigma_n$ ) than Type I faults ( $0 \leq \sigma_n / \tau \leq 1$ ) (Fig. 7g). Type II faults are interpreted as precursor of Type I faults with no adequate fault core development.

Most Type III fault planes appear polished without distinct lineation, and depending on orientation, assign variable stress ratios ( $\sigma_n / \tau$ ). Recorded Type III faults strike NNW-SSE and show antithetic (dextral) displacement with respect to the main (left-lateral) fault movement. These structures plot in a cluster of maximum shear stress ( $\tau_{max}$ ) and may represent a minor developed Anti-Riedel fault set (Fig. 2-10g).

#### 2.6.2.2 Site Brandwald

Paleostress analysis on this site indicates a transpressional stress regime with flat  $\sigma_1$ - (167/12) and  $\sigma_3$ -axis (077/02) and a stress ratio R of 0.21 (Fig. 2-10e).

Steep Type I faults, tracing parallel to the main fault direction, exclusively develop in orientation of the maximum shear stress ( $\sigma_n / \tau \sim 1$ ) and strike NE-SW (red squares in Fig. 7e, h).

Type II faults developed in two orientations:

- (1) Sub-parallel to the main fault orientation with a deviation of approximately  $15^\circ$  (green circles in Fig. 2-10e, h), indicating lower normal stress ( $\sigma_n$ ) and
- (2) Sub-perpendicular ( $\sim 80^\circ$ ) to the main fault direction (green/white circles in Fig. 7e, h), representing the conjugated counterpart of the main fault direction, imposing maximum shear stress ( $\sigma_n / \tau \sim 1$ ).

Fault Type III structures strike predominantly N-S and developed in synthetic Riedel configuration to the main fault course and therefore in an orientation of low normal stress (blue triangles in Fig. 2-10e, h).

#### 2.6.2.3 Site Föls

This site exposes a distinct conjugated main fault system in a transtensional regime. The main stress axes  $\sigma_1$  (166/21) and  $\sigma_3$  (261/14) assign flat dip to S and E, respectively. The stress ratio R was defined with 0.76 (Fig 2-10f).



Type I faults exclusively developed as a conjugated fault system. This configuration of main faults leads to a distinct cluster of maximum shear stress in the Mohr stress circle diagram (red squares in Fig. 2-10i) ( $\sigma_n / \tau \sim 1$ ).

Type II faults were recorded sub-parallel to main fault direction (deviation  $\sim 15^\circ$ ), tendentially showing lower normal stress values in comparison with Fault type I faults ( $\sigma_n / \tau \leq 1$ ) (green circles in Fig. 2-10 f, i).

Fault type III structures appear in variable orientations.

(1) Sub-parallel to the conjugated main fault directions (deviation  $\sim 15^\circ$ ). These type III faults plot in a similar cluster like Type II faults (blue triangles in Fig. 2-10f, i).

(2) The main Fault Type III set strikes almost perpendicular (E-W) to the main stress axis  $\sigma_1$  and, therefore, shows high normal stress values (blue triangles in Fig. 2-10f, i).

## 2.7 Discussion

With respect to fault core architecture (thickness and structural inventory) and characteristics of fault core rocks ( $F_{max}$ , matrix area), the studied faults and fault zones can be classified into three types (Fault type I, II and III). Fabric and paleostress analyses clearly indicate the exclusive development of Type I and Type II faults in direction of maximum shear stress, and in an orientation parallel to the main fault strike. This therefore indicates, that although the protolith carbonates show a pre-existing anisotropy (sedimentary bedding), the main fault develop in an orientation parallel to the maximum shear stress. . Distinct indication of a conjugated main fault system was only recorded at site Fölz. Antithetic fault development of minor fault types (II and III) in a possible Anti-Riedel configuration was, however, recorded at sites Haindlkar and Brandwald.

Beside the strike direction of main faults, Type II and III faults generally developed in various orientations. Type II and III faults in high or maximum shear stress orientation did, however, not develop completely to type I or type II faults.

Type II and type III faults, striking sub-parallel to the main fault directions, show an average deviation of  $15^\circ$ - $25^\circ$  in strike direction and therefore do not obtain required (maximum) shear stress to develop to type I or type II faults. Furthermore, affected by pre-existing and predominant structures, and in spite of high or maximum shear stress orientation, no complete development of a conjugated main fault system (antithetic Riedel shear orientation) occurred at site Haindlkar and Brandwald.

Type III faults also occur in other orientations with low normal stress (synthetic orientation sub-parallel to  $\sigma_1$ ) or sub-perpendicular to  $\sigma_1$  with high normal stress in antithetic Riedel orientation (X-planes).

These observations basically show that Type I faults defined in this study generally evolve in a strike direction of maximum shear stresses ( $\tau$ ). Referring to analogue experiments (e.g., Chambon et al., 2006; Coelho et al., 2006; Del Ventisette et al., 2006; Dooley and Schreurs, 2012; Misra et al., 2009; Renner and Rummel, 1996; Richard and Krantz, 1991; Schellart, 2000), Mohr-Coulomb fracture mechanics as well as numerical models (Anderson, 1951; Caine and Foster, 1999; Healy et al., 2006; Magri et al., 2005; Renner and Rummel, 1996; Sheldon et al., 2006; Zhang et al., 2007), this is not surprising, but was rarely described so far from natural examples at a scale of major fault zones with a width exceeding tens of meters. We assume that the main fault zones developed continuously from Type III towards Type II and Type I as cataclastic shear zones. The development of the fault type is therefore significant for the amount of displacement indicating that, for this study area, the width of the fault core increased with continuous displacement and that the fragment size within the fault core decreased simultaneously. As shear localized along one distinct shear zone, previous sets of sub-parallel shears were aborted and remained in their stage of fault zone evolution (either as Type III or Type II).

Faults with other strike directions did not develop in an orientation related to the maximum shear stress direction, but evolved as secondary faults to the main fault zone, in an orientation according to R or R' (or X) shear fractures. Shear was only moderately localized and mainly accommodated displacement along the main fault zone. Due to the minor displacement, these faults developed as Type III faults zones, and in some cases towards Type II cataclastic shear zones.

The total displacement along the major SEMP fault system is estimated up to 60 km of left lateral displacement in Oligo-Miocene time (e.g., Linzer et al., 2002; Linzer et al., 1997). Investigated, sub-parallel and transverse oriented secondary faults (Type II and Type III) hardly show distinct indication to estimate absolute displacement in the field. Summarizing field observations and studies in similar environments (e.g., Bastesen et al., 2010; Billi, 2005b; Kim and Sanderson, 2005; Micarelli et al., 2006; Twiss and Marrett, 2010a, b), the range of displacement for each fault type is variable. Depending on pre-existing and predominant structures and orientation (stress state), estimated displacement increases from decimeters to few meters (fault type III), to several tenth of meters (fault type II) up to several hundred meters (fault type I).

In general, fault zone evolution within the study area indicates that the width of fault cores and the matrix / fragment areal surface ratio seem to be reciprocally related to the ratio ( $\sigma_n / \tau$ ). As this ratio can also be interpreted as an indirect approach of displacement assessment, the evolution of the fault zones in the study area shows that the width of the cataclastic fault cores increase with decreasing ( $\sigma_n / \tau$ ) ratio, and therefore presumably with increasing displacement. Type II and Type III fault zones are therefore characterized by low and high ( $\sigma_n / \tau$ ) ratios, respectively. Accordingly, grain size was reduced continuously and matrix / fragment areal surface ratio increased in Type I faults.

<b>Fault type</b>	<b>Fault core thickness</b>	<b>Fault core properties</b>	<b>F<sub>max</sub> [mm]</b>	<b>Matrix area [%]</b>
Fault type I	1 m – several 10's m	complex fault core structure; suitable thickness and orientation; several cataclasite domains; internal (minor) fault planes	< 7 (site Haindlkar)	~ 80 - 90 (site Haindlkar)
			<13 (site Brandwald, Fölz)	55 – 80 (site Brandwald, Fölz)
Fault type II	20 – 100 cm	internal segmentation; shear bands; internal (minor) fault planes	< 10 (site Haindlkar)	~ 80 (site Haindlkar)
			<16 (site Brandwald, Fölz)	50 – 85 (site Brandwald, Fölz)
Fault type III	0 – 20 cm	Uniform and solitary cataclasite layer	< 6 (site Haindlkar)	~ 70 - 90 (site Haindlkar)
			<10 (site Brandwald, Fölz)	60 – 80 (site Brandwald, Fölz)

Table 2-1: Compilation of relevant fault core specifications. Fault core thickness as visible in the field. Matrix area includes particles with  $F_{max} < 0.5\text{mm}$  and indicates bulk fault core composition for fault types I and II. For advanced data of particle analysis see Table 2-2.

## 2.8 Conclusions

The methodical approach of this study combines an elaborated brittle fault type classification scheme with related paleostress analysis of coherent (re-) activated shear zones in carbonate rocks. Compared to other investigations, this work provides evidence for fault zone evolution from field observations, comparable to theoretical and analogue models of Mohr-Coulomb fracture evolution. From the evolution of cataclastic fault zones described in this study, the following general conclusions can be deduced:

- Wide cataclastic shear zones (with cataclastic fault cores) mainly develop in the direction of planes of maximum shear stress ( $t_{\max}$ ).
- The thicknesses of fault cores, between these planes of maximum shear stress concentration, reflect the main amount of displacement along the shear zone.
- The evolution of cataclastic fault cores is depending on orientation with respect to principal stress axis as well as pre-existing and predominant structures.
- Progressive fault development from Fault type III to Fault type II and Fault type I appears to be limited to orientations with high or maximum shear stress ( $\tau$ ).
- These field observations are a natural example of fault zone development according to Mohr-Coulomb fracture evolution described from Riedel type experimental configurations.

## 2.9 Appendix

Site Haindlkar								
sample site	fault type	sample area	particle area (F <sub>max</sub> > 0,5)	particle area	matrix area	matrix	part./matrix ratio	(F <sub>max</sub> ) max
		[mm <sup>2</sup> ]	[mm <sup>2</sup> ]	%	[mm <sup>2</sup> ]	%		[mm]
G12	I	2666,81	209,45	7,85	2457,36	92,15	0,09	2,87
G7	I	2672,07	242,11	9,06	2429,95	90,94	0,10	4,47
G13	I	3845,37	758,43	19,72	3086,94	78,05	0,25	6,21
G8	I	740,04	154,88	20,93	585,16	79,07	0,26	4,53
H6	II	1636,90	247,97	15,15	1388,93	84,85	0,18	7,43
H7	II	2851,90	528,82	18,54	2323,08	81,46	0,23	9,91
H9	II	1684,67	369,51	21,93	1315,16	78,07	0,28	9,17
JN3M	II	2930,69	549,27	18,74	2381,42	81,26	0,23	7,29
H10	III	683,32	189,11	27,67	494,21	72,33	0,38	5,22
H8	III	1136,89	113,53	9,99	1023,36	90,01	0,11	2,91
JN3O	III	2459,00	439,29	17,86	2019,71	82,14	0,22	5,12
JN3U	III	2260,17	172,44	7,63	2087,73	92,37	0,08	4,51

Site Brandwald								
sample site	fault type	sample area	particle area (F <sub>max</sub> > 0,5)	particle area	matrix area	matrix	part./matrix ratio	(F <sub>max</sub> ) max
		[mm <sup>2</sup> ]	[mm <sup>2</sup> ]	%	[mm <sup>2</sup> ]	%		[mm]
B10	I	2377,68	559,94	23,55	1817,74	76,45	0,31	6,38
B11	I	6765,05	2787,20	41,20	3977,85	58,80	0,70	12,37
B13	I	8816,06	2960,43	33,58	5855,63	66,42	0,51	10,56
B2	II	3914,42	578,16	14,77	3336,26	85,23	0,17	11,87
B6	II	4347,13	1301,96	29,95	3045,16	70,05	0,43	10,49
B14	II	7641,06	2787,46	36,48	4853,60	63,52	0,57	12,98
B19	II	7431,00	2371,75	31,92	5059,25	68,08	0,47	12,98
B1	III	8214,73	1594,45	19,41	6620,28	80,59	0,24	9,05
B8	III	1340,86	499,76	37,27	841,10	62,73	0,59	4,25

Site Fölz								
sample site	fault type	sample area	particle area (F <sub>max</sub> > 0,5)	particle area	matrix area	matrix	part./matrix ratio	(F <sub>max</sub> ) max
		[mm <sup>2</sup> ]	[mm <sup>2</sup> ]	%	[mm <sup>2</sup> ]	%		[mm]
FS1	I	3676,60	747,67	20,34	2928,93	79,66	0,26	6,35
FSR140	I	1812,45	399,04	22,02	1413,42	77,98	0,28	7,98
FS4R17	I	4271,29	1865,62	43,68	2405,67	56,32	0,78	12,98
FS4R3	II	7761,31	3285,49	42,33	4475,82	57,67	0,73	11,72
FS4R10	II	7794,98	2846,27	36,51	4948,71	63,49	0,58	10,94
FS4R13	II	6243,17	2870,58	45,98	3372,59	54,02	0,85	13,67
FS4R14	II	6288,76	2370,02	37,69	3918,74	62,31	0,60	15,52
FS4R15	II	2960,29	1256,58	42,45	1703,71	57,55	0,74	16,50
FS4R17	II	3199,07	1572,57	49,16	1626,50	50,84	0,97	12,98
FS4R144	III	5414,39	1432,87	26,46	3981,52	73,54	0,36	11,99
FS4R145	III	2924,11	860,49	29,43	2063,62	70,57	0,42	11,99
FS4R146	III	612,04	183,55	29,99	428,49	70,01	0,43	9,51
FS4R18	III	1057,23	330,91	31,30	726,33	68,70	0,46	6,48

Table 2-2: Particle analysis data, categorized by site and fault type. Matrix comprises particles with F<sub>max</sub> less than 0.5mm.

## 2.10 References

- Agosta, F., Aydin, A., 2006. Architecture and deformation mechanism of a basin-bounding normal fault in Mesozoic platform carbonates, central Italy. *Journal of Structural Geology* 28, 1445-1467.
- Ahlgren, S.G., 2001. The nucleation and evolution of Riedel shear zones as deformation bands in porous sandstone. *Journal of Structural Geology* 23, Issue 8, 1203–1214.
- Anderson, E.M., 1951. *The Dynamics of Faulting*. Oliver and Boyd, Edinburgh.
- Angelier, J., Mechler, P., 1977. Sur une methode graphique de recherche des contraintes principales egalement utilisable en tectonique et en seismologie : la methode des diedres droits. *Bulletin de la Societe Geologique de France* 7, 1309-1318.
- Antonellini, M., Aydin, A., Pollard, D.D., 1994. Microstructure of deformation bands in porous sandstones at Arches National Park, Utah. *Journal of Structural Geology* 16, Issue 7, 941-959.
- Aydin, A., Berryman, J.G., 2010. Analysis of the growth of strike-slip faults using effective medium theory. *Journal of Structural Geology* 32, 1629–1642.
- Bastesen, E., Braathen, A., Nottveit, H., Gabrielsen, R.H., Skar, T., 2010. Extensional fault cores in micritic carbonate – Case studies from the Gulf of Corinth, Greece. *Journal of Structural Geology* 32, Issue 11, 1609-1628.
- Bauer, F.K., 1998. Zur Frage der Mürzalpendecke im Gebiet der Gesäuseberge und eine Diskussion über die Stellung der Nördlichen Kalkalpen. *Jahrbuch der Geologischen Bundesanstalt* 141, S. 5 - 19.
- Behrmann, J.H., Tanner, D.C., 2006. Structural synthesis of the Northern Calcareous Alps, TRANSALP segment. *Tectonophysics* 414, 225–240.
- Billi, A., 2005b. Grain size distribution and thickness of breccia and gouge zones from thin (<1 m) strike-slip fault cores in limestone. *Journal of Structural Geology* 27, 1823–1837.
- Billi, A., Salvini, F., Storti, F., 2003. The damage zone-fault core transition in carbonate rocks: implications for fault growth, structure and permeability. *Journal of Structural Geology* 25, 1779–1794.
- Billi, A., Storti, F., 2004. Fractal distribution of particle size in carbonate cataclastic rocks from the core of a regional strike-slip fault zone. *Tectonophysics* 384, 115–128.

- Bonson, C.G., Childs, C., Walsh, J.J., Schöpfer, M.P.J., Carboni, V., 2007. Geometric and kinematic controls and the internal structure of a large normal fault in massive limestone: The Maghlaq Fault, Malta. *Journal of Structural Geology* 29, 336-354.
- Caine, J.S., Evans, J.P., Forster, C.B., 1996. Fault zone architecture and permeability structure. *Geology* 24, 1025 - 1028.
- Caine, J.S., Forster, C.B., Evans, J.P., 1993. A classification scheme for permeability structures in fault zones. *Eos (Transactions, American Geophysical Union)* 74.
- Caine, J.S., Foster, C.B., 1999. Fault zone architecture and fluid flow: insights from field data and numerical modelling. in: Haneberg, W.C., Mozley, P.S., Moore, J.C., Goodwin, L.B. (Eds.) - *Faults and Subsurface Fluid Flow in the Shallow Crust. Geophysical Monograph, Vol. 113. American Geophysical Union*, 101–127.
- Chambon, G., Schmittbuhl, J., Corfdir, A., Orellana, N., Diraison, M., Géraud, Y., 2006. The thickness of faults: From laboratory experiments to field scale observations. *Tectonophysics* 426, 77–94.
- Chester, F.M., Logan, J.M., 1986. Implications for mechanical properties of brittle faults from observations of the Punchbowl Fault, California. *Pure and Applied Geophysics* 124, 79–106.
- Childs, C., Manzocchi, T., Walsh, J.J., Bonson, C.G., Nicol, A., Schöpfer, M.P.J., 2009. A geometric model of fault zone and fault rock thickness variations. *Journal of Structural Geology* 31, 117–127.
- Cladouhos, T.T., 1999. Shape preferred orientations of survivor grains in fault gouge. *Journal of Structural Geology* 21, 419-436.
- Cloos, H., 1928. Experimente zur inneren Tektonik. *Centralblatt für Mineralogie und Paläontologie*.
- Coelho, S., Passchier, C., 2008. Mohr-cycles, a 3D representation of geological tensors: The examples of stress and flow. *Journal of Structural Geology* 30, 580-601.
- Coelho, S., Passchier, C., Marques, F., 2006. Riedel-shear control on the development of pennant veins: Field example and analogue modelling. *Journal of Structural Geology* 28, Issue 9, 1658-1669.
- Collettini, C., De Paola, N., Holdsworth, R.E., Barchi, M.R., 2006. The development and behavior of low-angle normal faults during Cenozoic asymmetric extension in the Northern Apennines, Italy. *Journal of Structural Geology* 28, 333-352.

- Davis, G.A., Bump, A.P., Garcia, P.E., Ahlgren, S.G., 1999. Conjugate Riedel deformation band shear zones. *Journal of Structural Geology* 22, 169–190.
- Davis, G.A., Bump, A.P., Garcia, P.E., Ahlgren, S.G., 2000. Conjugate Riedel deformation band shear zones. *Journal of Structural Geology* 22, Issue 2, 169–190.
- Decker, K., 2002. Tektonisch/Strukturgeologische Grundlagen, in: Mandl, G. (Ed.), Erstellung moderner geologischer Karten als Grundlage für karstgeologische Spezialuntersuchungen im Hochschwabgebiet. Geologische Bundesanstalt, Vienna.
- Decker, K., Mechede, M., Ring, U., 1993. Fault slip analysis along the northern margin of the Eastern Alps (Molasse, Helvetic nappes, North and South Penninic flysch, and the Northern Calcareous Alps). *Tectonophysics* 223, 291-312.
- Decker, K., Peresson, H., 1996. Tertiary kinematics in the Alpine–Carpathian–Pannonian system: links between thrusting, transform faulting and crustal extension. in: Wessely, G., Liebl, W. (Eds.), *Oil and Gas in Alpidic Thrustbelts and Basins of Central and Eastern Europe*. EAGE Special Publication, 69–77.
- Decker, K., Peresson, H., Faupl, P., 1994. Die miozäne Tektonik der östlichen Kalkalpen, Kinematik, Paläospannungen und Deformationsaufteilung während der "lateralen Extrusion" der Zentralalpen. *Jahrbuch der Geologischen Bundesanstalt* 137, 5-18.
- Del Ventisette, C., Montanari, D., Sani, F., Bonini, M., 2006. Basin inversion and fault reactivation in laboratory experiments. *Journal of Structural Geology* 28, 2067 - 2083.
- Delvaux, D., 2012. Win\_Tensor, 4.0.3 ed. Damien Delvaux, Tervuren, Belgium.
- Delvaux, D., Sperner, B., 2003. New aspects of tectonic stress inversion with reference to the TENSOR program. in: NIEUWLAND, D. A. (ed.) *New Insights into Structural Interpretation and Modelling*, Geological Society, London, Special Publications 212, 75-100.
- Dooley, T.P., Schreurs, G., 2012. Analogue modelling of intraplate strike-slip tectonics: A review and new experimental results. *Tectonophysics* 574/575, 1–71.
- Dresen, G., 1991. Stress distribution and the orientation of Riedel shears. *Tectonophysics*, 188, 239-247.
- Elter, F.M., Elter, P., Eva, C., Eva, E., Kraus, R.K., Padovano, M., Solarino, S., 2011. Strike-slip geometry inferred from the seismicity of the Northern-Central Apennines (Italy). *Journal of Geodynamics* 52, 379– 388.



- Evans, J.P., Forster, C.B., Goddard, J.V., 1997. Permeability of fault-related rocks, and implications for hydraulic structure of fault zones. *Journal of Structural Geology* 19, Issue 11, 1393-1404.
- Faulkner, D.R., Jackson, C.A.L., Lunn, R.J., Schlische, R.W., Shipton, Z.K., Wibberley, C.A.J., Withjack, M.O., 2010. A review of recent developments concerning the structure, mechanics and fluid flow properties of fault zones. *Journal of Structural Geology* 32, 1557-1575.
- Faulkner, D.R., Lewis, A.C., Rutter, E.H., 2003. On the internal structure and mechanics of large strike-slip fault zones: field observations of the Carboneras fault in southeastern Spain. *Tectonophysics* 367, 235– 251.
- Faulkner, D.R., Mitchell, T.M., Rutter, E.H., Cembrano, J., 2008. On the structure and mechanical properties of large strike-slip faults. in: Wibberley, C. A. J., Kurz, W., Imber, J., Holdsworth, R. E. & Collettini, C. (eds), *The Internal Structure of Fault Zones: Implications for Mechanical and Fluid-Flow Properties*, 139–150.
- Faulkner, D.R., Rutter, E.H., 2003. The effect of temperature, the nature of the pore fluid, and subyield differential stress on the permeability of phyllosilicate-rich fault gouge. *Journal of Geophysical Research*, Vol. 108, NO. B5.
- Frisch, W., Dunkl, I., Kuhlemann, J., 2000. Post-collisional orogen-parallel large-scale extension in the Eastern Alps. *Tectonophysics* 327, 239-265.
- Frisch, W., Gawlick, H.-J., 2003. The nappe structure of the central Northern Calcareous Alps and its disintegration during Miocene tectonic extrusion - a contribution to understanding the orogenic evolution of the Eastern Alps. *International Journal of Earth Sciences* Vol. 92, 712-727.
- Frisch, W., Kuhlemann, J., Dunkl, I., Brügel, A., 1998. Palinspatic reconstruction and topographic evolution of the Eastern Alps during late Tertiary tectonic extrusion. *Tectonophysics* 297, 1-15.
- Frost, E., Dolan, J., Sammis, C., Hacker, B., Cole, J., Ratschbacher, L., 2009. Progressive strain localization in a major strike-slip fault exhumed from midseismogenic depths: Structural observations from the Salzach-Ennstal-Mariazell-Puchberg fault system, Austria. *Journal of Geophysical Research* 114, 1-14.
- Gasser, D., Gusterhuber, J., Krische, O., Puhr, B., Scheucher, L., Wagner, T., Stüwe, K., 2009. Geology of Styria: An Overview. *Mitteilungen des naturwissenschaftlichen Vereins für Steiermark* 139, 5 - 36.

- Gudmundsson, A., 2000. Fracture dimensions, displacement and fluid transport. *Journal of Structural Geology* 22, 1221-1231.
- Hausegger, S., Kurz, W., Rabitsch, R., Kiechl, E., Brosch, F.J., 2010. Analysis of the internal structure of a carbonate damage zone: Implications for the mechanisms of fault breccia formation and fluid flow. *Journal of Structural Geology* 32, Issue 9, 1349-1362.
- Healy, D., Jones, R.R., Holdsworth, R.E., 2006. New insights into the development of brittle shear fractures from a 3-D numerical model of micro crack interaction. *Earth and Planetary Science Letters* 249, 14-28.
- Katz, Y., Weinberger, R., Aydin, A., 2004. Geometry and kinematic evolution of Riedel shear structures, Capitol Reef National Park, Utah. *Journal of Structural Geology* 26, 491–501.
- Kim, Y.-S., Peacock, D.C.P., Sanderson, D.J., 2004. Fault damage zones. *Journal of Structural Geology* 26, 503–517.
- Kim, Y.-S., Sanderson, D.J., 2005. The relationship between displacement and length of faults: a review. *Earth-Science Reviews* 68, 317-334.
- Linzer, H.-G., Decker, K., Peresson, H., Dell'Mour, R., Frisch, W., 2002. Balancing lateral orogenic float of the Eastern Alps. *Tectonophysics* 354, 211-237.
- Linzer, H.-G., Moser, F., Nemes, F., Ratschbacher, L., Sperner, B., 1997. Build-up and dismembering of the eastern Northern Calcareous Alps. *Tectonophysics* 272, 97-124.
- Linzer, H.-G., Ratschbacher, L., Frisch, W., 1995. Transpressional collision structures in the upper crust: the fold-thrust belt of the Northern Calcareous Alps. *Tectonophysics* 242, 41-61.
- Lister, G.S., Williams, P.F., 1983. The partitioning of deformation in flowing rock masses. *Tectonophysics* 92, 1-33.
- Magri, F., Bayer, U., Clausnitzer, V., Jahnke, C., Diersch, H.-J., Fuhrmann, J., Mfillere, P., Pekdegere, A., Tesmere, M., Voig, H., 2005. Deep reaching fluid flow close to convective instability in the NE German basin—results from water chemistry and numerical modelling. *Tectonophysics* 397, 5 –20.
- Mandl, G., 2000. The Alpine sector of the Tethyan shelf - Examples of Triassic to Jurassic sedimentation and deformation from the Northern Calcareous Alps. *Mitteilungen der Österreichischen Geologischen Gesellschaft* 92, 61-77.

- Mandl, G., 2001. Geologische Bundesanstalt - Arbeitstagung 2001 (Hochschwab). Bericht der Geologischen Bundesanstalt Wien. Geologische Bundesanstalt, Wien.
- Means, W.D., 1983. Application of the Mohr-circle construction to problems of inhomogeneous deformation. *Journal of Structural Geology* 5, 279-286.
- Micarelli, L., Benedicto, A., Wibberley, C.A.J., 2006. Structural evolution and permeability of normal fault zones in high porous carbonate rocks. *Journal of Structural Geology* 28, 1214-1227.
- Misra, S., Mandal, N., Chakraborty, C., 2009. Formation of Riedel shear fractures in granular materials: Findings from analogue shear experiments and theoretical analyses. *Tectonophysics* 471, 253–259.
- Mohr, O., 1882. Über die Darstellung des Spannungszustandes und des Deformationzustandes eines Körperelementes und über die Anwendung derselben in der Festigkeitslehre. *Civilingenieur* 28, 113-115.
- Nadai, A., 1950. *Theory of Flow and Fracture of Solids*. McGraw-Hill, New York.
- Nemes, F., Pavlik, W., Moser, M., 1995. Geologie und Tektonik im Salztal (Steiermark) – Kinematik und Paläospannungen entlang des Ennstal-Mariazell-Blattverschiebungssystems in den Nördlichen Kalkalpen. *Jahrbuch der Geologischen Bundesanstalt* 138, 349 - 367.
- Ortner, H., 2003. Local and far field stress-analysis of brittle deformation in the western part of the Northern Calcareous Alps, Austria. *Geol. Paläont. Mitt. Innsbruck* 26, 109-136.
- Passchier, C.W., Urai, J.L., 1988. Vorticity and strain analysis using Mohr diagrams. *Journal of Structural Geology* 10, 755-763.
- Peresson, H., Decker, K., 1997. The Tertiary dynamics of the northern Eastern Alps (Austria): changing paleostress in a collisional plate boundary. *Tectonophysics* 272, 125-157.
- Ramsay, J.G., 1967. *Folding and Fracturing of Rocks*. McGraw-Hill, New York.
- Ramsay, J.G., 1967. *Folding and Fracturing of Rocks*. McGraw-Hill, New York (1967).
- Ratschbacher, L., 1986. Kinematics of Austro-alpine Cover Nappes: Changing Translation Path due to Transpression. *Tectonophysics* 125, 335-356.
- Ratschbacher, L., Frisch, W., Linzer, H.-G., Merle, O., 1991. Lateral extrusion in the Eastern Alps. Part 2: structural analyses. *Tectonics* 10, 257–271.

- Ratschbacher, L., Frisch, W., Neubauer, F., Schmid, S.M., Neugebauer, J., 1989. Extension in compressional orogenic belts: the eastern Alps. *Geology* 17, 404–407.
- Renner, J., Rummel, F., 1996. The effect of experimental and microstructural parameters on the transition from brittle failure to cataclastic flow of carbonate rocks. *Tectonophysics* 258, 151–169.
- Renshaw, C.E., 1996. Influence of subcritical fracture growth on the connectivity of fracture networks. *Water Resources Research* 32, N0. 6, 1519-1530.
- Richard, P., Krantz, R.W., 1991. Experiments on fault reactivation on strike-slip mode. *Tectonophysics* 188, 117-131.
- Riedel, W., 1929. Zur Mechanik Geologischer Brucherscheinungen. *Zentralblatt für Mineralogie, Geologie und Paläontologie*, 354-368.
- Salvani, F., Billi, A., Wise, D.U., 1999. Strike-slip fault-propagation cleavage in carbonate rocks: the Mattinata Fault Zone, Southern Apennines, Italy. *Journal of Structural Geology* 21, 1731-1249.
- Schellart, W.P., 2000. Shear test results for cohesion and friction coefficients for different granular materials: scaling implications for their usage in analogue modelling. *Tectonophysics* 324, 1–16.
- Schmid, S.M., Fügenschuh, B., Kissling, E., Schuster, R., 2004. Tectonic map and overall architecture of the Alpine orogen. *Eclogae geol. Helv.* 97, 93-117.
- Schuster, R., Koller, F., Hoek, V., Hoinkes, G., Bousquet, R., 2004. Explanatory Notes to the Map: Metamorphic Structures of the Alps - Metamorphic Evolution of the Eastern Alps. *Mitt. Österr. Miner. Ges.* 149.
- Sheldon, H.A., Barnicoat, A.C., Ord, A., 2006. Numerical modelling of faulting and fluid flow in porous rocks: An approach based on critical state soil mechanics. *Journal of Structural Geology* 28, 1468-1482.
- Shipton, Z.K., Cowie, P.A., 2003. A conceptual model for the origin of fault damage zone structures in high-porosity sandstone. *Journal of Structural Geology* 25, 333-344.
- Sibson, R.H., 1977. Fault rocks and fault mechanisms. *Journal of the Geological Society* 133, 191-213.
- Sibson, R.H., 1996. Structural permeability of fluid-driven fault-fracture meshes. *Journal of Structural Geology* 18, 1031-1042.

- Storti, F., Billi, A., Salvini, F., 2003. Particle size distribution in natural carbonate fault rocks: insights of non-self-similar cataclasis. *Earth and Planetary Science Letters* 206, 173-186.
- Storti, F., Rossetti, F., Salvini, F., 2001. Structural architecture and displacement accommodation mechanisms at the termination of the Priestley Fault, northern Victoria Land, Antarctica. *Tectonophysics* 341, 141–161.
- Tollmann, A., 1966. Tektonische Karte der Nördlichen Kalkalpen, 1. Teil: Der Ostabschnitt. *Mitteilungen der Geologischen Gesellschaft in Wien*, 59. Band.
- Tollmann, A., 1976. Der Bau der Nördlichen Kalkalpen. Deuticke, Vienna.
- Tollmann, A., 1976. Der Bau der Nördlichen Kalkalpen. Monographie der Nördlichen Kalkalpen, Bd 3 (1976) Deuticke, Vienna.
- Tollmann, A., 1980. Neuergebnisse über die deckentektonische Struktur der Kalkhochalpen. *Mitt. Österr. Geol. Ges.* 71/72, 397 - 402.
- Tollmann, A., 1985. Geologie von Österreich. Franz-Deuticke, Vienna.
- Treagus, S.H., 1986. Some applications of the Mohr diagram for three-dimensional strain. *Journal of Structural Geology* 8, 819-830.
- Twiss, R.J., Marrett, R., 2010. Determining brittle extension and shear strain using fault length and displacement systematics: Part II: Data evaluation and test of the theory. *Journal of Structural Geology* 32, Issue 12, 1978-1995.
- Twiss, R.J., Marrett, R., 2010. Determining brittle extension and shear strain using fault-length and displacement systematics: Part I: Theory. *Journal of Structural Geology* 32, Issue 12, 1960-1977.
- Wagreich, M., 1995. Subduction tectonic erosion and Late Cretaceous subsidence along the northern Austroalpine margin (Eastern Alps, Austria). *Tectonophysics* 242, 63-78.
- Wagreich, M., 2000. A slope-apron succession filling a piggyback basin: the Tannheim and Losenstein Formation (Aptian - Cenomanian) of the eastern part of the Northern Calcareous Alps (Austria). *Mitteilung der Österreichischen Geologischen Gesellschaft* 93, 31-54.
- Wagreich, M., Decker, K., 2001. Sedimentary tectonics and subsidence modelling of the type Upper Cretaceous Gosau basin (Northern Calcareous Alps, Austria). *International Journal for Earth Sciences* 90, 714-726.

- Wang, X., Neubauer, F., 1998. Orogen-parallel strike-slip faults bordering metamorphic core complexes: the Salzach-Enns fault zone in the Eastern Alps, Austria. *Journal of Structural Geology* 20, 799–818.
- Wibberley, C.A.J., Petit, J.-P., Rives, T., 2000. Micromechanics of shear rupture and the control of normal stress. *Journal of Structural Geology* 22, 411- 427.
- Wibberley, C.A.J., Shimamoto, T., 2003. Internal structure and permeability of major strike-slip fault zones: the Median Tectonic Line in Mie Prefecture, Southwest Japan. *Journal of Structural Geology* 25, 59–78.
- Wibberley, C.A.J., Yielding, G., Di Toro, G., 2008. Recent advances in the understanding of fault zone internal structure: a review. in: Wibberley, C. A. J., Kurz, W., Imber, J., Holdsworth, R. E. & Collettini, C. (Eds), *The Internal Structure of Fault Zones: Implications for Mechanical and Fluid-Flow Properties*. 299, 5–33.
- Zhang, X., Jeffrey, R.G., Thiercelin, M., 2007. Deflection and propagation of fluid-driven fractures at frictional bedding interfaces: A numerical investigation. *Journal of Structural Geology* 29, Issue 3, 396-410.

### **3 Changing fluid chemistry during continuous shearing in cataclastic fault zones – a semiquantitative analysis based on cathodoluminescence, microprobe and stable isotope analysis.**

Submitted to Journal of Structural Geology, March 2013

Stefan HAUSEGGER\*, Walter KURZ\*\*

\* Graz University of Technology, Institute of Applied Geosciences, Rechbauerstrasse 12, A-8010 GRAZ, Austria

\*\* University of Graz, Institute of Earth Sciences, Heinrichstrasse 26, A-8010 GRAZ, Austria

#### **3.1 Abstract**

Brittle fault rock samples from carbonate shear zones along the Salzach-Ennstal-Mariazell-Puchberg fault system (SEMP) have been analyzed using cathodoluminescence microscopy (CL), microprobe analysis and stable isotope composition. The combination of these analytical methods provides an insight into comminution processes and fluid chemistry. The reconstruction of the evolution of fluid chemistry leads to a chronological classification of five fluid phases with respect to fluid chemistry, CL behavior and related structural processes. Initial cataclasis is accompanied by dedolomitization processes along crystal borders and intragranular fractures derived by Ca-rich fluids (Phase P1). Subsequent fluid phases (P2-P5) are characterized by variable Fe- (and Si-content) and therefore variable CL behavior.

Microprobe element mappings support the discrimination of Fe-enriched, non luminescent phases and Ca- and Mn-enriched fluids with bright luminescent calcite precipitations. Fe-enriched carbonates and Fe-hydroxide precipitation indicates fluid circulation in deeper parts of the stratigraphic sequence. These fluids are assumed to be derived from underlying clastic sequences of the Werfen Formation. Stable isotope signatures ( $\delta^{13}\text{C}$  and  $\delta^{18}\text{O}$ ) indicate mainly meteoric origin of penetrating fluids and variable amounts of fluids in the fault zone.

**Keywords:** Fluid chemistry, Brittle fault zones, Cathodoluminescence, Stable isotopes, Northern Calcareous Alps.

### 3.2 Introduction

The basic approach to investigations on fluid flow and fluid chemistry in fault zones depends on various factors. Lithology of the host rock, deformation mechanisms (brittle, brittle/ductile, ductile) and the structural evolution of the fault zone are decisive for potential pathways for fluid flow (e.g., Marquer and Burkhard 1992; Sample et al. 1993; Conti et al. 2001; Cello et al. 2001b; Abart et al. 2002; Bellot 2007; Billi et al. 2007; Gabrielov et al. 2007; Fitz-Diaz et al. 2011). Besides structural analysis of fault zones and macroscopic investigations, micro-structural and geochemical analyses are essential for studies in this research field. Hence, the selected combination of analytical methods is diverging and, amongst others, primarily comprises petrographic- and cathodoluminescence microscopy, stable isotope analysis, fluid inclusion analysis and determination of major and trace elements by different analytical methods (e.g., Bustillo et al. 1992; Janssen et al. 1998; Caine and Foster 1999; Cello et al. 2001; Cello et al. 2001b; Pili et al. 2002; Marfil et al. 2005; Micarelli et al. 2005; Barker Shaun et al. 2006; Hausegger et al. 2010).

This study is based the structural investigations and results from Hausegger and Kurz (submitted) and comprises multiple analytical methods in order to obtain a semi-quantitative assessment on changing fluid chemistry in brittle carbonate shear zones during continuous shear. Microscopic analysis (petrographic microscopy and cathodoluminescence) are combined with microprobe analysis (backscattered electron images and element mappings) and stable isotope analysis. Data from X-ray diffraction and ICP OES supported the interpretation of microscopic and geochemical data. This combination led to a chronological sequence of (1) changing fluid chemistry and (2) related deformation and fluid-rock interactions, respectively.

### 3.3 Site description

Investigated sites are located in the southernmost part of the Northern Calcareous Alps (Fig. 3-1). These transgressively overly the Greywacke Zone (e.g., Bauer 1998; Linzer et al. 2002; Frisch and Gawlick 2003; Schmid et al. 2004) which is characterized by a Paleozoic volcanic-sedimentary evolution. The study sites are located within the



Mürzalpen nappe that comprises to Mesozoic cover sequences of Permian to Scythian clastic terrigenous sediments at the base, overlain by massive platform carbonates (e.g., Mandl, 2000). The tectonic evolution of the Northern Calcareous Alps is characterized by multiple phases of nappe stacking from the Late Jurassic to the Early Cretaceous, Late Cretaceous extension and post Middle Miocene orogen-parallel strike-slip faulting (e.g., Linzer et al. 1995; Nemes et al. 1995; Linzer et al. 1997; Peresson and Decker 1997; Frisch and Gawlick 2003; Schmid et al. 2004). The northern margin of the Mürzalpen nappe is formed by the sinistral Oligocene-Miocene Salzach-Ennstal-Mariazell-Puchberg (SEMP) fault system (e.g., Ratschbacher et al. 1989; Ratschbacher et al. 1991; Decker et al. 1993; Decker and Peresson 1996; Linzer et al. 1997; Wang and Neubauer 1998; Frisch et al. 2000) (Fig. 3-1).

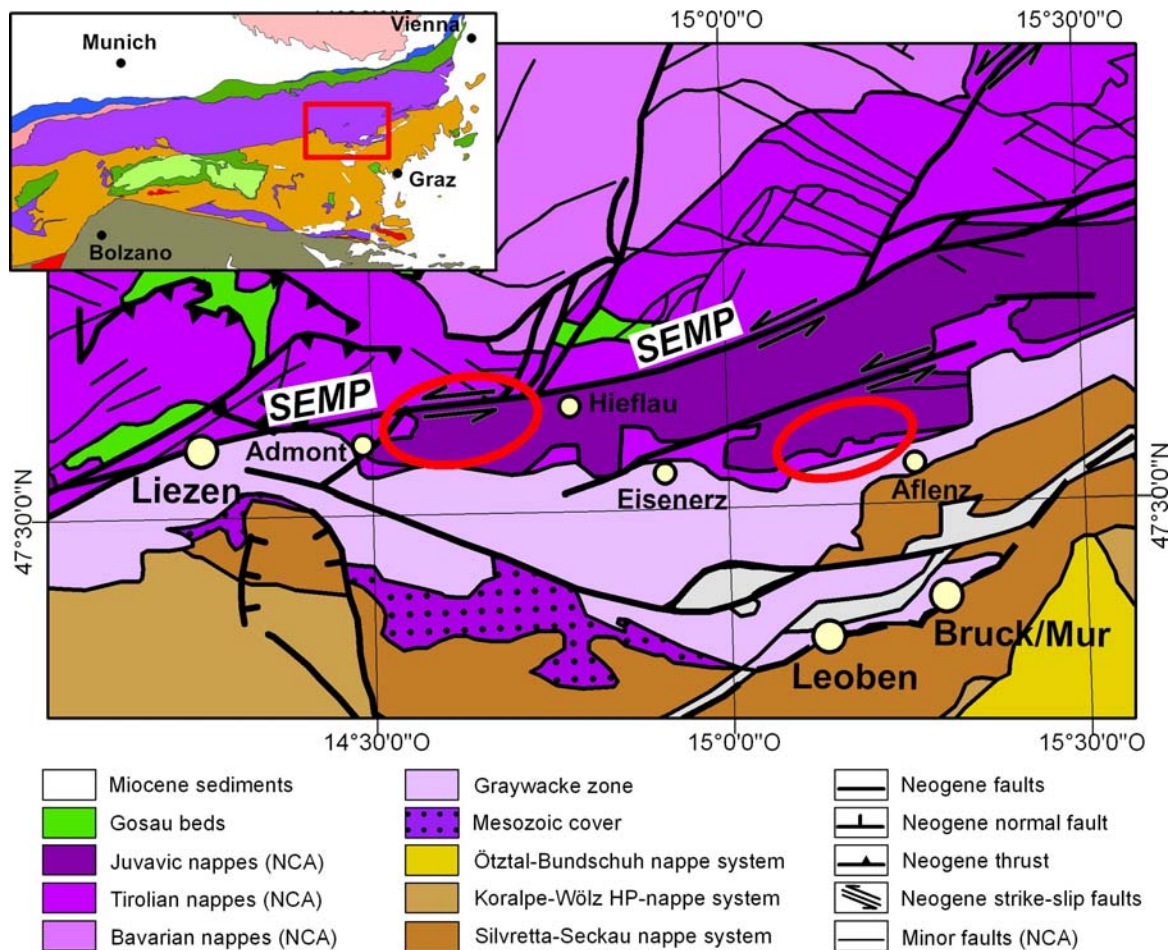


Figure 3-1: Geological overview of the Eastern Alps (top left) and location of working areas (after Schmid et al., 2004). Sites are encircled. Site Haindlkar is situated in the western part between Admont and Hieflau in the Gesäuse Mountains. Site Brandwald and Fölz represent the eastern part of the working area North of Aflenz on the south side of the Hochschwab massif.

This study focuses on three different sites in the Ladinian Wetterstein-limestone/ -dolomite units of the Mürzalpen nappe (Fig. 3-1). Site Haindlkar is located in the Gesäuse Mountains and directly affected by the Ennstal/Gesäuse fault, a segment of the SEMP fault system. Site Brandwald and Fölz represent the eastern part of the study area on the south side of the Hochschwab massif (Fig. 3-1).

Nomenclature of structural elements follows common classifications (following e.g., Caine et al. 1996; Caine and Foster 1999; Billi et al. 2003; Kim et al. 2004; Faulkner et al. 2010) and discriminate between host rock, damage zone, transition zone and fault core. Fault type classification was adopted from Hausegger and Kurz (submitted) which describes a continuous evolution due to increasing displacement from initial fault type III over fault type II to mature fault type I.

Fault type I is characterized by the most complex internal fault core structure. Several domains of cataclasites, shear bands and relictic lenses of damage zone matter are bordered by internal fault planes or gradual transition zones to adjacent domains. Type I fault cores reach widths of several 10's of meters. Fault type II represents an intermediate stage of development from fault type III (thin solitary cataclastic layers) towards fault type I. Type II fault cores are classified by an advanced internal segmentation of one to several shear bands and thicknesses up to 100 cm. Both fault types show typical asymmetric cross sections. Fault cores are bordered by at least one master fault plane and, in some parts along strike, a variable transition zones towards the damage zone (Hausegger and Kurz, submitted).

### **3.4 Methods**

Coincidentally to field data acquisition and structural analysis (Hausegger and Kurz, submitted), oriented samples from all structural elements (host rock, damage zone and fault core) of fault zones were taken at the three sites described above. Virtually cubic hand samples with an average edge length of approximately 10 to 15 centimeters were cut out with a power saw in order to get sufficient sample size without destruction by hammer stroke or a drilling bit.

### 3.4.1 Sample preparation

In-cohesive and highly fractured specimens were stabilized with synthetic resin. All samples were saw-cut into several sections with respect to the orientation of the related fault zone. Thin-sections for petrographic microscopy, as well as polished and carbon-coated thin sections for cathodoluminescence- and microprobe analysis were prepared at the University of Graz, Institute of Earth Sciences. Powder samples for stable isotope analysis were collected with a micro-drilling gear and categorized in “host rock”, “components” (cataclasite particles), “matrix/cement” (mainly comminuted dolomite), and “calcite cement”.

### 3.4.2 Optical microscopy and cathodoluminescence

Optical microscopy on a petrographic microscope was conducted at the Institute of Applied Geosciences, Graz University of Technology, on a Leica DMLP microscope equipped with an Olympus DP26 digital camera. Digital overview images were recorded in order to locate areas of special interest for subsequent Cathodoluminescence (CL) analysis.

CL microscopy was executed on polished and carbon-coated thin-sections with a Lumic HC5-LM cathodoluminescence microscope at the Department of Lithospheric Research, University of Vienna. The electron beam of this stage is supplied by a heated filament (“hot cathode”) delivering true color CL images. Acceleration voltage was fixed at 14 kV, beam current varied from 0,14 to 0,21 mA. Digital high-resolution images were recorded through the basically petrographic microscope with a high sensitivity CCD Kappa PS 4/40 camera and subsequently processed with common image editing software packages. Cathodoluminescence (CL) analysis is a powerful tool for the investigation of carbonate rocks and used for visualization of petrographic features which are often not visible in conventional transmitted-light microscopy (e.g., ten Have and Heijnen 1985; Budd et al. 2000; Habermann et al. 1996; Gillhaus et al. 2000; Götz 2002; Lee et al. 2005; Boggs and Krinsley 2006). CL behavior is generally triggered by the amount and/or ratio of certain elements. The main activation element in carbonates is  $Mn^{2+}$ , causing orange to red luminescence colors at a minimum concentration of ~20 to 40 ppm. Pairs of REE (e.g.,  $Eu^{2+}$  and  $Eu^{3+}$  or  $Tb^{3+}$  and  $Dy^{3+}$ ) can also act as activators and/or influence the colors of  $Mn^{2+}$ -activated luminescence (e.g., Habermann et al. 1996, Marchel 2000, ten Have and Heijnen, 1985). Main sensitizers for  $Mn^{2+}$ -activated luminescence in carbonates are  $Pb^{2+}$  and  $Ce^{3+}$ . In natural carbonates  $Fe^{2+}$  is considered as the main quencher of  $Mn^{2+}$ -activated luminescence, being effective from a concentration of ~30 to 35 ppm (Marchel,

2000). In this study CL analysis gives contribution to the understanding and interpretation of diagenesis, deformation history and fluid flow in carbonate fault rocks. Furthermore, microprobe analysis was an important application for the evolutionary interpretation of investigated fault rocks. Backscattered electron emission (BSE) images provide an overview of the chemical composition and contribute to the interpretation of brittle deformation and comminution. Element mappings of main (Ca, Mg) and minor (Si, Fe, Mn, Al) elements complete the assembly of analytical micro-scale applications.

### **3.4.3 Microprobe analysis**

Polished and carbon-coated samples were analyzed by electron microprobe analysis (EMPA) using a JEOL JXA8200 at the University of Leoben, Austria. Backscattered electron emission (BSE) images were collected at an accelerating voltage of 15 kV and a beam current of 5 nA. Qualitative single-spot analyses were conducted by energy dispersive X-ray spectrometry (EDS) in order to determine main and accessory mineral phases using magnifications from 40x (overview) up to 600x for details.

Selected areas were analyzed by wave-length dispersive X-ray spectrometers (WDS) with 600x magnification in order to get element mappings for main (Ca, Mg) and minor elements (Si, Fe, Mn). Analyses were conducted with constant accelerating voltage of 15 kV. Probe current ranged from 50 to 90 nA with variable dwell time from 16 to 25 ms in intervals from 0.46 x 0.46 to 2 x 2  $\mu\text{m}$ . The content of each element is stated by the detection level (counts per second), aligned with respect to measurement conditions and evaluated with knowledge from CL and optical microscopy. Hence, element map color levels of images from each site are comparable and support interpretation of micro-structural and geochemical processes.

### **3.4.4 Stable isotope composition**

Stable isotope geochemistry was used in order to determine  $\delta^{18}\text{O}$  and  $\delta^{13}\text{C}$  isotopic composition of host rock, cataclasite fragments (components), cataclasite matrix/cement and secondary vein fillings. Discussed and displayed data of 30 different samples were analyzed at the isotope lab of the Joanneum Research Forschungsgesellschaft mbH (Graz, Austria) using a Gasbench II for automated continuous-flow gas preparation coupled to a Finnigan DELTAplus XP Mass Spectrometer. Stable isotope results are reported in  $\delta$ -notation. All  $\delta$ -values have been normalized into the V-PDB scale. Analytical

techniques, experimental conditions and data corrections are described in Dietzel et al. (2009) and Hausegger et al. (2010).

### **3.4.5 Inductively coupled plasma spectrometry (ICP)**

Inductively coupled plasma optical emission spectrometry (ICP-OES), synonym for inductively coupled plasma atomic emission spectroscopy (ICP-AES), is a very common tool in numerous scientific fields e.g., Hou and Jones (2000), Montaser (1992), Nölte (2002), Todoli and Mermet (2008). This analytical technique provides qualitative and quantitative detection of a broad spectrum of elements. ICP-OES analysis was conducted on samples of cement-, matrix-, fragment- and host rock material with a Perkin Elmer Optima 4300 at the Institute of Applied Geosciences, University of Graz. Main elements (Ca, Mg) were detected in order to differentiate calcite and dolomite and to support the interpretation of deformation and fluid-rock interaction (dedolomitization).

## **3.5 Results**

### **3.5.1 Site Haindlkar**

Fault core cataclasites from the major fault zone at site Haindlkar (fault type I) are composed of dolomite components embedded in a fine grained matrix of comminuted dolomite matter (Fig. 3-2a, b). Cathodoluminescence analysis (Fig. 3-2c) exhibits typical dull to dark red colors for dolomite components. Distinct bright red luminescence is visible along crystal borders and intra-granular fractures, respectively. Though the matrix material is dolomite, luminescence along crystal borders causes bright red luminescence of areas composed of fine grained matrix material.

Damage zone samples of minor faults, sub-parallel to the main fault direction (fault type II) are characterized by calcite veins and pore fillings in a dolomite host rock. Analogue to fault core cataclasites (Fig. 3-2a-c) the dolomite parent rock material shows dull red luminescence, whereas bright red colors are concentrated along crystal borders and intra-granular fractures, respectively. Secondary calcite pore fillings offer no luminescence and stay dark (Fig. 3-2f).



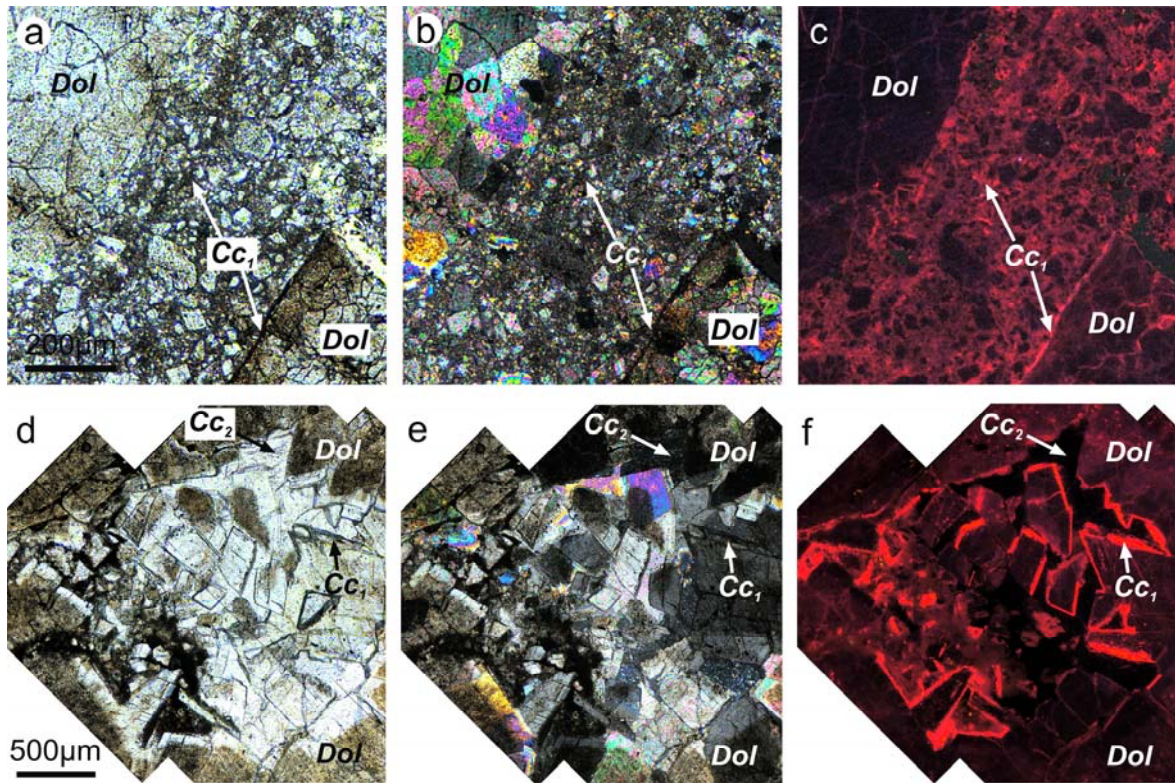


Figure 3-2: (a) Plane-light, (b) cross-polarized light and (c) CL image of a dolomite fault core cataclasite from site Haindkar (sample G7).

(d) Plane-light, (e) cross-polarized light and (f) CL image of a damage zone rock sample from site Haindkar (sample H4).

Parent rock material is dolomite ('Dol') with secondary calcite fillings and dedolomitized crystal rims and matrix material ('Cc<sub>1</sub>').

Microprobe analysis, BSE images as well as element mappings, of described samples (Fig. 3-3) support the results from optical microscopy and CL. The matrix of the fault core cataclasite (Fig. 3-2a-c) consists of comminuted dolomite material derived from the parent rock (Fig. 3a). Element mappings of Ca and Mg show a slight decrease of especially Mg along crystal borders and intra-granular fractures (Fig. 3-3d, g). Subsequent to brittle deformation/comminution of dolomite host rock, a further phase of brittle deformation left an imprint, visible as deformation band from the lower right corner to the middle of the left edge of the image (Fig. 3-3a, d, g, j). The compiled map of Si and Al distribution (Fig. 3-3j) underlines this feature and classifies this deformation band and matrix as area of increased Si content.

The parent rock material of the investigated damage zone shows similar composition of Ca and Mg with respect to the fault core cataclasite (Fig. 3-3e, f, h, i). However, pore volumes and fractures are filled with secondary calcite with almost no Mg (Fig. 3-3e, f). In element mappings of Fe (Fig. 3-3k, l) a slight increase of Fe is visible in calcite fillings, which is responsible for quenched luminescence of these areas (Fig. 3-2f).



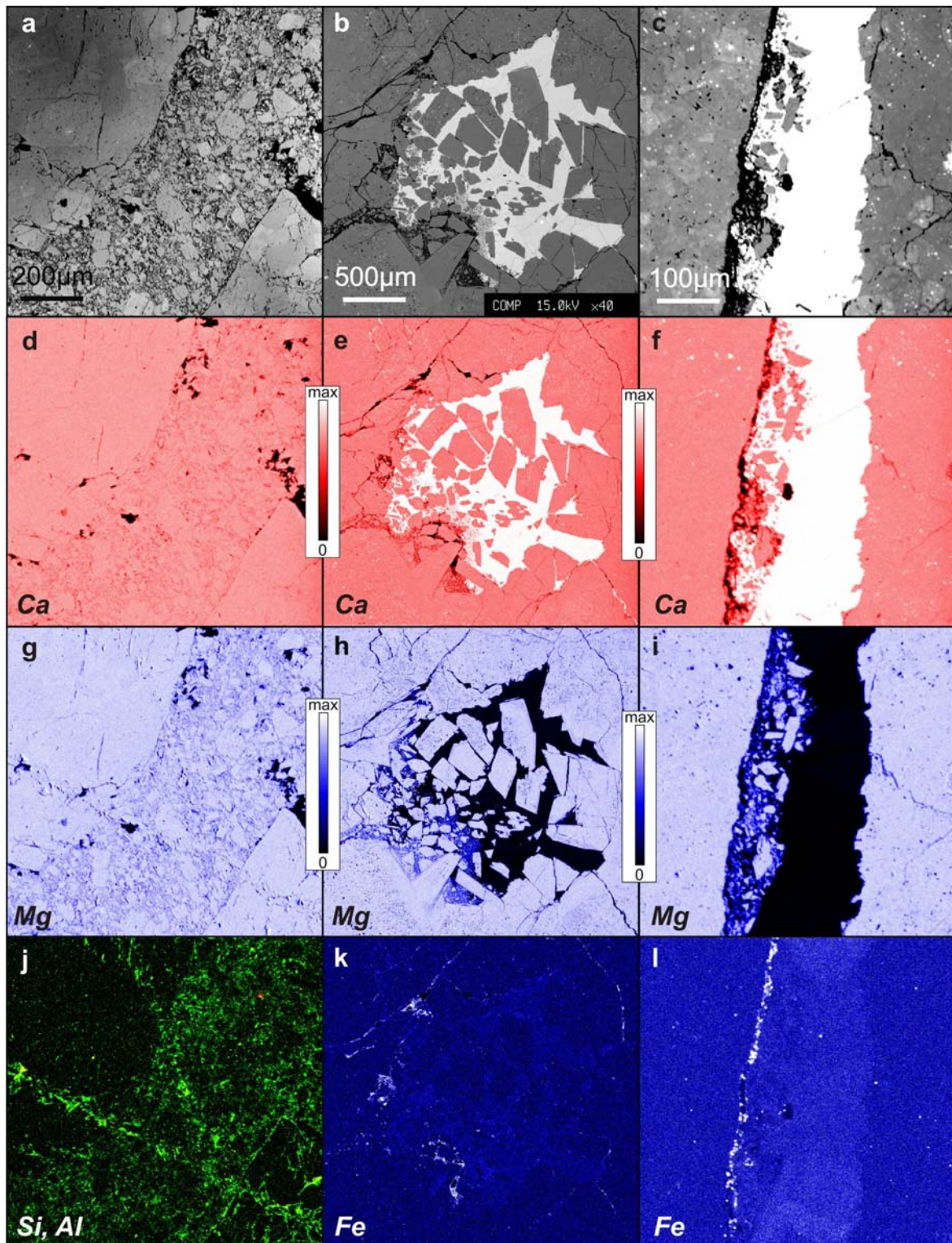


Figure 3-3: BSE image of (a) fault core cataclasite (sample G7), (b) damage zone (sample H4) and (c) detailed image of a damage zone calcite vein. All samples from site Haindlkar. In BSE images calcite is shown in bright grey to white and dolomite in dark grey colors. (d-f) Mapping of Ca content. (g-i) Mapping of Mg content. (j) Compiled element mapping of Si and Al of sample G7 (fault core cataclasite). (k, l) Fe mapping of sample H4 (damage zone) showing slightly increased Fe contents which quenches CL in areas of secondary calcite.



### 3.5.2 Site Brandwald

At site Brandwald samples from two different fault core cataclasites were analyzed. Minor fault type II cataclasites (Fig. 3-4a-c) consist of dolomite components in a very fine grained dolomite matrix. Subsequent fractures and pore volumes are partly filled with secondary calcite and Fe-hydroxides. CL shows typical dark to dull red luminescence colors of dolomite components. As already described at site Haindlkar crystal borders and intra-granular fractures exhibit bright red luminescence. Hence, the matrix area, composed of very fine grained dolomite, appears like an almost continuous area of bright luminescence.

Fault core cataclasites from the main fault zone at site Haindlkar (fault type I) also consist of dolomite components and comminuted, fine grained matrix material (Fig. 3-4d, e). Additionally calcite cement and vein fillings are dominant in this sample (Fig. 3-4d, f). In CL images (Fig. 3-4f) dolomite components and matrix areas show dull red luminescence but appear slightly brighter than components in Fig. 3-3c. Bright red luminescence is visible along crystal borders and intra-granular fractures but also in irregular shaped areas inside dolomite components. Calcite cements and vein fillings stay dark under the bombardment of the hot cathode (Fig. 3-4f).

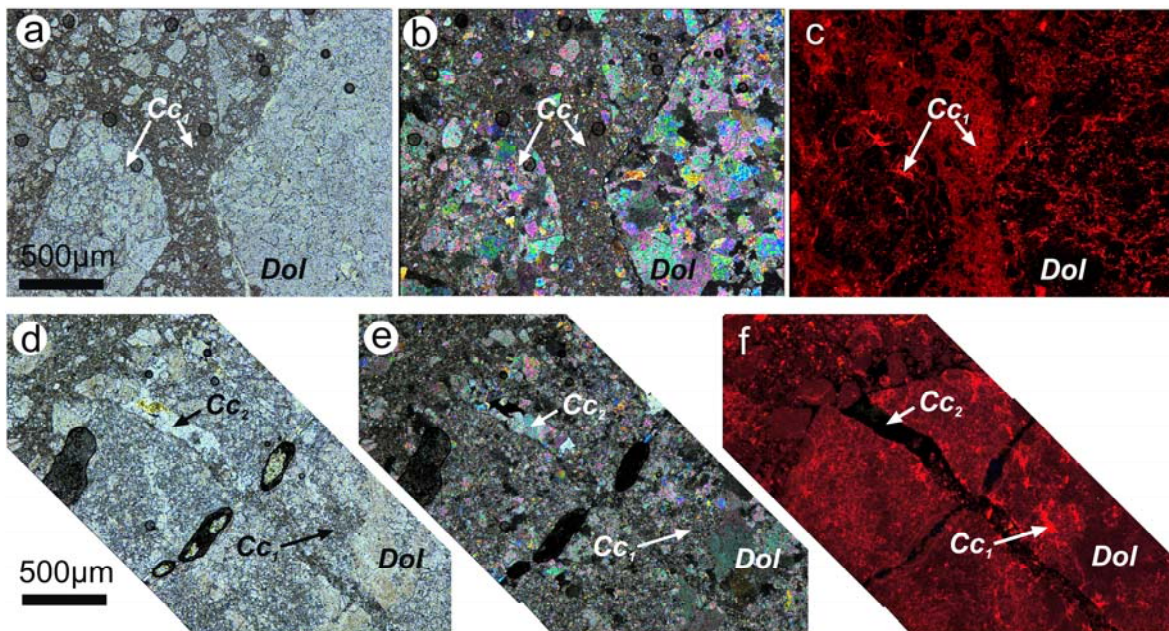


Figure 3-4: (a) Plane-light, (b) cross-polarized light and (c) CL image of a fault core cataclasite from site Brandwald (fault type II; sample B8).

(d) Plane-light, (e) cross-polarized light and (c) CL image of the main fault core cataclasite from site Brandwald (fault type I; sample B11).

Parent rock material is dolomite ('Dol') with secondary calcite fillings, dedolomitized crystal rims and matrix material ('Cc<sub>1</sub>') as well as subsequent calcite veins ('Cc<sub>2</sub>').



Element mappings and BSE images of cataclasites from minor faults (Fig. 3-5a, d, g, j) underline impressions from optical microscopy and CL. Components as well as comminuted matrix material mainly consist of dolomite. Element mappings of Ca and Mg support results from CL analysis and express a decrease of Mg along crystal borders and intra-granular fractures (Fig. 3-5d, g). Compiled Fe-Mn mappings (Fig. 3-5j) clearly indicate Fe-rich (Fe-hydroxide) vein fillings in intra- and inter-granular fractures and crystal borders.

Derived from the same dolomite parent rock material, fault type I cataclasites can be distinguished by the presence of calcite cement and calcite vein fillings in intra-granular fracture (Fig. 3-5b, c). Similar to minor faults (Fig. 3-5a) a decrease in Mg is detected along crystal borders (Fig. 3-5e, h, k) as well as Fe-rich crack fillings. However, Ca-rich (calcite) cement and vein fillings (Fig. 5e, f) differ this cataclasite type from type II fault core samples in Fig. 3-5a, d, g, j. Compiled Fe-Mn mappings exhibit slightly increased Fe-contents in areas of calcite cements and fillings (Fig. 3-5k, l). This change in Fe-content is manifested in the missing luminescence of this calcite generation.

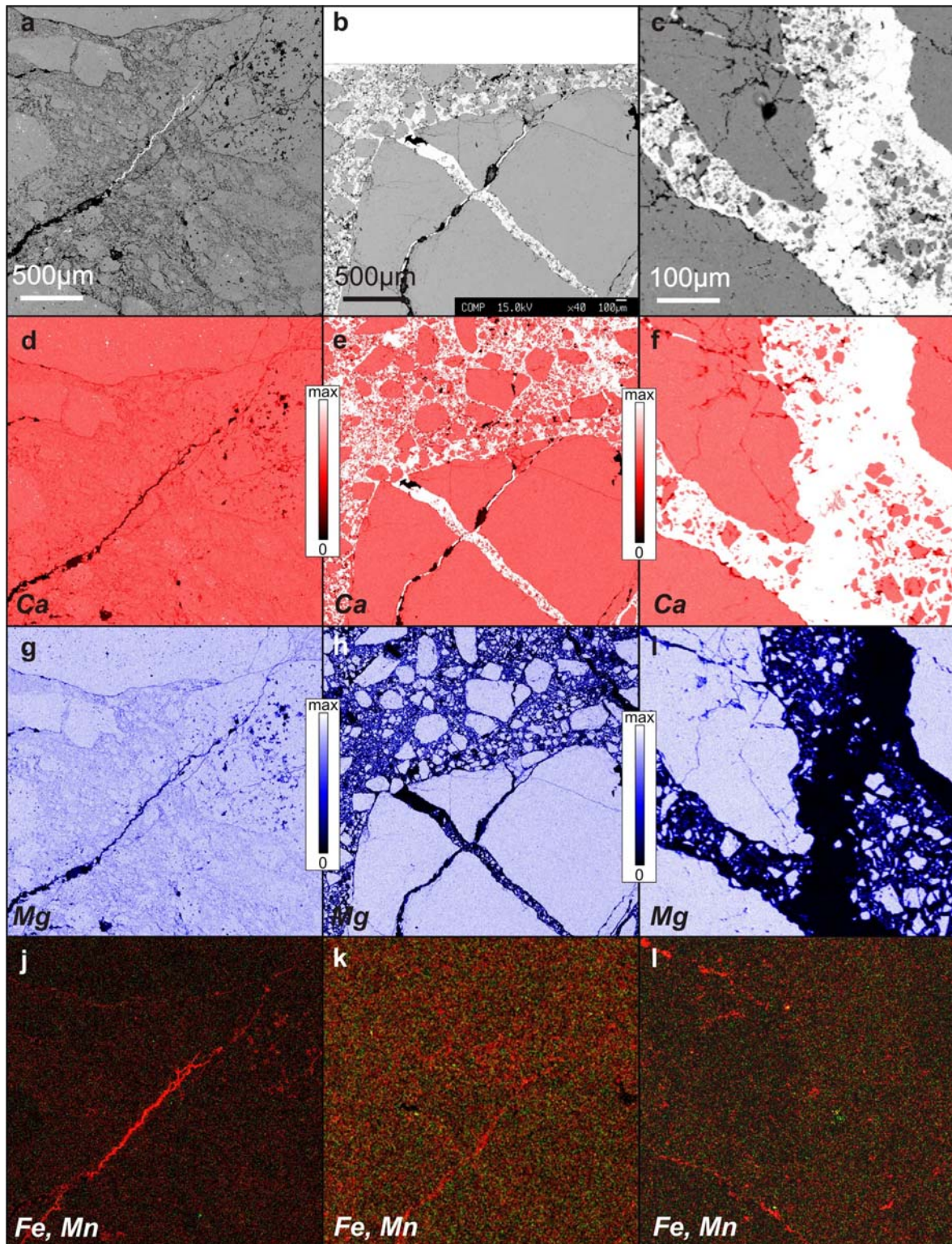


Figure 3-5: BSE image of (a) fault core cataclasite (fault type II; sample B8), (b) fault core cataclasite (fault type I; sample B11) and (c) detailed image of a calcite vein in fault type I cataclasites. Calcite and Fe-rich vein fillings (a) is shown in bright grey to white and dolomite in dark grey colors. (d-f) Mapping of Ca content. (g-i) Mapping of Mg content. (j-l) Compiled Fe-Mn mappings express areas of increased Fe-content (brighter areas and red veins).

### 3.5.3 Site Fölz

Former structural analysis (Hausegger and Kurz, submitted) identified this site as shear zone with a complex structural evolution and in close range to the underlying Permian to Scythian clastic Werfen formation. Investigated fault cores from site Fölz consist of ultracataclasites (Fig. 3-6a – f) and cataclasites (Fig 3-6g-i), both derived from dolomite host rocks.

Ultracataclasites are built up by dolomite components, particle diameter from 10 to 50  $\mu\text{m}$ , embedded in a fine grained, calcite matrix (Fig. 3-6a, b, d, e). Bands of increased dolomite components and calcite matrix, respectively, exhibit a quasi-layered internal structure. Vein fillings show a distinct zonation of quartz along the rims and calcite inside the vein (Fig. 3-6a-f). Quartz-rich areas stay dark in CL, whereas dolomite components exhibit typical dull red luminescence. Calcite, whether cement/matrix or vein fillings, glares in bright red colors. Furthermore, CL exposes an internal zonation of calcite vein fillings, represented by small bands of brighter luminescence towards quartz vein rims (Fig. 3-6c). Fault core cataclasites (Fig. 3-6g-i) consist of dolomite components in a matrix of comminuted dolomite material and calcite cement in inter-granular pore volumes and intragranular fractures. Microscopy and CL images display different generations of quartz and calcite vein fillings (Fig. 3-6g-i). In CL images dolomite components stay dull red but calcite filled intra- and inter-granular volumes show bright red luminescence. Quartz filled as well as discordant calcite filled veins show no luminescence (Fig. 3-6i).



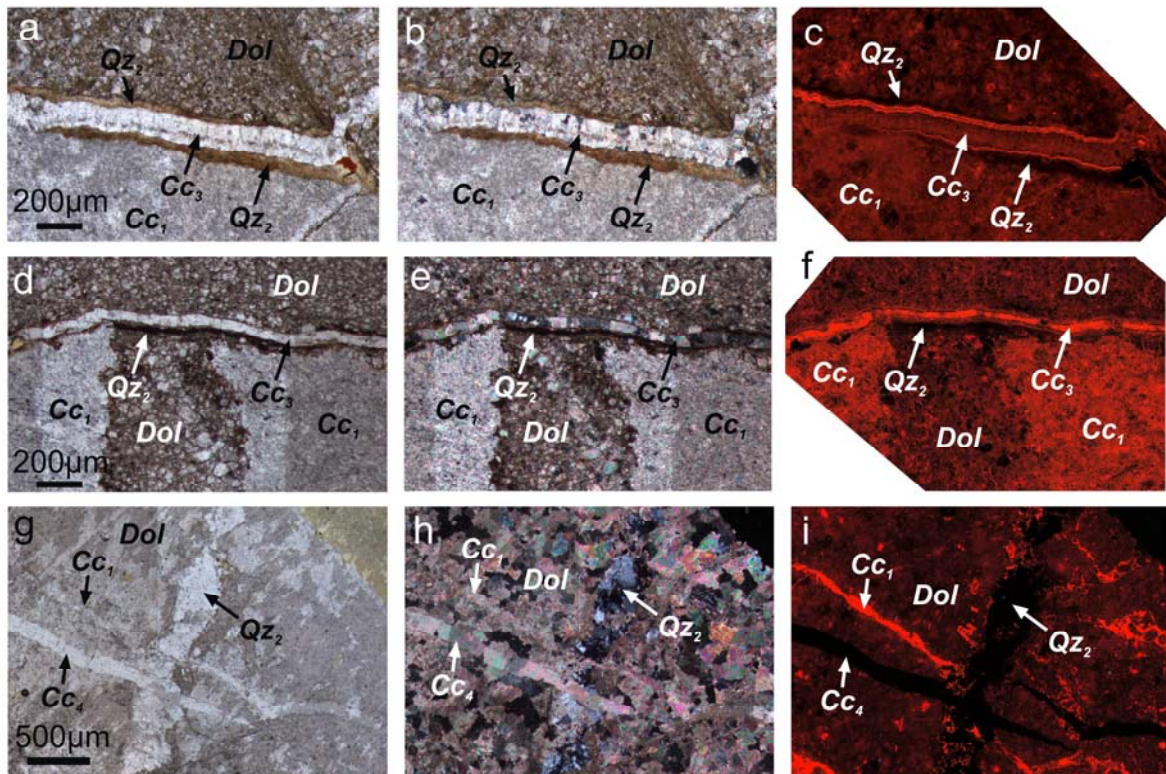


Figure 3-6: (a, d) Plane-light, (b, e) cross-polarized light and (c, f) CL image of an Ultracataclasite from site Fölz (samples EA1, EA2). (g) Plane-light, (h) cross-polarized light and (i) CL image of a fault core cataclasite from site Fölz (sample R14). Parent rock material is dolomite ('Dol'). Dedolomitized material and vein fillings ('Cc<sub>1</sub>'), quartz filled veins ('Qz<sub>2</sub>') and subsequent calcite veins ('Cc<sub>3</sub> and Cc<sub>4</sub>') are distinguished.

BSE images and element mappings of Ca and Mg of ultracataclasite samples (Fig. 3-7a, b, d, e, g, h) show distinct bordered areas of dolomite components embedded in calcite cement/matrix. Surrounded by calcite filled veins, areas of almost pure calcite matter without any dolomite components are visible in Fig. 3-7a, d, g, h below the calcite vein and Fig. 3-7b, e, h, k on the left and right image border below the calcite vein. Cataclasite fault core samples consist of dolomite components and mainly calcite cement and vein fillings (Fig. 3-7c, f, i). Combined Fe-Mn element mappings show very low Fe contents in primary calcite cement and vein fillings. This lack of Fe-quenching is visible as bright red to orange luminescence.



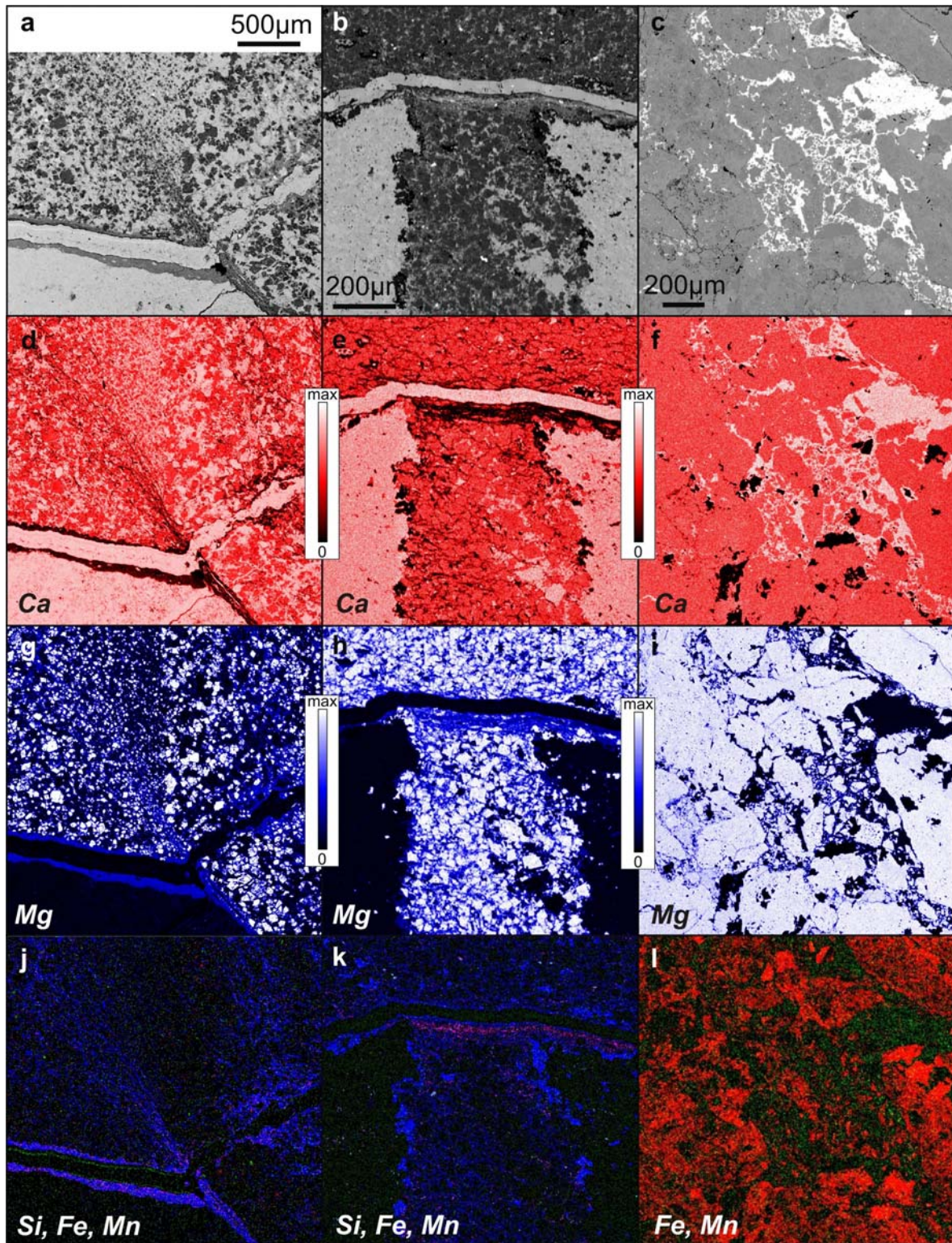


Figure 3-7: BSE image of (a, b) ultracataclasite (samples EA1 and EA2) and (c) fault core cataclasites (sample R14). Calcite (Ca) is shown in bright grey to white and dolomite (Mg) in dark grey colors. (d-f) Mapping of Ca content. (g-i) Mapping of Mg content. (j, k) Compiled element mapping of Si, Fe and Mn of ultracataclasite samples EA1 and EA2 showing constant Mn distribution (dark) and increased Fe- (purple) and Si- (blue) content in the outer rims of calcite filled veins and in intergranular pore volume. (l) Compiled Fe-Mn mapping of cataclasite sample R14. Mn shows constant distribution (green), whereas Fe content (red) in calcite areas is very low.

### 3.6 Stable isotope analysis

At site Haindlkar host rock and cataclasite components show constant  $\delta^{13}\text{C}$  values from 3.16 to 3.93 ‰ and variable  $\delta^{18}\text{O}$  values from host rock to components from 1.49 to -0.47 ‰. Cataclasite matrix/cement exhibits similar  $\delta^{18}\text{O}$  values with respect to components but shows more variable  $\delta^{13}\text{C}$  values from 1.86 to 3.38 ‰ (Fig. 3-8).

Stable isotope composition at site Brandwald shows similar patterns with respect to site Haindlkar. Host rock and cataclasite components plot in a field of uniform  $\delta^{13}\text{C}$  values (2.90 to 3.74 ‰) and variable  $\delta^{18}\text{O}$  values from -2.31 to 0.18 ‰. Cataclasite matrix/cement generally shows lower values for  $\delta^{18}\text{O}$  than host and components (-3.94 to -1.38 ‰). Similar to site Haindlkar, matrix/cement is more variable in  $\delta^{13}\text{C}$  values and ranges from -1.96 to 3.46 ‰. However, matrix/cement samples plot in a wider field of stable isotope composition (Fig. 3-8).

All types of samples from site Fölz plot in a narrow band of  $\delta^{13}\text{C}$  values from 2.63 to 4.29 ‰. Variations in  $\delta^{18}\text{O}$  values range from -4.84 to -1.31 ‰. Dolomite host rock material plots in a  $\delta^{18}\text{O}$  range from -2.38 to -1.34 ‰. Cataclasite components show lower  $\delta^{18}\text{O}$  values with respect to host rocks and range from -4.84 to -2.44 ‰. Comminuted matrix matter plots in a  $\delta^{18}\text{O}$  field similar to components from -3.68 to -2.24 ‰. Calcite cement and vein fillings show similar  $\delta^{18}\text{O}$  values with respect to matrix material but tend towards lower  $\delta^{13}\text{C}$  values from 2.63 to 3.14 ‰ (Fig. 3-8).



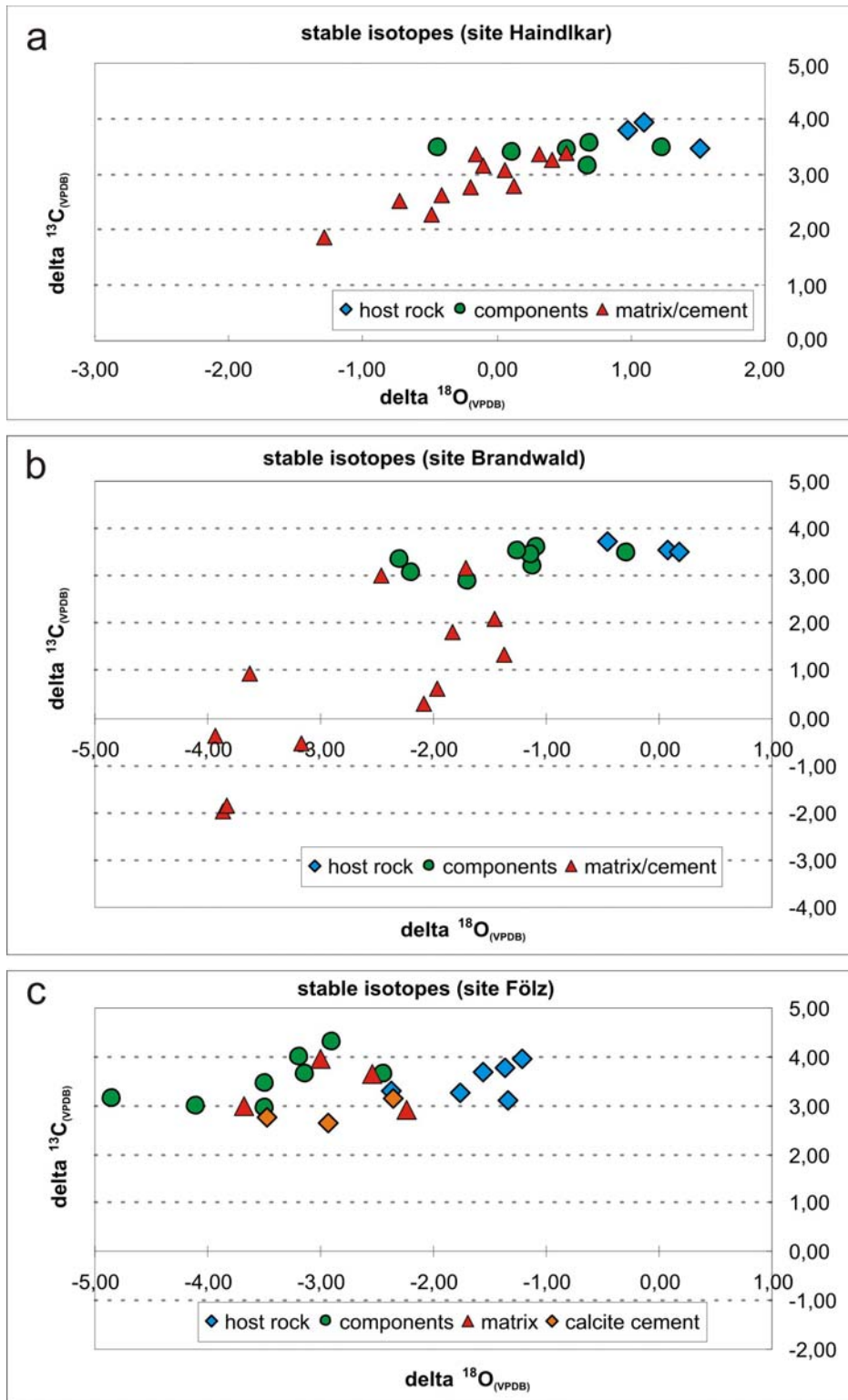


Figure 3-8: Stable isotope compositions ( $\delta^{13}\text{C}$  and  $\delta^{18}\text{O}$  in ‰) of host rock slices as well as cataclasite components, cataclasite matrix and secondary calcite cement from fault core samples from (a) site Haindlkar, (b) site Brandwald and (c) site Fölz.

All sites indicate the tendency of decreased  $\delta^{18}\text{O}$  values in the course of evolution from host rock to cataclasite components and matrix/cement. (a, b) Dedolomitised matrix material from site Haindlkar and Brandwald show decreased  $\delta^{13}\text{C}$  values.

## **3.7 Discussion**

### **3.7.1 Fault development and comminution**

Macroscopic structural investigations on brittle fault zones in the study areas have identified multiple deformation events. Development of brittle shear zones depend on paleostress orientation and pre-existing discontinuities in the development of brittle shear zones (Hausegger and Kurz, submitted). The structural evolution is decisive for potential fluid flow, subsequent chemical alterations and fluid-rock interactions (e.g., Crampin 1999; Conti et al. 2001; Cello et al. 2001b; Billi et al. 2007). Microscale, mainly microprobe analysis illustrates comminution processes and gives contribution to further chemical development of fault rocks (Figs. 3-3a-c; 3-5a-c; 3-9). Dolomite components are mainly separated along crystal borders and intragranular fractures from parent rock material. Subsequent rotation continuous comminution and arranges a fine grained matrix of mainly dolomite matter between the components (Figs 3-3a; 3-5a).



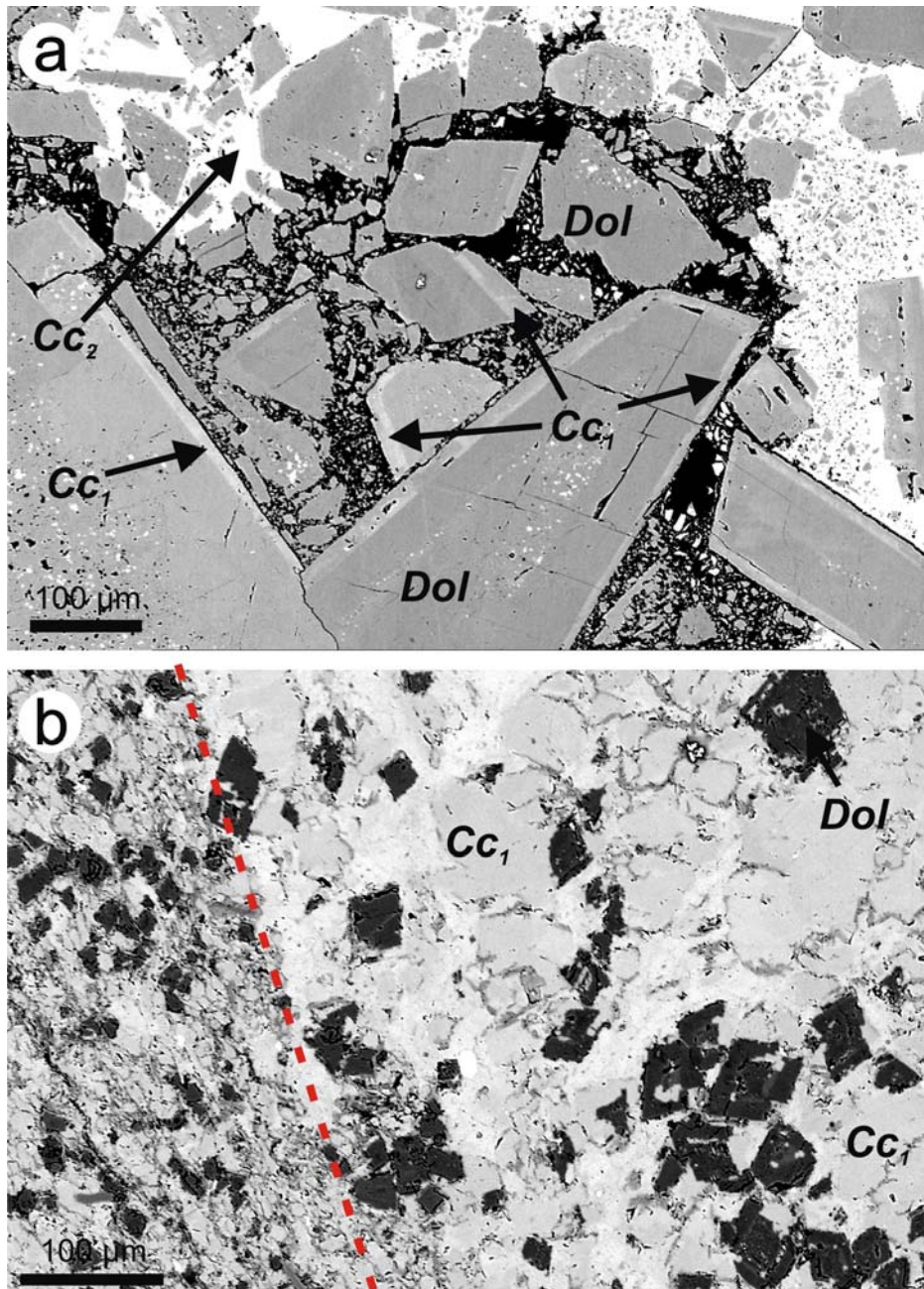


Figure 3-9: BSE images to illustrate dedolomitization and comminution processes. (a) Sample H4 from site Haindlkar consists of dolomite components ('Dol'; dark grey) which show brighter rims along crystal borders as result of dedolomitization processes ('Cc<sub>1</sub>'). Subsequent cementation with calcite material is illustrated in light grey to white ('Cc<sub>2</sub>'). (b) Ultracataclasite sample from site Fölz (sample EA1) showing dolomite components with maximum diameters of 50 μm embedded in completely dedolomitised (calcite) cement ('Cc<sub>1</sub>'). Dashed red line borders two domains of ultracataclasite in this sample. Left domain exhibits dolomite components with maximum diameters of 20 μm, indicating increased shear and comminution.

All samples show distinct evidence of dedolomitization processes (Ayora et al. 1998; Arenas et al. 1999; Zeeh et al. 2000; Nader et al. 2003; Benito et al. 2006; Arienzo 2008; Fu et al. 2008; Rameil 2008) with variable characteristics (Figs. 3-10, 3-11, 3-12). The most common feature is an increased luminescence along crystal borders and intra-granular fractures caused by the dedolomitization along fragment borders. This reaction produces Mg-depleted, Ca-enriched rims around dolomite components and is responsible for observed luminescence behavior (Figs. 3-2, 3-4, 3-6, 3-9a).

Ultracataclasites represent an advanced stage of dedolomitization (Fig. 3-9b). Due to high displacement (shear) and appropriate fluid chemistry (Ca-rich) and fluid flow, these fault rocks mainly consist of micritic calcite cement/matrix and dolomite components with particle sizes less than 50  $\mu\text{m}$  (Fig. 3-12).

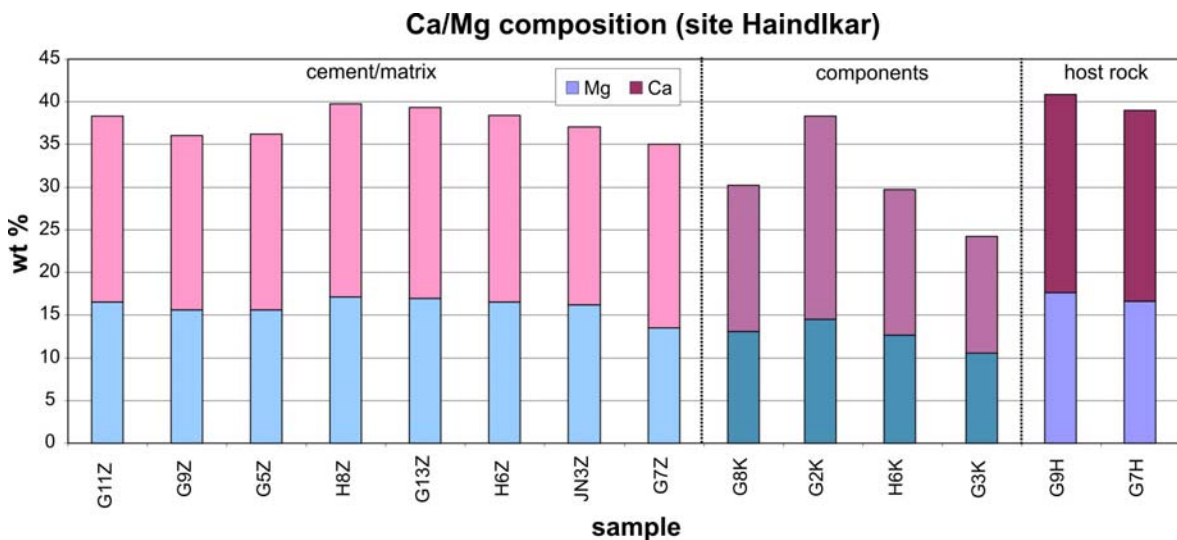


Figure 3-10: Ca and Mg composition of powder samples from site Haindlkar. Though CL and microprobe analysis give distinct evidence for dedolomitization processes, no significant change in Ca/Mg ratios between host rock, cataclasite components and cement/matrix is visible. Host rock samples may already underwent dedolomitization in similar extent with respect to cataclasite components and cement/matrix.

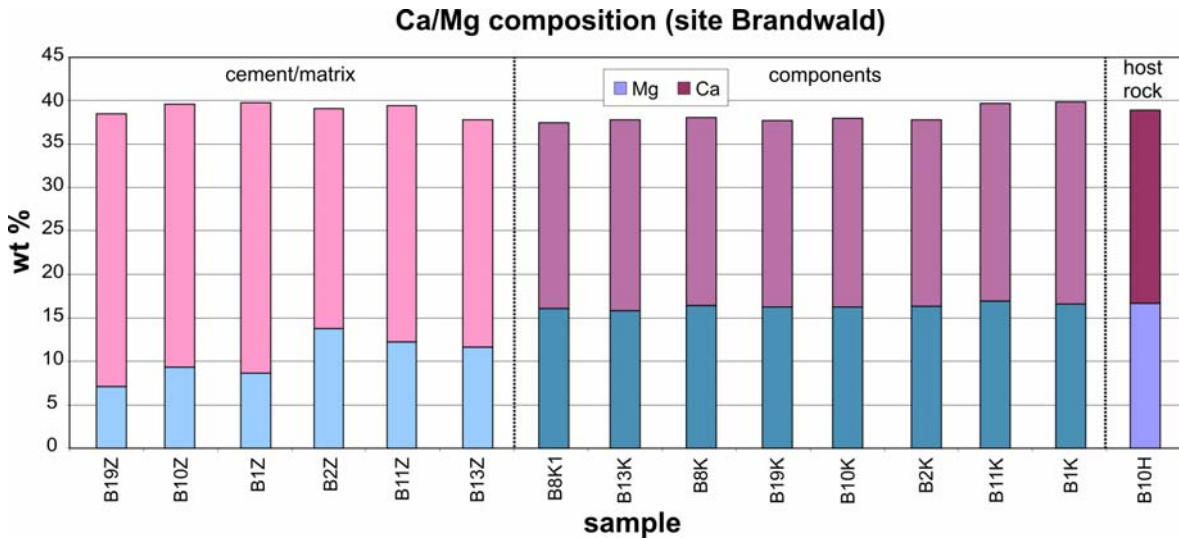


Figure 3-11: Ca and Mg composition of powder samples from site Brandwald. While the Ca/Mg ratio is constant in host rock and cataclasite components, cement/matrix samples exhibit distinct indications for dedolomitization, illustrated by a distinct change of Ca/Mg ratio (decreased Mg- and increased Ca content).

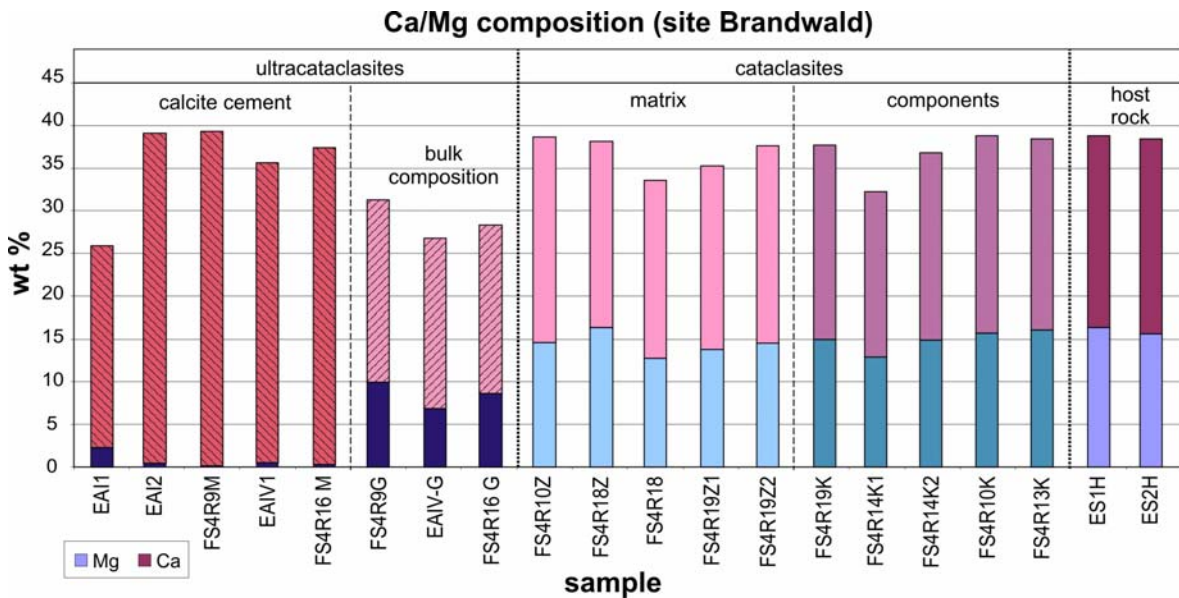


Figure 3-12: Ca and Mg composition of powder samples from site Fölz. Ca/Mg ratios of host rock and cataclasite samples exhibit only slight variations. However, ultracataclasites show distinct evidence of partial (bulk composition) and almost complete dedolomitization into calcite cements.

### 3.7.2 Fluid phases and properties

Distinct stages of fluid infiltration have been categorized chronologically with respect to chemical composition and related CL behavior in a sequence of five phases (Figs. 3-10, 3-11). Phase 1 (P1) concerns all sites and analyzed samples. Dedolomitization, as described above, is visible in variable distinctness. This stage comprises dedolomitization processes synchronous and subsequent to cataclastic events. Fluid chemistry is characterized as Ca-rich with a very low amount of Fe and an adequate Mn content, indicated by bright red luminescence along crystal borders and intra-granular fractures (Figs. 3-2, 3-4, 3-6).

Phase 2 (P2) is subdivided with respect to fluid chemistry in two different stages. At site Fölz quartz filled veins and pore volumes indicate Si-rich fluid phases (Fig. 3-6). Samples from site Haindlkar and site Brandwald exhibit pore volumes and veins cemented by euhedral to subhedral calcite which derived from Ca-rich fluids. These fluid phases are characterized by an increased Fe content with respect to initial phase P1. Precipitation of Fe-hydroxides in veins and pores has been distinguished in samples from site Brandwald and Fölz (Figs. 3-5j-l; 3-7j, k). As a basic principle increased Fe-content quenches luminescence. Therefore, precipitated calcite from this phase can be easily distinguished from early dedolomitization features (Figs. 3-2f; 3-3; 3-4c, f; 3-5).

Fluid phases 3 to 5 (P3-P5) exclusively developed at site Fölz. P3 is restricted to ultracataclasite samples and characterized by calcite vein fillings with bright red luminescence. These veins developed in quartz veins (concordant) from phase P2 (Figs. 3-6, 3-7) and show an internal zonation of Mn-enriched bands, visible as bright red stripes in CL images (Fig. 3-13).

Phase 4 represents another change in fluid chemistry and deformation. Calcite filled veins developed sub-perpendicular to no-luminescent quartz and calcite veins from phase P3 (Figs. 3-6g-i, 3-14). Chemical composition (high Fe-amount and low Mn-values) prevents any luminescence of P4-vein fillings.

The latest stage of distinguished fluid development marks another change in fluid chemistry. Phase 5 (P5) calcite veins crosscut all prior features and show a very bright red luminescence (Fig. 3-14).



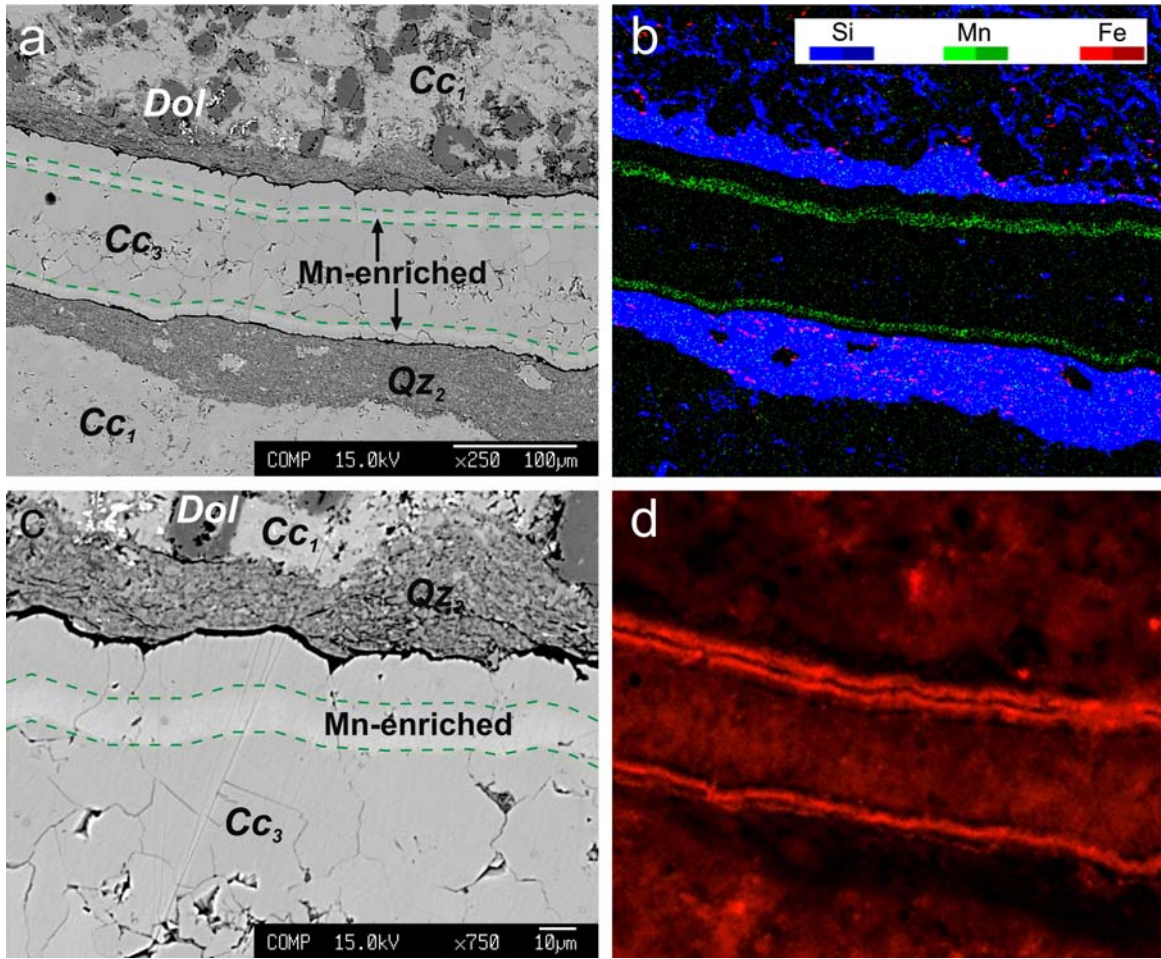


Figure 3-13: (a, c) BSE image of a secondary calcite vein in ultracataclasite sample EA1. Dolomite components ('Dol') are embedded in dedolomitized material ('Cc<sub>1</sub>'). Calcite vein Cc<sub>3</sub> strikes through former quartz veins ('Qz<sub>2</sub>') and exhibits internal zonation, showing bands of increases Mn content. (b) Combined element mapping of Si, Mn and Fe illustrates Mn enriched bands and quartz precipitation in veins and intergranular pore space. (c) Detailed image of the upper rim of the calcite vein. (d) CL image clearly illustrates the bright luminescence of Mn-enriched bands. Dedolomite domains show darker red luminescence colors and quartz rich areas stay dark.

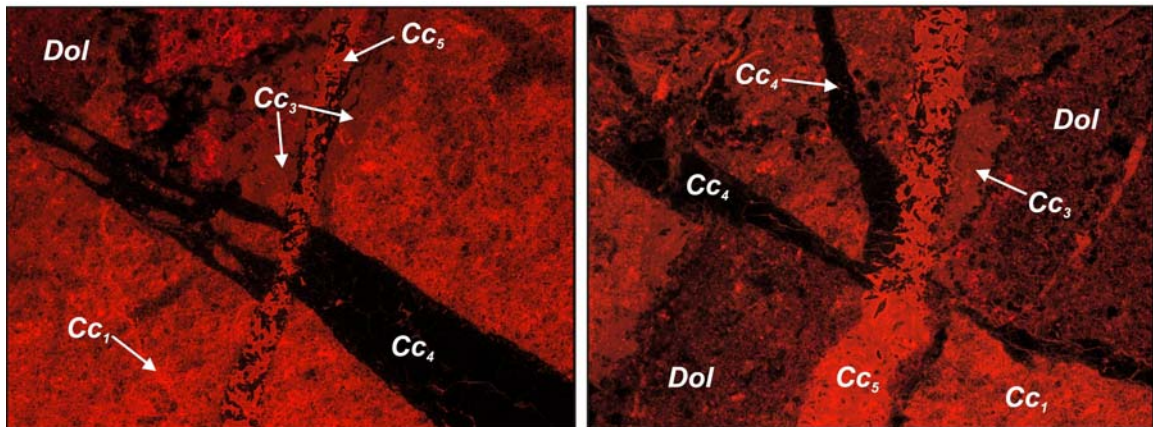


Figure 3-14: CL images of ultracataclasites from site Fölz (samples EA1 and EA2) illustration CL behavior and chronological sequence of all five fluid phases (phase P1 to P5). Calcite cement

derived from de-dolomitization ('Cc<sub>1</sub>') and phase P3 ('Cc<sub>3</sub>') show intermediate to bright red luminescence. Calcite veins from phase P4 ('Cc<sub>4</sub>') with no luminescence developed sub-perpendicular to Cc<sub>3</sub>-veins. Bright red calcite veins from phase P5 ('Cc<sub>5</sub>') strike through dark Cc<sub>4</sub>-veins, dragging non-luminescent material from phase P4 along the course of P5 veins. Image size is 2.8 x 1.7 mm.

### 3.7.3 Fluid source and fluid flow

Stable isotope composition of  $\delta^{13}\text{C}$  and  $\delta^{18}\text{O}$  was used to get additional information on fluid sources and fluid flow (e.g., Kerrich 1986; Taylor and Bucher-Nurminen 1986; Marquer and Burkhard 1992; Ghisetti et al. 2001; Abart et al. 2002; Pili et al. 2002; Rasser and Fenninger 2002; Caja et al. 2003; Kopf et al. 2003; Dallai et al. 2005). All samples show variable  $\delta^{18}\text{O}$  values, ranging from -4,84 to 1,49 ‰. Host rock samples exhibit the tendency to higher values than cataclasite components, matrix material and calcite cement (Fig. 3-8). Host rock and cataclasite components show only slight variation in  $\delta^{13}\text{C}$  values at all three sites, ranging from 2,77 to 4,29 ‰. Samples of matrix material from site Haindlkar and especially from site Brandwald show the tendency to decreased  $\delta^{13}\text{C}$  values of -1,96 to 3,97 ‰, whereas all samples from site Fölz show constant  $\delta^{13}\text{C}$  values between 2,63 to 4,29 ‰ (Fig. 3-8).

Variation of stable isotope signatures are regarded as related to the amount and the chemical composition of fluids (e.g., Pili et al. 2002; Agosta and Kirschner 2003).

Variations in  $\delta^{18}\text{O}$  values with relative constant  $\delta^{13}\text{C}$  signatures are interpreted as either derived from meteoric (aqueous) fluids with very little carbon content (e.g., Kerrich 1986; Ghisetti et al. 2001; Pili et al. 2002; Rasser and Fenninger 2002) or as repeated infiltration of fluids with variable chemistry (Janssen et al. 1998).

Depletion of  $\delta^{13}\text{C}$  in matrix material at site Brandwald and Haindlkar also indicates a meteoric fluid source. The development to lower  $\delta^{13}\text{C}$  values, with respect to host rock and components, is related to the content of biogenic carbonate and the amount of fluid, penetrating the fault core. High fluid flow prevents equilibration of fluids and solids and causes variations in isotope signatures. Low variation in  $\delta^{13}\text{C}$  signature at site Fölz represents a closed system (e.g., Kirschner & Kennedy, 2001; Pili et al., 2002; Agosta & Kirschner, 2003).

The development of isotopic signatures from host rocks to components and further matrix material, indicated by decreasing  $\delta^{18}\text{O}$  values and decreasing (site Haindlkar and Brandwald) or constant  $\delta^{13}\text{C}$  values (site Fölz) (Fig. 8), indicate meteoric derived fluids

and low temperatures between 30 and 100°C (e.g., Kerrich, 1986; Agosta and Kirschner 2003; Nader et al. 2003).

Precipitation of Fe-hydroxides and Fe-rich carbonates (Phase P2 and P4) indicates that related fluids circulated through deeper parts of the sedimentary sequence. Fe-enrichment is assumed to be derived from clastics, therefore, the underlying Werfen Formation is presumed to be the source for this Fe-enrichment. Site Fölz is situated in close range to the clastic Werfen Formation and shows Fe-contents up to 10 times higher than samples from site Haindlkar and Fölz. Si-rich fluids (Phase P2, site Fölz) also reference the Werfen Formation as potential fluid source. Enrichment in Fe or Si is assumed to be an indicator for changing fluid temperature and/or changing pH-value.

### **3.8 Conclusions**

The methodical combination of cathodoluminescence, microprobe- and stable isotope analysis in this study enables the determination, characterization and chronological sequence of different fluid phases in fault core rocks of brittle fault zones in the Northern Calcareous Alps. The following general assumptions can be deduced from the interpretation of this study's results:

- (1) The methodical combination of cathodoluminescence, microprobe and stable isotope analysis allows the reconstruction of the evolution of fluid chemistry in carbonate fault zones.
- (2) Five fluid phases and related processes were distinguished and classified with respect to fluid chemistry, CL behavior and structural processes.
- (3) Besides differentiation of fluid generations, detailed CL images provide an indication of internal, chemical zonation of carbonate vein and pore fillings.
- (4) Stable isotope composition ( $\delta^{13}\text{C}$  and  $\delta^{18}\text{O}$ ) indicates fluid sources of mainly meteoric origin. The extent of variation of isotopic signatures is related to the amount fluid and fluid flow through the fault zone, respectively.
- (5) Circulation of meteoric derived fluids through deeper, clastic sequences (Werfen Formation) is deduced as potential mechanism for Fe- and Si-enriched fluids and related precipitation of Fe-hydroxides, Fe-rich carbonates and quartz vein fillings.

### 3.9 References

- Abart, R., Badertscher, N., Burkhard, M., Povoden, E., 2002. Oxygen, carbon and strontium isotope systematics in two profiles across the Glarus Thrust: implications for fluid flow. *Contrib Mineral Petrol* 143, 192-208.
- Agosta, F., Kirschner, D.L., 2003. Fluid conduits in carbonate-hosted seismogenic normal faults of central Italy. *Journal of Geophysical Research* 108 B4, 2221-2234.
- Arenas, C., Alonso Zarza, A.M., G., P., 1999. Dedolomitization and other early diagenetic processes in Miocene lacustrine deposits, Ebro Basin (Spain). *Sedimentary Geology* 125, 191-214.
- Arienzo, M., 2008. Dedolomitization of the Cambrian Ledger and Kinzers Formations, York County, PA. Franklin & Marshall College, Department of Geosciences, Abstract.
- Ayora, C., Taberer, C., Saaltink, M.W., Carrera, J., 1998. The genesis of dedolomites: a discussion based on reactive transport modelling. *Journal of Hydrology* 209, 346-365.
- Barker Shaun, L.L., Cox, S.F., Eiggins, S.M., Gagan, M.K., 2006. Microchemical evidence for episodic growth of antitaxial veins during fracture-controlled fluid flow. *Earth and Planetary Science Letters* 250, 331-344.
- Bauer, F.K., 1998. Zur Frage der Mürzalpendecke im Gebiet der Gesäuseberge und eine Diskussion über die Stellung der Nördlichen Kalkalpen. *Jahrbuch der Geologischen Bundesanstalt* 141, 5 - 19.
- Bellot, J.-P., 2007. Extensional deformation assisted by mineralised fluids within the brittle-ductile transition: Insights from the southwestern Massif Central, France. *Journal of Structural Geology* 29, Issue 2, 225-240.
- Benito, M., Lohmann, K., Mas, R., 2006. Micro-sized dolomite inclusions in ferroan calcite cements developed during burial diagenesis of Kimmeridgian Reefs, northern Iberian Basin, Spain. *Journal of Sedimentary Research* 76, Issue 3-4, 472-482.
- Billi, A., Salvini, F., Storti, F., 2003. The damage zone-fault core transition in carbonate rocks: implications for fault growth, structure and permeability. *Journal of Structural Geology* 25, 1779-1794.
- Billi, A., Valle, A., Brilli, M., Faccenna, C., Funiciello, R., 2007. Fracture-controlled fluid circulation and dissolutional weathering in sinkhole-prone carbonate rocks from central Italy. *Journal of Structural Geology* 29, 385-395.



- Boggs, S., Krinsley, D., 2006. Application of Cathodoluminescence Imaging to the Study of Sedimentary Rocks. Cambridge University Press, New York.
- Budd, D., Hammes, U., Ward, B., 2000. Cathodoluminescence in Calcite Cements: New Insights on Pb and Zn Sensitizing, Mn Activation and Fe Quenching at low Trace-Element Concentration. *Journal of Sedimentary Research* Vol. 70, No.1, 217-226.
- Bustillo, M., Fort, R., Ordoñez, S., 1992. Genetic implications of trace-element distributions in carbonate and non-carbonate phases of limestones and dolostones from western Cantabria, Spain. *Chemical Geology*, 97, 273-283.
- Caine, J.S., Evans, J.P., Forster, C.B., 1996. Fault zone architecture and permeability structure. *Geology* 24, 1025 - 1028.
- Caine, J.S., Foster, C.B., 1999. Fault zone architecture and fluid flow: insights from field data and numerical modelling. in: Haneberg, W.C., Mozley, P.S., Moore, J.C., Goodwin, L.B. (Eds.) - *Faults and Subsurface Fluid Flow in the Shallow Crust*. Geophysical Monograph, Vol. 113. American Geophysical Union, 101–127.
- Caja, A.M., Al-Aasm, I.S., Marfil, R., Tsighe, M., Martin-Crespo, T., Salas, R., 2003. Multiphase carbonate cementation related to fractures in the upper Jurassic limestones, Maestrat Basin (Iberian Range, Spain). *Journal of Geochemical Exploration* 78/79, 33-38.
- Cello, G., Invernizzi, C., Mazzoli, S., Tondi, E., 2001a. Fault properties and fluid flow patterns from Quaternary faults in Apennines, Italy. *Tectonophysics* 336, 63 – 78.
- Cello, G., Tondi, E., Micarelli, L., Inve, C., 2001b. Fault zone fabrics and geofluid properties as indicators of rock deformation modes. *Journal of Geodynamics* 32, 543–565.
- Conti, A., Turpin, L., Polino, R., Mattei, M., Zuppi, G.M., 2001. The relationship between evolution of fluid chemistry and the style of brittle deformation: examples from the Northern Apennines (Italy). *Tectonophysics* 330, 103-117.
- Crampin, S., 1999. Calculable fluid-rock interactions. *Journal of the Geological Society*, Vol. 156, 501-514.
- Dallai, L., Magro, G., Petrucci, E., Ruggieri, G., 2005. Stable Isotope and noble gas isotope compositions of inclusions fluids from Larderello geothermal field (Italy): Constraints to fluid origin and mixing processes. *Journal of Volcanology and Geothermal Research* 148, 152-164.

- Decker, K., Mechede, M., Ring, U., 1993. Fault slip analysis along the northern margin of the Eastern Alps (Molasse, Helvetic nappes, North and South Penninic flysch, and the Northern Calcareous Alps). *Tectonophysics* 223, 291-312.
- Decker, K., Peresson, H., 1996. Tertiary kinematics in the Alpine–Carpathian–Pannonian system: links between thrusting, transform faulting and crustal extension. in: Wessely, G., Liebl, W. (Eds.), *Oil and Gas in Alpidic Thrustbelts and Basins of Central and Eastern Europe*. EAGE Special Publication, 69–77.
- Dietzel, M., Tang, J., Leis, A., Köhler, S.J., 2009. Oxygen isotopic fractionation during inorganic calcite precipitation — Effects of temperature, precipitation rate and pH. *Chemical Geology* 268, 107–115.
- Faulkner, D.R., Jackson, C.A.L., Lunn, R.J., Schlische, R.W., Shipton, Z.K., Wibberley, C.A.J., Withjack, M.O., 2010. A review of recent developments concerning the structure, mechanics and fluid flow properties of fault zones. *Journal of Structural Geology* 32, 1557-1575.
- Fitz-Diaz, E., Hudleston, P., Siebenhaller, L., Kirschner, D., Camprubí, A., Tolson, G., Pi Puig, T., 2011. Insights into fluid flow and water-rock interaction during deformation of carbonate sequences in the Mexican fold-thrust belt. *Journal of Structural Geology* 33, 1237-1253.
- Frisch, W., Dunkl, I., Kuhlemann, J., 2000. Post-collisional orogen-parallel large-scale extension in the Eastern Alps. *Tectonophysics* 327, 239-265.
- Frisch, W., Gawlick, H.-J., 2003. The nappe structure of the central Northern Calcareous Alps and its disintegration during Miocene tectonic extrusion - a contribution to understanding the orogenic evolution of the Eastern Alps. *International Journal of Earth Sciences* Vol. 92, 712-727.
- Fu, Q., Qing, H., Bergman, K.M., Yang, C., 2008. Dedolomitization and calcite cementation in Middle Devonian Winnipegosis Formation in Central Saskatchewan, Canada. *Sedimentology* 55, 1623-1642.
- Gabrielov, A.M., Keilis Borok, V.I., Pinsky, V., Podvigina, O.M., Shapira, A., Zheligovsky, V.A., 2007. Fluids migration and dynamics of a blocks-and-faults system. *Tectonophysics* 429, 229-251.
- Ghisetti, F., Kirschner, D., Vezzani, L., Agosta, F., 2001. Stable isotope evidence for contrasting paleofluid circulation in thrust faults and normal faults of central Apennines, Italy. *Journal of Geophysical Research* 106 B4, 2221-2234.

- Gillhaus, A., Habermann, D., Meijer, J., Richter, D.K., 2000. Cathodoluminescence spectroscopy and micro-PIXE: combined high resolution Mn-analyses in dolomites - First results. *Nuclear Instruments and Methods in Physics Research Section B: Beam Interactions with Materials and Atoms* 161, 842-845.
- Götz, J., 2002. Kathodolumineszenz-Mikroskopie und -Spektroskopie in den Geo- und Materialwissenschaften. *Mitt. Österr. Miner. Ges.* 147.
- Habermann, D., Neuser, R., Richter, D.K., 1996. REE-activated cathodoluminescence of calcite and dolomite: high-resolution spectrometric analysis of CL emission (HRS-CL). *Sedimentary Geology* 101, 1-7.
- Hausegger, S., Kurz, W., submitted. Cataclastic faults along the SEMP fault system (Eastern Alps, Austria) – a contribution to fault zone evolution, internal structure and palaeo-stresses. *Tectonophysics* (submitted January 2013).
- Hausegger, S., Kurz, W., Rabitsch, R., Kiechl, E., Brosch, F.J., 2010. Analysis of the internal structure of a carbonate damage zone: Implications for the mechanisms of fault breccia formation and fluid flow. *Journal of Structural Geology* 32, Issue 9, 1349-1362.
- Hou, X., Jones, B.T., 2000. Inductively Coupled Plasma/Optical Emission Spectroscopy. In: R.A. Meyers (Eds.), *Encyclopedia of Analytical Chemistry*. John Wiley & Sons Ltd, Chichester, 9468-9485.
- Janssen, C., Laube, N., Bau, M., Gray, D.R., 1998. Fluid regime in faulting deformation of the Waratah Fault Zone, Australia, as inferred from major and minor element analyses and stable isotopic signatures. *Tectonophysics* 294, 109-130.
- Kerrick, R., 1986. Fluid infiltration into fault zones: Chemical, isotopic, and mechanical effects. *Pure and Applied Geophysics* 124, 225-268.
- Kim, Y.-S., Peacock, D.C.P., Sanderson, D.J., 2004. Fault damage zones. *Journal of Structural Geology* 26, 503–517.
- Kirschner, D., Kennedy, L., 2001. Limited syntectonic fluid flow in carbonate-hosted thrust faults of the Front Ranges, Canadian Rockies, inferred from stable isotope data and structures. *Journal of Geophysical Research*. 106, 8827-8840.
- Kopf, A., Behrmann, J., Deyhle, A., Roller, S., Erlenkeuser, H., 2003. Isotopic evidence (B, C, O) of deep fluid processes in fault rocks from the active Woodlark Basin detachment zone. *Earth and Planetary Science Letters* 208, 51-68.

- Lee, M., Martin, R., Trager-Cowan, C., Edwards, P., 2005. Imaging of cathodoluminescence zoning in calcite by scanning electron microscopy and hyperspectral mapping. *Journal of Sedimentary Research* Vol. 75, No. 2, 313-322.
- Linzer, H.-G., Decker, K., Peresson, H., Dell'Mour, R., Frisch, W., 2002. Balancing lateral orogenic float of the Eastern Alps. *Tectonophysics* 354, 211-237.
- Linzer, H.-G., Moser, F., Nemes, F., Ratschbacher, L., Sperner, B., 1997. Build-up and dismembering of the eastern Northern Calcareous Alps. *Tectonophysics* 272, 97-124.
- Linzer, H.-G., Ratschbacher, L., Frisch, W., 1995. Transpressional collision structures in the upper crust: the fold-thrust belt of the Northern Calcareous Alps. *Tectonophysics* 242, 41-61.
- Mandl, G., 2000. The Alpine sector of the Tethyan shelf - Examples of Triassic to Jurassic sedimentation and deformation from the Northern Calcareous Alps. *Mitteilungen der Österreichischen Geologischen Gesellschaft* 92, 61-77.
- Marchel, H.G., 2000. Application of Cathodoluminescence to Carbonate Diagenesis. In: Pagel M., Barbin V., Blanc P. and Ohnenstetter D (Ed.), *Cathodoluminescence in Geosciences*. Springer, Berlin.
- Marfil, R., Caja, M.A., Tsighe, M., Al-Aasm, I.S., Martin-Crespo, T., Salas, R., 2005. Carbonate -cemented stylolites and fractures in the Upper Jurassic limestones of the Eastern Iberian Range, Spain: A record of paleofluids composition and thermal history. *Sedimentary Geology* 178, 237-257.
- Marquer, D., Burkhard, M., 1992. Fluid circulation, progressive deformation and mass-transfer processes in the upper crust: the example of basement-cover relationship in the External Crystalline Massifs, Switzerland. *Journal of Structural Geology* 14, Issue 8/9, 1047-1057.
- Micarelli, L., Benedicto, A., Invernizzi, C., Saint-Bezar, B., Michelot, J.L., Vergely, P., 2005. Influence of P/T conditions and the style of normal fault initiation and growth in limestones from the SE-Basin, France. *Journal of Structural Geology* 27, 1577-1598.
- Montaser, A., 1992. *Inductively coupled plasmas in analytical atomic spectrometry*. VCH-Verlagsgesellschaft, Weinheim.
- Nader, F.H., Swennen, R., Ottenburgs, R., 2003. Karst-meteoric Dedolomitization in Jurassic Carbonates, Lebanon. *Geologica Belgica* 6, 1-2, 3-23.

- Nemes, F., Pavlik, W., Moser, M., 1995. Geologie und Tektonik im Salztal (Steiermark) – Kinematik und Paläospannungen entlang des Ennstal-Mariazell-Blattverschiebungssystems in den Nördlichen Kalkalpen. *Jahrbuch der Geologischen Bundesanstalt* 138, 349 - 367.
- Nölte, J., 2002. ICP Emissionsspektrometrie für Praktiker. Wiley-VCH, Weinheim.
- Peresson, H., Decker, K., 1997. Far-field effects of Late Miocene subduction in the Eastern Carpathians: E-W compression and inversion of structures in the Alpine-Carpathian-Pannonian region. *Tectonics* 16, No. 1, 38-56.
- Pili, E., Poitrasson, F., Gratier, J.-P., 2002. Carbon-oxygen isotope and trace element constraints on how fluids percolate faulted limestones from the San Andreas Fault system: partitioning of fluid sources and pathways. *Chemical Geology* 190, 231-250.
- Rameil, N., 2008. Early diagenetic dolomitization and dedolomitization of Late Jurassic and earliest Cretaceous platform carbonates: A case study from the Jura Mountains (NW Switzerland, E France). *Sedimentary Geology* 212, 70–85.
- Rasser, M.W., Fenninger, A., 2002. Paleoenvironmental and diagenetic implications of  $\delta^{18}\text{O}$  and  $\delta^{13}\text{C}$  isotope ratios from the Upper Jurassic Plassen limestone (Northern Calcareous Alps, Austria). *Geobios* 35, 41-49.
- Ratschbacher, L., Frisch, W., Linzer, H.-G., Merle, O., 1991. Lateral extrusion in the Eastern Alps. Part 2: Structural analyses. *Tectonics* 10, 257–271.
- Ratschbacher, L., Frisch, W., Neubauer, F., Schmid, S.M., Neugebauer, J., 1989. Extension in compressional orogenic belts: the eastern Alps. *Geology* 17, 404–407.
- Sample, J.C., Reid, M.R., Tobin, H.J., Moore, J.C., 1993. Carbonate cement indicate channeled fluid flow along a zone of vertical faults at the deformation front of the Cascadia accretionary wedge (northwest U.S. coast). *Geology* 21, 507-510.
- Schmid, S.M., Fügenschuh, B., Kissling, E., Schuster, R., 2004. Tectonic map and overall architecture of the Alpine orogen. *Eclogae geol. Helv.* 97, 93-117.
- Taylor, B.E., Bucher-Nurminen, K., 1986. Oxygen and carbon isotope and cation geochemistry of metasomatic carbonates and fluids-Bergell aureole, Northern Italy. *Geochimica et Cosmochimica Acta*, Vol. 50, 1267-1279.
- ten Have, T., Heijnen, W., 1985. Cathodoluminescence activation and zonation in carbonate rocks: an experimental approach. *Geologie en Mijnbouw* 64, 297-310.

- Todoli, J.-L., Mermet, J.-M., 2008. *Liquid Sample Introduction in ICP Spectrometry*. Elsevier, New York.
- Wang, X., Neubauer, F., 1998. Orogen-parallel strike-slip faults bordering metamorphic core complexes: the Salzach-Enns fault zone in the Eastern Alps, Austria. *Journal of Structural Geology* 20, 799–818.
- Zeeh, S., Becker, F., Heggemann, H., 2000. Dedolomitization by meteoric fluids: the Korbach fissure of the Hessian Zechstein basin, Germany. *Journal of Geochemical Exploration* 69/70, 173–176.

## 4 Applied Methodology

The combination of methodological applications in this thesis focused on various analytical methods and combines a wide field of different examinations of macro- to micro-scale structures as well as geochemical alterations between host rock, cataclastic rock fragments (components) and cement/matrix.

In addition to the methods discussed in the publications (chapters 1, 2 and 3), this chapter gives an insight into further executed examination methods and their results.

Site	Sample	Particle analysis	Thin section	CL	Microprobe	Stable isotopes	ICP	XRD
Fözl	ES12		•			•	•	
	EAL1		•			•	•	•
	EAI.V.1		•	•	•		•	•
	FS1	•	•					
	FS4R1		•	•	•			
	FS4R3	•	•					
	FS4R9		•	•	•	•	•	•
	FS4R10	•				•	•	•
	FS4R13	•				•		
	FS4R14	•	•	•	•	•	•	•
	FS4R15	•	•	•	•		•	
	FS4R16		•			•	•	
	FS4R17	•	•	•	•			
FS4R18		•			•	•	•	
FS4R19					•	•	•	
Brandwald	B1	•				•	•	
	B2	•	•			•	•	•
	B4		•	•	•			
	B6	•				•		•
	B8	•	•	•	•	•	•	
	B10	•				•	•	•
	B11	•	•	•	•	•	•	
	B13	•	•			•	•	•
	B14	•	•					
B19	•				•	•		
Haidlkar	G2		•			•	•	
	G3					•		
	G5		•			•	•	•
	G6		•			•	•	
	G7	•	•	•	•	•	•	•
	G8	•	•			•	•	
	G9					•	•	
	G10		•			•	•	•
	G11					•	•	
	G12	•	•			•	•	
	G13	•	•			•	•	
	JN2		•	•	•			
	JN3	•					•	•
	H4		•		•			
	H6	•	•			•	•	
	H7	•	•			•	•	•
H8	•					•		
H9	•	•						
H10	•	•						

Table 4-1: List of analyzed samples and executed methods.

## **4.1 Particle analysis**

In geosciences the use of two-dimensional sections in order to get information about spatial distribution, size and shape of particles is very common. Particle analysis contributes to the interpretation of deformation mechanisms, comminution processes and displacement of cataclastic fault zones (e.g., Marone and Scholz, 1989; Fernlund, 1998; Storti et al., 2003; Billi and Storti, 2004; Billi, 2005; Heilbronner and Keulen, 2006; Keulen et al., 2007).

In this work, samples from 26 different locations were cross-cut into serial sections with spacing of few centimeters. Particle analysis of serial sections of coherent cataclasite domains lead to multiple 2D-sections through the volume of interest.

### **4.1.1 Particle detection**

Coated samples were scanned in high resolution (800dpi). Contrast improvement and brightness modification in standard image editing software packages (Corel X3, Adobe Photoshop) prepared the images for further analysis.

As described in chapter 2.3, particle size and shape analysis of cataclastic fault core rocks was conducted by the program package “analySIS auto 5.0© 1986–2006, Olympus Soft Imaging Solution GmbH”. This software package enables to process, measure and analyze images. Furthermore, data base and report generation is provided in one seamless manner.

Automated particle detection operates with manually defined color threshold values (Fig. 4-1) in order to identify areas (grains or particles) with equal color values and separate them from matrix or embedding matter. Manual error handling after automated detection mainly involves correction of fuzzy grain boundaries and elimination of incorrect detected particles.



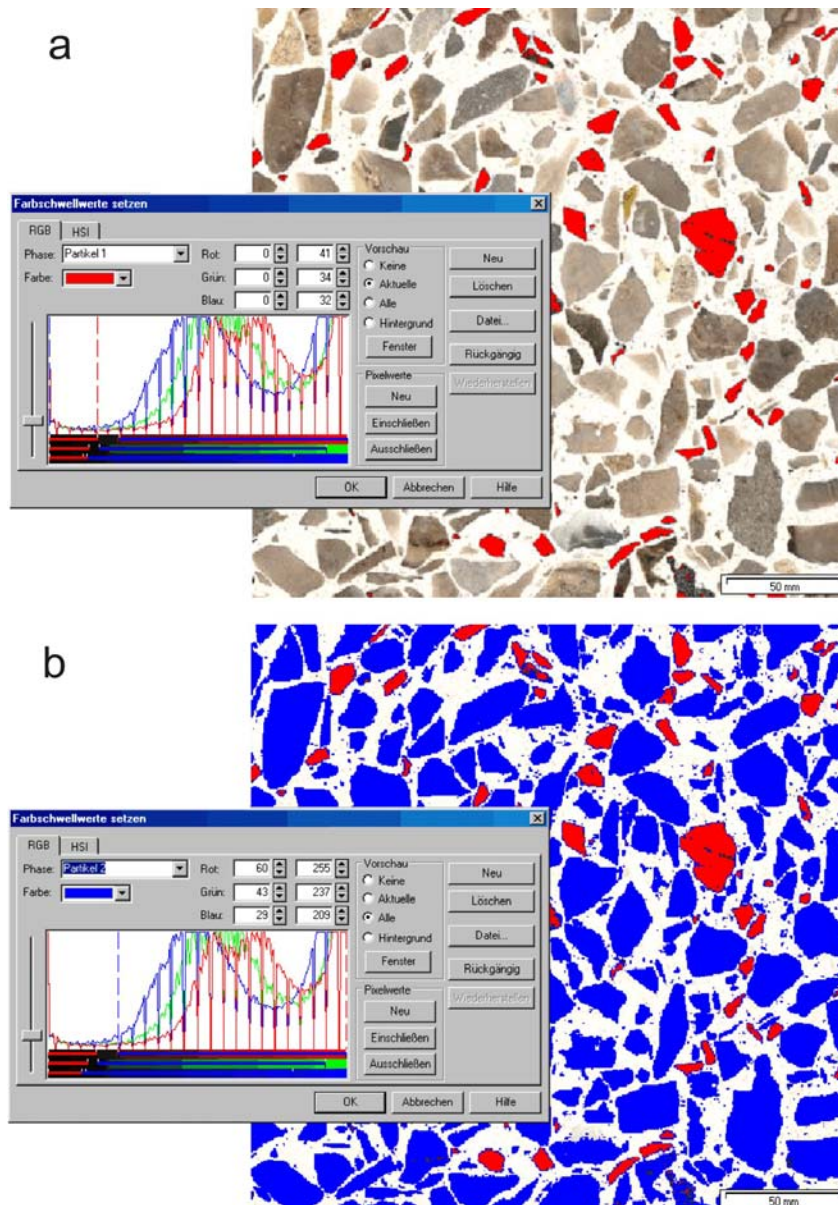


Figure 4-1: Definition of color threshold values for automated particle detection in Olympus analysisIS auto 5.0. Different phases can be defined in order to detect all particles of a given sample or sample area (ROI = region of interest). (a) Setting for particle phase 1. (b) Particle phase 1 (red) and 2 (blue) covers all particles in the sample.

#### 4.1.2 Measurements and data processing

Simultaneously to particle detection this program package provides multifaceted options to analyze, classify and report particle characteristics. Main characteristics in this work include the maximum Feret diameter, aspect ratio, form factor, roundness and elongation

(Figs. 4-2; 4-3). These values are automatically reported in an Excel-like work sheet (Fig. 4-2b).

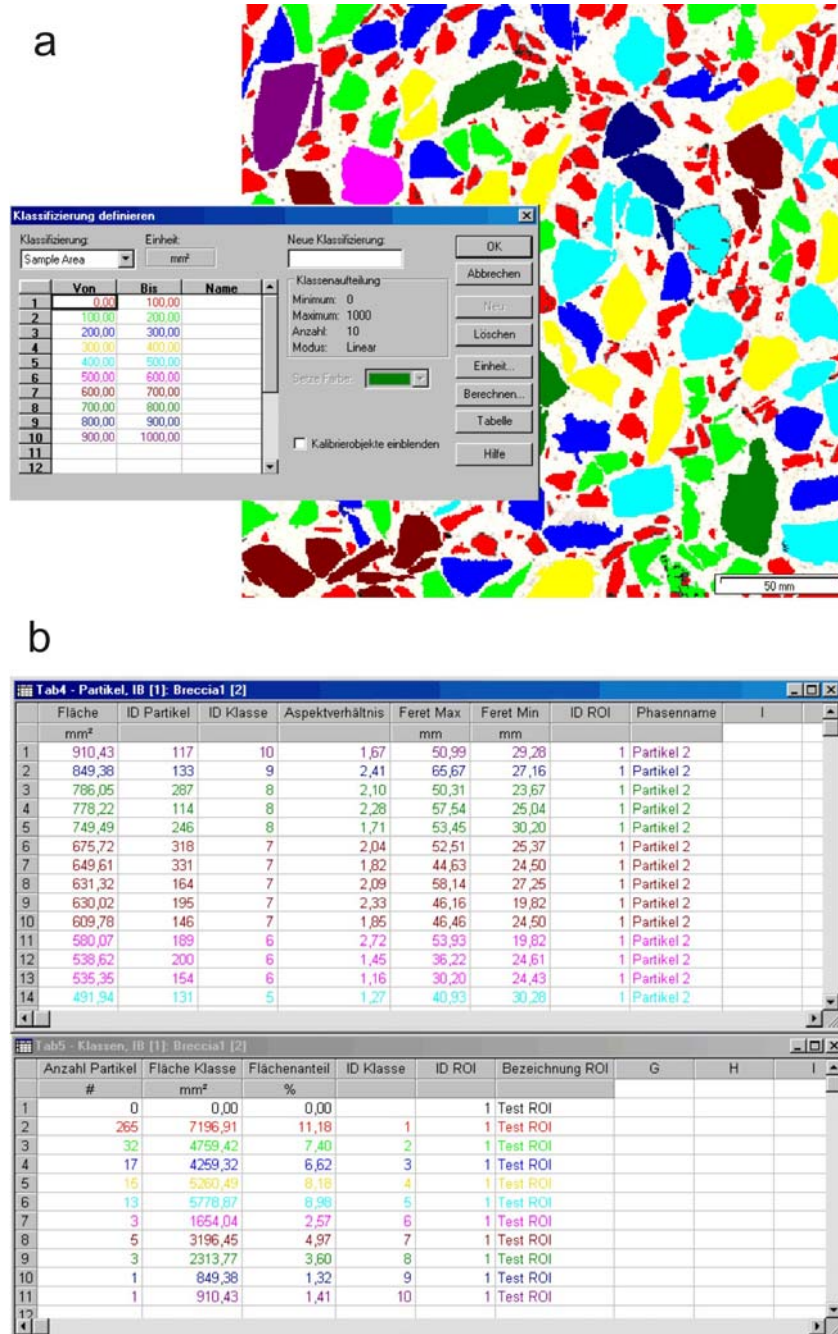


Figure 4-2: (a) Definition of classification of detected particles. In this example particles are classified after their sample area in mm<sup>2</sup> in 10 classes with steps of 100 mm<sup>2</sup>. (b) Data tables of particle analysis and classification results. All measurement results are reported and displayed for each particle and class.

The “size” of particles was determined by  $F_{max}$ -values (maximum Feret diameter) which represent the maximum, normal distance between parallel tangents at opposite points on the particle margin (Fig. 4-3a). Automated analysis routines detect particles with  $F_{max} \geq 0.5$  millimeters. Limited by contrast and image resolution, grain size fraction  $F_{max} < 0.5$  millimeters is attributed to the matrix of analyzed cataclasites.

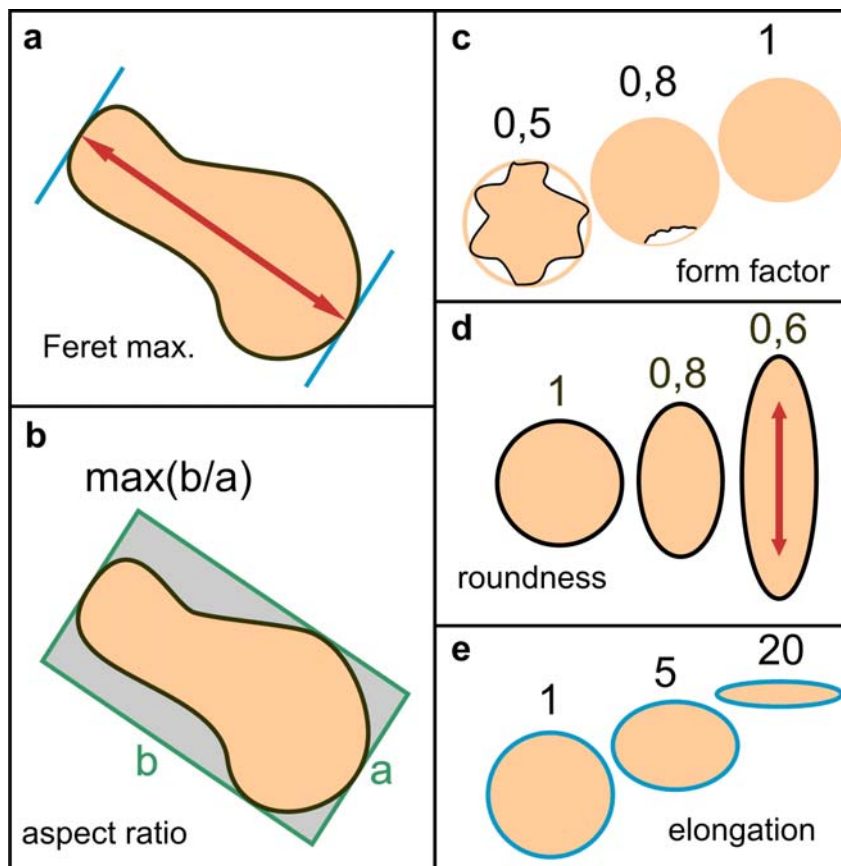


Figure 4-3: Schematic illustration of main particle analysis parameters. (a) Maximum Feret diameter ( $F_{max}$ ) describes the maximum distance between two parallel tangents at opposite particle margin. (b) Aspect ratio of the particle enveloping rectangle. (c) form factor, (d) roundness and (e) elongation.

Form factor, roundness and elongation of particles are calculated simultaneously during particle detection. Calculations follow equations eq. 1 to eq. 3.

$$(eq. 1) \text{ formfactor} = 4 * \pi * \left( \frac{\text{area}}{\text{perimeter}^2} \right)$$

$$\text{(eq. 2) } roundness = \frac{(M_{xx} + M_{yy}) - (4 \cdot M_{xy}^2 + (M_{yy} - M_{xx})^2)^{0.5}}{(M_{xx} + M_{yy}) + (4 \cdot M_{xy}^2 + (M_{yy} - M_{xx})^2)^{0.5}}$$

$$\text{(eq. 3) } elongation = \sqrt{\frac{1}{roundness}}$$

Result sheets (Fig. 4-2b) were exported to MS Excel for further analysis and interpretation for publications (chapters 1 and 2). Advanced procedures include calculation of particle size distribution, evaluation of particle shape characteristics and subsequent compilation of diagrams (Tab. C-4; Figs. 1-10, 2-7, 2-8, 2-9).

## 4.2 References

- Billi, A., 2005. Grain size distribution and thickness of breccia and gouge zones from thin (<1 m) strike-slip fault cores in limestone. *Journal of Structural Geology* 27 (2005) 1823–1837.
- Billi, A., Storti, F., 2004. Fractal distribution of particle size in carbonate cataclastic rocks from the core of a regional strike-slip fault zone. *Tectonophysics* 384 (2004) 115–128.
- Fernlund, J.M.R., 1998. The effect of particle form on sieve analysis: a test by image analysis. *Engineering Geology* 50 (1998) 111–124.
- Heilbronner, R., Keulen, N., 2006. Grain size and grain shape analysis of fault rocks. *Tectonophysics* 427 (2006) 199–216.
- Keulen, N., Heilbronner, R., Stünitz, H., Boullier, A.-M., Ito, H., 2007. Grain size distributions of fault rocks: A comparison between experimentally and naturally deformed granitoids. *Journal of Structural Geology* 29 (2007) 1282 - 1300.
- Marone, C., Scholz, C.H., 1989. Particle-size distribution and microstructures within simulated fault gouge. *Journal of Structural Geology* 11 (1989) No. 7, pp. 799 - 814.
- Storti, F., Billi, A., Salvini, F., 2003. Particle size distribution in natural carbonate fault rocks: insights of non-self-similar cataclasis. *Earth and Planetary Science Letters* 206 (2003) 173-186.

## 5 Conclusion

This thesis comprises field and laboratory studies from sites along a major fault system in the Eastern Alps which was affected by multiple deformation events and therefore provides a complex history of fault development and fluid flow. The overall aim of this thesis is to improve the understanding of:

- (1) Formation and development of brittle fault zones in carbonate environments,
- (2) Internal structural architecture,
- (3) Mechanisms of deformation,
- (4) Comminution processes ,
- (5) Fluid penetration (fluid flow, chemistry and source),
- (6) Chemical alterations (fluid-rock-interactions).

Structural investigation led to a sequence of deformation processes in anisotropic rocks with layer-parallel shear. This sequence describes the evolution of fault zones from initial fracturing (damage zone) to the formation of breccias/cataclasites and related comminution processes (fault core cataclasites). Evidence for cyclic brecciation and subsequent cementation was integrated to the concept of 'fault rock recycling'.

Examination of fault zones in Ladinian Wetterstein-dolomite units of the Mürzalpen nappe enables to elaborate a customized classification of three different fault types (Fault type I, II and III). Main statements and contributions on the research in brittle fault zones of this investigations are (1) progressive fault development is distinguished from Fault type III to Fault type II and Fault type I, (2) the evolution of cataclastic fault cores is depending on orientation with respect to principal stress axis as well as pre-existing and predominant structures and (3) these field observations represent a natural example of fault zone development according to fracture evolution described from Riedel-type experimental configurations.

The methodical combination of cathodoluminescence microscopy, microprobe and stable isotope analysis, linked to ICP-OES and X-ray diffraction data, allowed the reconstruction of fluid chemistry evolution in carbonate fault zones. Discrimination of different fluid phases (characterized by CL behavior and, therefore, chemical composition) and their

chronological classification in this thesis represents new insights in this research field. Furthermore, CL- and microprobe analysis provide evidence of internal, chemical zonation of secondary carbonate precipitation, mainly indicated by changing Fe-, Mn- and Ca-content and therefore changing CL behavior.

In order to classify fluid sources and fluid flow, changes in stable isotope composition of  $\delta^{13}\text{C}$  and  $\delta^{18}\text{O}$  were investigated and led to conclusions on fluid penetration and fluid-rock interactions. Decreasing  $\delta^{13}\text{C}$  and  $\delta^{18}\text{O}$  values in matrix material and cements with respect to host rock composition indicate meteoric derived fluids. However, Fe- and Si enriched fluids are deduced to circulate through deeper, clastic sequences (in this case Werfen Formation).

Changes in fluid chemistry, cyclic fluid infiltration/cementation and variable evidence for equilibration between host rock- and fluid composition implies cyclic changes between an open and a closed system.

## Appendix

### A Coordinates of sites and sampling locations

#### Semmering (Chapter 1)

„Stiegerinhütte“: Topographic map of Austria, 1:50,000, sheet no. 104 (Mürzzuschlag);  
15° 44' 29" E; 47° 39' 17" N, 1030 m.

„Atlitz“: Topographic map of Austria, 1:50,000, sheet no. 104 (Mürzzuschlag); 15° 47' 23"  
E; 47° 39' 28" N, 912 m.

#### Hochschwab (Chapter 2 and 3)

Site Fölz: Topographic map of Austria, 1:50.000, sheet no. 102 (Aflenz); 15° 11' 37.34" E,  
47° 34' 13.35" N, 830 m.

Site Brandwald: Topographic map of Austria, 1:50.000, sheet no. 102 (Aflenz); 15° 09'  
18.23" E, 47° 33' 56.88" N, 887 m.

#### Haindlkar (Chapter 2 and 3)

„Haindlkarhütte“: Topographic map of Austria, 1:50.000, sheet no. 100 (Hieflau); 14° 36'  
45.96" E, 47° 34' 03.33" N, 1122 m.

Haindlkar (cirque): Topographic map of Austria, 1:50.000, sheet no. 100 (Hieflau); 14° 36'  
54.11" E, 47° 34' 35.26" N, 755 m.

Gseng: Topographic map of Austria, 1:50.000, sheet no. 100 (Hieflau); 14° 36' 27.05" E,  
47° 34' 03.75" N, 1214 m.



## B Analytical facilities

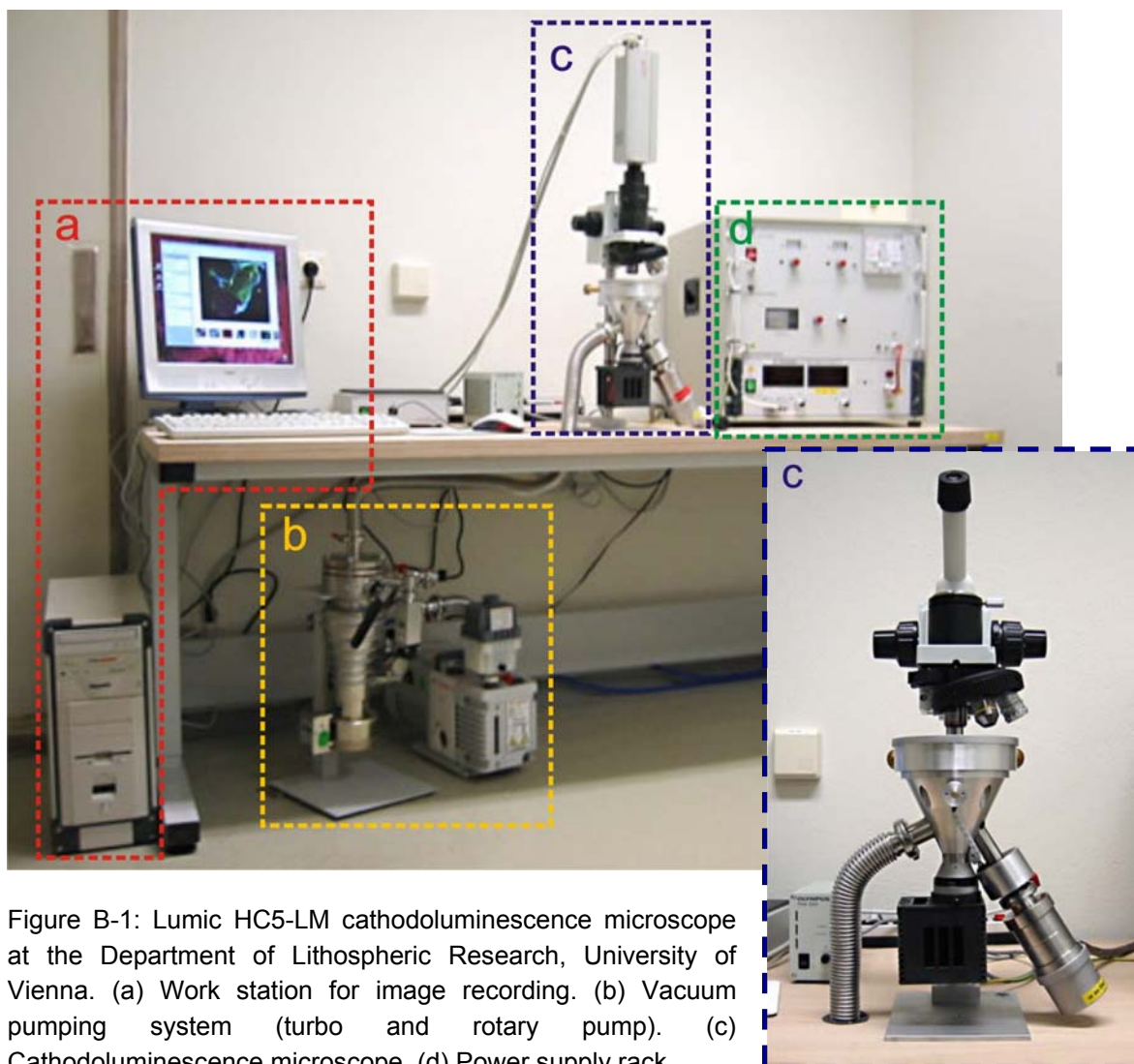


Figure B-1: Lumeric HC5-LM cathodoluminescence microscope at the Department of Lithospheric Research, University of Vienna. (a) Work station for image recording. (b) Vacuum pumping system (turbo and rotary pump). (c) Cathodoluminescence microscope. (d) Power supply rack.

CL microscope	Lumeric HC5-LM
Sample	Polished thin section
Electron beam	Defocused, stationary mode
Electron source	Heated filament (hot-cathode)
Acceleration voltage	14 kV
Beam current	0,1 – 0,45 mA
Deflection	~ 8V
Focus	8 – 12 V
Vacuum chamber	$< 5 \times 10^{-4}$ mbar
Spectral range	380 – 750 nm (visible)
Spatial resolution	1 – 2 $\mu\text{m}$
Analytical combination	Polarized microscopy

Table A-1: CL specifications and analytical settings.





Figure B-2: Microprobe Jeol JXA8200 and work station at the University of Leoben.



Figure B-3: Detailed image of the Jeol JXA8200 Microprobe



Figure B-4: Perkin Elmer Optima 4300 (ICP-OES) at the Institute of Applied Geosciences, University of Technology, Graz (Austria).

## C Data tables

### ICP-OES

element/ sample	Al	Fe	Mn	S	Sr	Ca	Mg
	[ppm]						
G9H	440,13	127,46	btl	336,57	82,65	232012,80	176250,07
G7H	81,23	31,70	btl	345,72	83,21	223874,48	166419,97
G2K	22,49	btl	btl	273,80	49,87	136897,70	105606,79
H6K	56,10	43,52	17,41	320,14	66,74	170225,16	126701,68
G3K	50,80	48,81	20,92	238,07	58,77	238074,25	145434,48
G8K	35,95	30,12	btl	253,60	55,38	171012,47	131174,34
G11Z	51,27	58,30	11,06	254,33	67,35	217132,23	165864,90
G9Z	67,49	56,57	9,92	255,05	64,51	204439,92	155811,01
G13Z	40,17	38,16	btl	300,29	70,30	223959,58	169727,21
G5Z	54,61	26,81	btl	308,79	70,50	206525,19	155886,80
H8Z	47,70	94,39	21,31	276,06	57,85	226327,03	171521,38
H6Z	61,39	108,93	49,51	275,28	66,35	218841,29	165368,76
JN3Z	108,77	128,55	65,26	473,64	90,97	208640,68	162166,22
G7Z	89,36	34,14	6,02	254,01	65,26	195779,51	147587,63

Table C-1: ICP-OES analysis of main (Ca, Mg) and minor (Al, Fe, Mn, S, Sr) elements in ppm. Maximum and minimum values are plotted in red and green, respectively. ('btl' stands for 'below detection limit')

element/ sample	Al	Fe	Mn	Na	S	Sr	Ca	Mg
	[ppm]							
B10H	34,90	108,68	45,86	os	206,39	51,85	221343,36	167503,09
B1K	29,74	236,93	44,61	os	190,34	76,33	231976,86	166547,49
B8K	43,84	392,54	100,63	465,27	142,47	74,72	216198,23	164390,36
B19K	119,31	205,81	52,69	815,28	211,77	71,59	213762,27	163055,87
B10K	25,13	42,81	29,78	677,46	174,02	59,56	216824,95	162851,36
B11K	43,73	50,69	29,82	687,75	246,48	64,60	226598,94	169949,21
B13K	57,35	70,96	34,02	648,38	218,72	58,33	219692,30	158450,64
B2K	13,98	70,88	33,94	750,71	178,69	64,89	214632,12	163719,39
B8K1	67,49	540,90	114,83	404,92	187,35	69,50	213540,46	161162,61
B2Z	29,43	226,28	46,68	369,35	162,35	70,01	252660,11	137999,10
B19Z	22,08	118,42	35,13	475,70	143,51	41,15	314121,32	70953,28
B1Z	44,67	205,49	31,77	os	149,90	56,59	310721,80	86863,12
B10Z	16,19	49,58	19,23	417,93	162,92	37,44	302569,12	93098,19
B11Z	21,68	82,78	35,48	468,11	190,20	50,26	271996,62	122201,38
B13Z	31,26	95,73	38,10	525,55	180,72	44,94	261800,62	116247,29

Table C-2: ICP-OES analysis of main (Ca, Mg) and minor (Al, Fe, Mn, Na, S, Sr) elements in ppm. Maximum and minimum values are plotted in red and green, respectively. ('os' stands for 'oversaturated')

element/ sample	Al	Fe	K	Mn	S	Sr	Ca	Mg
	[ppm]							
ES1H	149,19	426,81	163,02	68,17	214,40	65,21	224275,43	164007,58
ES2H	610,17	1371,90	808,28	142,64	289,24	89,15	227823,89	156505,11
FS4R14K1	1618,65	1470,84	2273,50	321,27	btl	91,35	192964,88	129327,53
FS4R14K2	624,79	1917,32	502,76	224,53	294,82	134,72	218676,12	149363,60
FS4R10K	351,26	1072,54	305,88	103,60	388,76	85,84	230887,51	156885,10
FS4R13K	725,40	1695,64	476,49	118,87	307,84	110,74	223511,65	160522,00
FS4R19K	392,16	649,30	432,86	185,66	360,39	97,30	227352,92	149913,93
FS4R19Z1	1716,21	1633,82	1976,46	404,94	229,10	99,48	215029,03	137658,77
FS4R19Z2	758,78	824,54	920,74	383,81	225,77	95,22	230676,00	145276,80
FS4R10Z	390,43	1541,02	357,29	240,27	315,87	129,45	240267,28	146024,51
FS4R18Z	117,50	1473,40	212,56	124,10	237,64	130,70	217840,98	163710,79
FS4R18	290,80	1222,14	579,59	141,90	3185,76	85,94	207854,05	127910,18
FS4R9G	3434,93	3150,53	4347,42	476,35	217,07	102,51	213049,88	99892,25
EAIV-G	3999,72	2676,82	4117,80	262,18	2984,03	90,06	199135,26	68946,83
FS4R16G	4273,25	3283,25	5503,21	454,84	2896,69	100,41	196794,23	86348,49
FS4R9M	264,57	445,90	367,62	315,10	147,64	169,44	391399,58	1644,87
EAIV1	982,01	1299,63	1625,29	77,39	5343,25	202,03	350788,84	5437,73
EAI1	3888,77	1279,11	4496,17	200,82	252,26	43,53	236432,22	22752,89
EAI2	655,97	394,99	382,90	42,32	143,08	136,03	386932,72	4101,08
FS4R16M	409,53	388,45	1332,98	185,69	5455,39	281,05	371387,87	2961,07

Table C-3: ICP-OES analysis of main (Ca, Mg) and minor (Al, Fe, K, Mn, S, Sr) elements in ppm. Maximum and minimum values are plotted in red and green, respectively. ('btl' stands for 'below detection limit')

## Particle analysis

Site Haindlkar														
sample	fault type	form factor				aspect ratio				roundness				(Fmax) max [mm]
		min	max	mean	std. dev.	min	max	mean	std. dev.	min	max	mean	std. dev.	
G12	I	0,40	0,88	0,62	0,0802	1,04	3,86	1,59	0,4200	0,05	0,97	0,45	0,1997	2,87
G13	I	0,27	0,96	0,65	0,1011	1,04	4,84	1,60	0,4411	0,03	0,98	0,45	0,1919	9,35
G7	I	0,28	0,80	0,65	0,0810	1,03	2,82	1,45	0,3132	0,08	0,97	0,51	0,1972	4,47
G8	I	0,31	0,87	0,68	0,0875	1,04	2,91	1,58	0,3794	0,06	0,94	0,45	0,1877	4,53
H6	II	0,28	0,90	0,71	0,1036	1,04	4,15	1,64	0,4352	0,04	0,95	0,42	0,1904	7,43
H7	II	0,36	0,82	0,66	0,0718	1,04	3,86	1,56	0,3644	0,06	1,00	0,46	0,2078	9,91
H9	II	0,31	1,21	0,61	0,1028	1,08	5,28	1,78	0,5777	0,04	0,95	0,39	0,2079	9,17
JN3M	II	0,12	0,94	0,75	0,1119	1,04	4,25	1,70	0,5176	0,05	0,92	0,42	0,1834	7,29
H10	III	0,29	0,78	0,61	0,0886	1,06	2,78	1,62	0,3629	0,09	0,92	0,41	0,1843	5,22
H8	III	0,27	0,79	0,57	0,0932	1,06	3,55	1,54	0,3594	0,05	0,93	0,46	0,2107	2,91
JN3O	III	0,36	0,94	0,75	0,1028	1,04	5,64	1,71	0,5215	0,03	1,00	0,42	0,2002	5,12
JN3U	III	0,44	0,94	0,76	0,0965	1,05	3,65	1,57	0,3893	0,06	0,97	0,46	0,1997	4,51

Site Brandwald														
sample	fault type	form factor				aspect ratio				roundness				(Fmax) max [mm]
		min	max	mean	std. dev.	min	max	mean	std. dev.	min	max	mean	std. dev.	
B10	I	0,34	0,79	0,64	0,0794	1,05	4,07	1,64	0,4578	0,04	0,97	0,44	0,1990	6,38
B11	I	0,20	0,91	0,63	0,0839	1,04	6,07	1,66	0,4668	0,02	0,99	0,43	0,2010	12,37
B13	I	0,16	0,83	0,62	0,0903	1,03	8,20	1,66	0,5101	0,01	1,00	0,43	0,2006	10,56
B14	II	0,22	0,84	0,61	0,0915	1,03	5,35	1,68	0,5065	0,03	0,98	0,42	0,2049	12,98
B19	II	0,43	0,96	0,79	0,0922	1,05	5,06	1,63	0,4552	0,04	0,98	0,45	0,1987	12,98
B2	II	0,34	0,80	0,65	0,0785	1,04	4,14	1,61	0,4522	0,05	0,97	0,45	0,2010	11,87
B6	II	0,13	0,95	0,75	0,1082	1,03	6,17	1,74	0,5581	0,01	0,97	0,41	0,2003	10,49
B1	III	0,30	0,81	0,65	0,0747	1,05	3,85	1,56	0,3796	0,05	0,99	0,47	0,1973	9,05
B8	III	0,38	0,81	0,64	0,0826	1,05	3,88	1,65	0,4499	0,06	0,95	0,43	0,2011	4,25

Site Fölz														
sample	fault type	form factor				aspect ratio				roundness				(Fmax) max [mm]
		min	max	mean	std. dev.	min	max	mean	std. dev.	min	max	mean	std. dev.	
FS1	I	0,29	0,90	0,72	0,0862	1,04	3,25	1,57	0,3538	0,07	0,96	0,45	0,1843	6,35
FS4R140	I	0,45	0,94	0,79	0,0914	1,05	4,10	1,59	0,4393	0,06	0,98	0,47	0,2048	7,98
FS4R17	I	0,23	0,82	0,62	0,0882	1,03	6,18	1,70	0,5131	0,02	0,97	0,42	0,2030	12,98
FS4R10	II	0,20	0,93	0,61	0,1348	1,02	6,31	1,68	0,4880	0,01	0,97	0,43	0,2032	10,94
FS4R13	II	0,42	0,96	0,79	0,0877	1,04	4,52	1,62	0,4197	0,04	0,99	0,45	0,1970	13,67
FS4R14	II	0,26	0,96	0,77	0,1231	1,03	5,18	1,57	0,3955	0,03	0,99	0,47	0,1926	15,52
FS4R15	II	0,44	0,95	0,79	0,0910	1,04	5,10	1,65	0,4608	0,04	0,98	0,44	0,2028	16,50
FS4R17	II	0,23	0,82	0,62	0,0886	1,03	6,18	1,70	0,5225	0,02	0,97	0,42	0,2024	12,98
FS4R3	II	0,28	0,94	0,77	0,0906	1,05	6,00	1,65	0,4484	0,02	0,95	0,44	0,1967	11,72
FS4R144	III	0,43	0,94	0,77	0,0915	1,05	4,10	1,62	0,4269	0,06	0,98	0,45	0,1985	11,99
FS4R145	III	0,43	0,94	0,76	0,0892	1,06	3,69	1,64	0,4153	0,06	0,94	0,44	0,1954	11,99
FS4R146	III	0,43	0,91	0,75	0,0924	1,12	3,47	1,65	0,4443	0,07	0,91	0,43	0,1906	9,51
FS4R18	III	0,26	0,80	0,61	0,0870	1,03	4,14	1,68	0,4892	0,03	0,94	0,42	0,2049	6,48

Table C-4: Particle analysis data compilation, displaying maximum particle size ( $F_{max}$ ), form factor, aspect ratio and roundness, ordered by site and fault type.



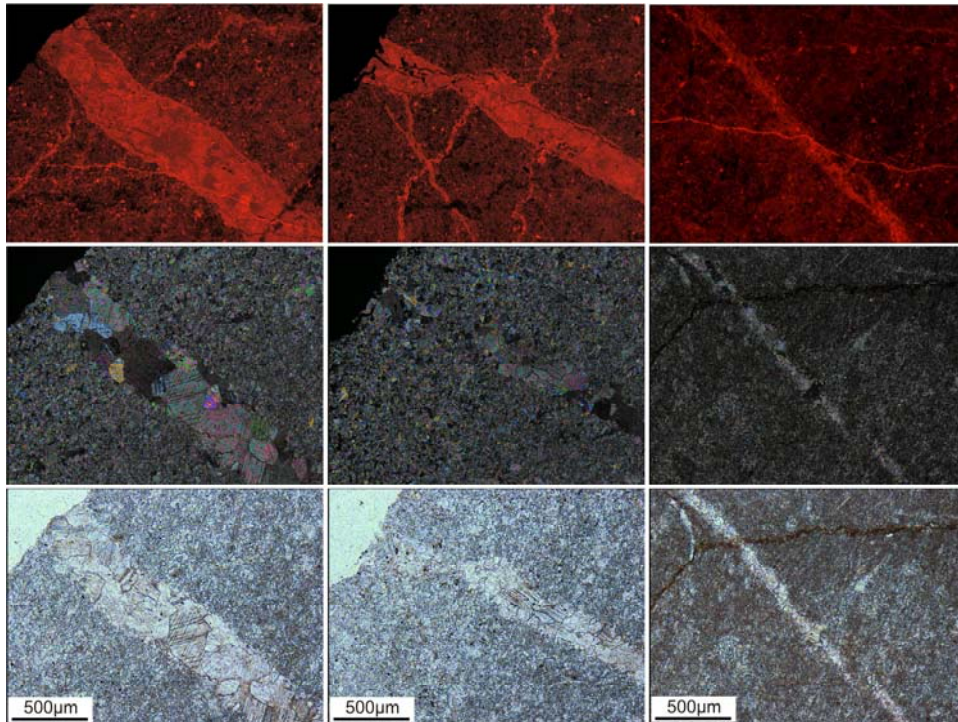
**D Additional figures**

Figure D-1: CL, cross-polarized light and plane-light images of secondary calcite veins in ultracataclasite fault core samples from site Fölz.

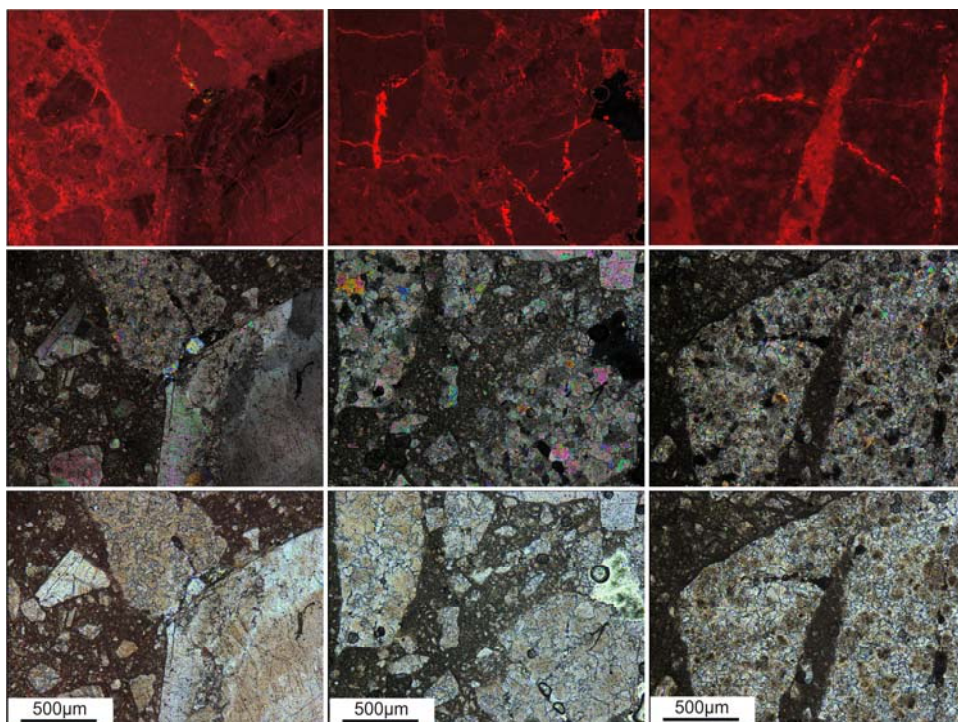


Figure D-2: CL, cross-polarized light and plane-light images of cataclasite fault core samples from site Fölz, showing bright luminescence of dedolomitized matrix and secondary calcite fracture fillings.



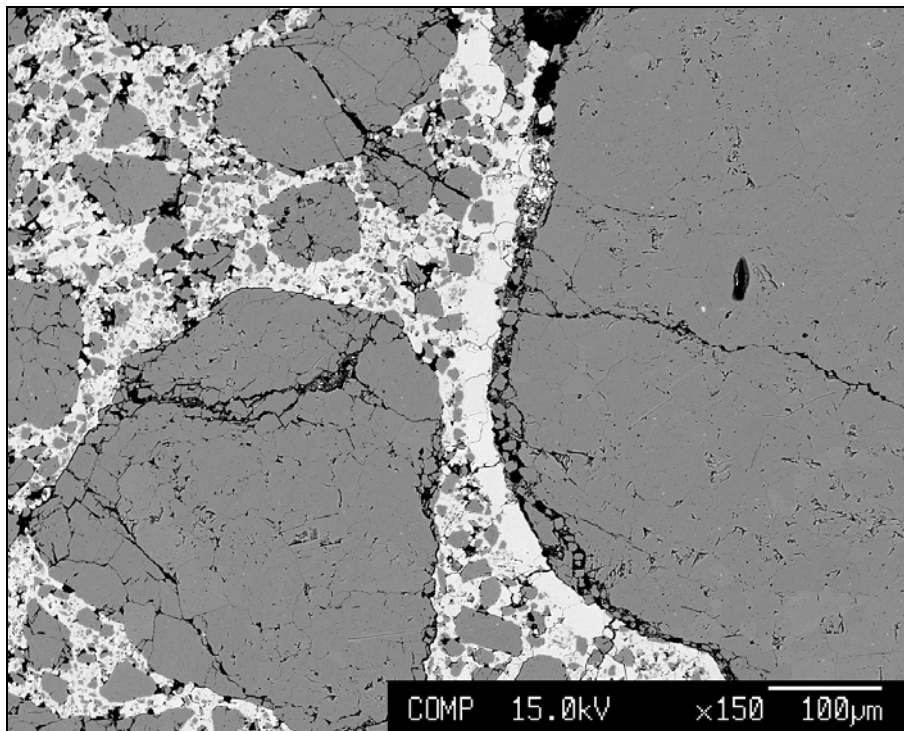


Figure D-3: BSE image of a type I fault core cataclasite from site Brandwald, illustrating comminution along particle and crystal borders and cementation. Dolomite components in dark grey, secondary calcite cement in white.

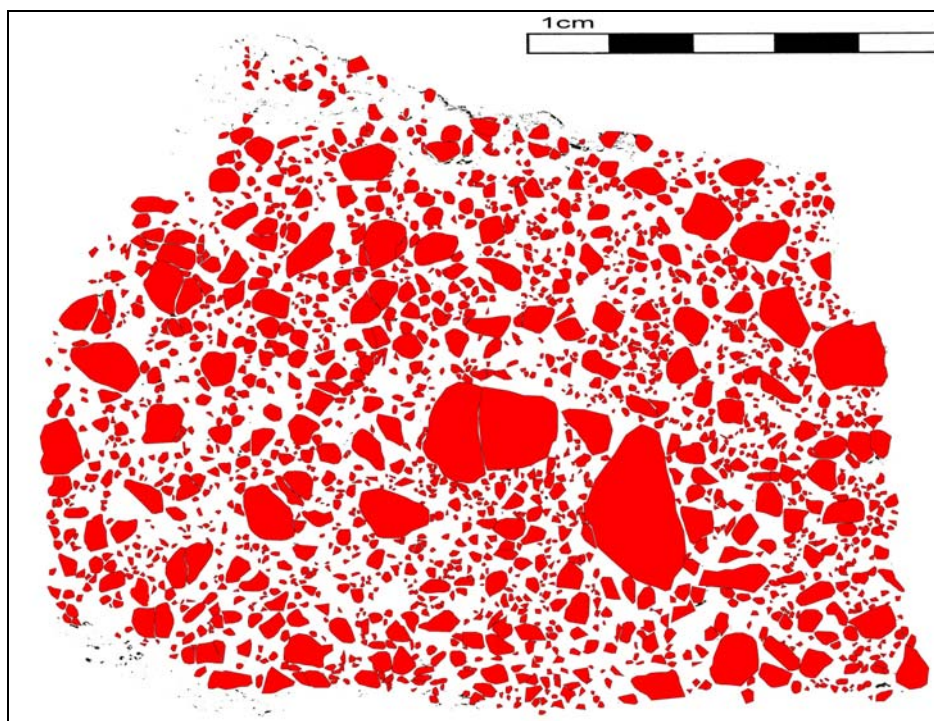


Figure D-4: Example of preliminary particle detection results. Subsequent tasks (1) correction of fuzzy grain boundaries, (2) elimination of incorrect detected particles (3) classification of particle size classes, (4) setup of measurements and export of data in Excel-style work sheets.





Figure D-5: View to the East from the Johnsbach valley (“Gseng”) towards Haindlkar.



Figure D-6: View to ENE towards site Brandwald. Outcrops are located in the middle of the image above the debris covered slope toe.

## Curriculum vitae

Name: Stefan HAUSEGGER  
Home Address: St. Oswald 51B  
A-81113 St. Oswald bei Plankenwarth, Austria  
Telephone: +43 660 34 66 930  
Date of Birth: 1978, June 14<sup>th</sup>  
Nationality: Austria  
E-Mail: stefan.hausegger@gmail.com

### School education

1984–1988 **Elementary school** St.Oswald bei Plankenwarth  
1988–1996 **High school** - BRG Graz, Keplerstrasse 1  
Leaving Examination (1996, June 8<sup>th</sup>)  
1997–1999 **College for Civil Engineering and Steel constructions** - HTBLVA  
Graz, Ortweingasse  
Final Examination (1999, September 22<sup>nd</sup>)

### Academic education

2000–2003 **Bachelor studies – Earth sciences**, University of Graz & Graz  
University of Technology  
Final project: Geoscientific and Geotechnical Work on a new Forest  
Road (Übelbach/Styria).  
Advisor: Univ.-Prof. Dr.phil. Leander P. BECKER<sup>†</sup>  
2003–2006 **Master studies – Earth sciences**, University of Graz & Graz  
University of Technology  
Major subjects in Structural Geology and Engineering Geology  
Master thesis: Internal Deformation of large Slope Movements on the  
Example of the Lärchberg-Galgenwald Mass Movement  
(Murau/Styria).  
Advisor: Univ.-Prof. Mag. Dr. Walter KURZ  
2006–2013 **Doctoral studies – Technical Geology**, Graz University of  
Technology  
Ph.D. project: Fluid penetration through carbonate fault rocks.  
Advisor: Univ.-Prof. Mag. Dr. Walter KURZ

## Work experience

- 2006 – 2009     **Scientific staff**; Institute for Applied Geosciences, Graz University of Technology, Graz, Austria  
Project title: Fluid penetration through carbonate fault rocks.
- 2010            **Assistant Lecturer** (Brittle Tectonics); Institute for Earth Sciences, University of Graz
- 2010 – 2011    **Field Geologist**, Intergeo ZT GmbH, Salzburg  
Libyan Railways, Railway line Sirte – Benghazi (based at Ras Lanuf)
- 2011            **Scientific staff**, Institute for Applied Geology, University for Natural Resources and Life Sciences (BOKU), Vienna  
Project title: Geo-Hazards and Mass Movements in the Pamirs.
- since 2011     **Scientific staff**; Institute for Earth Sciences, University of Graz

## Languages

German (Mother tongue)  
English (very good)  
French (basics)

## Further qualifications / Software skills

AutoCAD 2012  
ArcMap/GIS Version 10  
ENVI incl. SARscape Modules  
JointMetriX<sup>3D</sup> & ShapeMetriX<sup>3D</sup>  
TectonicsFP, Win\_Tensor, OpenStereo  
MS Office, CorelDraw Graphics Suite

Stefan Hausegger

## Publications

- 2013 Cataclastic faults along the SEMP fault system (Eastern Alps, Austria) – a contribution to fault zone evolution, internal structure and palaeo-stresses. (submitted to *Tectonophysics*, January 2013) - Hausegger, S. & Kurz, W.  
Changing fluid chemistry during continuous shearing in cataclastic fault zones – a semiquantitative analysis based on cathodoluminescence, microprobe and stable isotope analysis. (submitted to *Journal of Structural Geology*, March 2013) - Hausegger, S. & Kurz, W.
- 2012 Brittle fault re-activation in the southern parts of the Northern Calcareous Alps (Styria, Austria) - contribution on palaeo-stress, fault development, structural inventory and comminution.  
10th Anniversary of PANGEO, Salzburg (Austria) - Hausegger, S. & Kurz, W.  
Final report „Compilation of a digital, tectonic and structural geological map of Lower Austria“.  
Unpublished Report of the Federal State Government of Lower Austria, Geological Office – Hausegger, S. & Kurz, W.
- 2011 Progress report „Compilation of a digital, tectonic and structural geological map of Lower Austria“.  
Unpublished Report of the Federal State Government of Lower Austria, Geological Office – Hausegger, S. & Kurz, W.
- 2010 Analysis of the internal structure of a carbonate damage zone: Implications for the mechanisms of fault breccia formation and fluid flow.  
*Journal of Structural Geology* 32 (2010) Issue 9, Pages 1349–1362 - Hausegger, S.; Kurz, W.; Rabitsch, R.; Kiechl, E.; Brosch, F.-J.
- 2009 Grain Boundary Systematics and Differential Stress from Fractal Geometry.  
5th International Conference on Fractals and Dynamic Systems in Geosciences, Townsville, Australia - Krenn, R.; Fritz, H.; Hergarten, S.; Hausegger, S.
- 2009 Brittle Structures and Fault Development in Carbonatic Rocks – A Case Study from the Eastern Alps.  
Topical Issues of Subsoil Usage (Conference). Saint-Petersburg State Mining University (St. Petersburg, Russian Federation) – Hausegger, S.
- 2008 Formation of carbonate cataclasites by fault-breccia recycling.  
33rd International Geological Congress, Oslo (Norway) 2008, S. STT-01 – Hausegger, S.  
Mechanisms of grain-size reduction in layer-parallel brittle shear zones.  
*Geophysical Research Abstracts* ; 2008, S. EGU2008-A-03008, European Geosciences Union General Assembly, Vienna (Austria) – Hausegger, S. & Kurz, W.
- 2007 Formation of fault breccias and cataclastic shear zones within layered carbonates: examples from the Eastern Alps.  
*Geophysical Research Abstracts* (2007), S. 02722, European Geosciences Union General Assembly, Vienna (Austria) – Hausegger, S. & Kurz, W.
- 2006 Die Interdeformation von Großhangbewegungen am Beispiel der Massenbewegung Lärchberg-Galgenwald (Murau, Steiermark).  
*Pangeo Austria* 2006, S. 93 , Innsbruck (Austria) – Hausegger, S.